CR-185630

CSDL-T-1062

TRAJECTORY OPTIMIZATION FOR AN ASYMMETRIC LAUNCH VEHICLE

by

Jeanne Marie Sullivan

June 1990

Master of Science Thesis
Massachusetts Institute of Technology

The Charles Stark Draper Laboratory, Inc.
555 Technology Square
Cambridge, Massachusetts 02139

TRAJECTORY OPTIMIZATION FOR AN ASYMMETRIC LAUNCH VEHICLE

by

Jeanne Marie Sullivan
B.S. Physics, Carnegie Mellon University, (1988)

Submitted to the Department of Mechanical Engineering
in Partial Fulfillment of the Requirements for the
Degree of

MASTER OF SCIENCE
IN MECHANICAL ENGINEERING

at the

MASSACHUSETTS INSTITUTE OF TECHNOLOGY
June 1990

Signature of Author_____
Department of Mechanical Engineering
September 1989

Certified by_____
Professor Kamal Youcef-Toumi
Thesis Advisor, Department of Mechanical Engineering

Approved by_____
Richard D. Goss
CSDL Technical Supervisor

Accepted by_____
Ain A. Sonin
Chairman, Department Graduate Committee

Table of Contents

Chapter **Page**

List of Figures

Figure | Page

Figure **Page**

List of Tables

ABSTRACT

A numerical optimization technique is used to fully automate the trajectory design process for an asymmetric configuration of the proposed Advanced Launch system (A.L.S.). The objective of the A.L.S. trajectory design process is the maximization of the vehicle mass when it reaches the desired orbit.

The trajectories used in this thesis were based on a simple shape that could be described by a small set of parameters. The use of a simple trajectory model can significantly reduce the computation time required for trajectory optimization.

A predictive simulation was developed to determine the on-orbit mass given an initial vehicle state, wind information, and a set of trajectory parameters. This simulation utilizes an idealized control system to speed computation by increasing the integration time step.

The conjugate gradient method is used for the numerical optimization of on-orbit mass. The method requires only the evaluation of the on-orbit mass function using the predictive simulation, and the gradient of the on-orbit mass function with respect to the trajectory parameters. The gradient is approximated with finite differencing.

Prelaunch trajectory designs were carried out using the optimization procedure. For the trajectory shape originally used, the procedure proved to be highly sensitive to the initial guess of the optimal solution. To rectify this problem, the trajectory shape was modified and this change resulted in a procedure that was robust to the initial choice of the guess.

The predictive simulation is used in flight to redesign the trajectory to account for trajectory deviations produced by off-nominal conditions -- e.g., stronger than expected head winds. For this purpose, only a single trajectory parameter is modified -- the value of $Q\alpha$ used in the constant aerodynamic loading portion of the trajectory.

ACKNOWLEDGEMENTS

I received much help and support while working on my masters thesis. I would first like to thank Richard Goss, Frederick Boelitz, and Gilbert Stubbs for all of their advice and assistance. They have taught me much about engineering in my two years at Draper.

I would especially like to thank Monique Gaffney for being such a great friend and study buddy. I would also like to thank my friends Mike (since first grade!), Chavela, Diane, Camille, Mariano, Akhil, Chris, Fred (op.cit.), Carde, Kris, Om, Bob, Duncan, Kamala, Kelly, Pete, Dave, and Cathy.

Finally, I would like to thank my family for all of their encouragement and support. My parents always said I could be anything I wanted to be when I grew up, except play left tackle for the 'Skins.

This report was prepared at the Charles Stark Draper Laboratory, Inc. under Task Order # 74 from the National Space and Aeronautics Administration Langley Research Center under Contract NAS9-18147 with the National Space and Aeronautics Administration Johnson Space Center.

Publishing of this report does not constitute approval by the Draper Laboratory or the sponsoring agency of the findings or conclusions contained herein. It is published for the exchange and stimulation of ideas.

Jeanne M. Sullivan

Chapter One

INTRODUCTION

1.1 Background and Problem

Both manned and unmanned launch vehicles currently require a large amount of planning to design trajectories for each mission flown. This leads to high costs and causes the launch system to be inflexible to last minute payload or orbital changes. In addition, trajectories for these vehicles are designed based on monthly wind averages rather than wind data measured the day of launch. If winds differ too widely from those expected for the design, the vehicle might reach orbit with insufficient fuel left for required orbit maneuvers.

A new launch vehicle is being developed by NASA to alleviate these problems. Called the Advanced Launch System (A.L.S.), the proposed vehicle should decrease the costs associated with mission preparation while allowing the vehicle to be robust to unpredicted wind variations. The vehicle will have wind velocity data available to it from measurements taken a half hour before launch. The goal of the A.L.S. trajectory design has been established by NASA as the maximization of the mass of the vehicle once it has reached a desired orbit. This mass will be referred to in this thesis as the "on-orbit mass." The primary constraint on trajectory design is that the normal aerodynamic loads on the vehicle not exceed design limits.

Several vehicle models of the A.L.S. have been proposed. This thesis focuses on an asymmetrical version submitted by General Dynamics in 1988. This vehicle consists of a core stage containing the payload attached to a single booster. The booster contains seven engines while the core contains only three such engines. The resulting asymmetry in thrust leads to trajectories requiring large pitch angles of attack.

An earlier study was conducted by Boelitz[1]. The guidance and control concepts he developed are included n the full simulation used for this study. Boelitz restricted vehicle motion to the pitch plane by nulling both yaw and roll torques. This thesis will be based on the same assumption so that comparisons between the two studies can be made.

A previous thesis in ascent guidance was done by Corvin[2] . Corvin's thesis had the same goals as this study but utilized a different vehicle mode, the single stage-to-orbit (SSTO) Shuttle II. Corvin developed a simple trajectory shape that could be described by a small set of parameters. Boelitz used this trajectory shape and this thesis will also use this shape.

1.2 Method

To reduce costly prelaunch preparation time and to enhance system flexibility, the trajectory design process should be fully automated. Given a specific vehicle mode, payload, and wind information acquired shortly before launch, a mission planner should be able to use a computer program that determines to within some tolerance on on-orbit mass, the set of trajectory parameters which will maximize the on-orbit mass of the vehicle. That program should then be able to design a trajectory based on these parameters and save the trajectory in the flight computer's memory for the guidance system to command during flight. If the flight computers have the computational capability, then this same program could be used to redesign the trajectory in flight. This redesign would allow the vehicle trajectory to adapt to winds that differ significantly from the prelaunch measurements.

A computer algorithm has been developed which meets the objectives outlined above. The algorithm utilizes a predictive simulation which calculates the vehicle's on-orbit mass

---

[1] Boelitz, F.W., "Guidance, Steering, Load Relief and Control of an Asymmetric Launch Vehicle". 1989. Massachusetts Institute of Technology Master of Science Thesis, CSDL Report T-1036.

[2] Corvin, M.A., "Ascent Guidance for a Winged Boost Vehicle." 1988. Massachusetts Institute of Technology Master of Science Thesis, CSDL Report T-1002.

and a numerical optimization scheme which uses the on-orbit mass to define it's objective function.

The predictive simulation is a simplified simulation that is used in place of the full simulation to calculate on-orbit mass. The predictive simulation idealizes the control system used in the full simulation. This idealized system greatly reduces the total computation time for the on-orbit mass calculation because the vehicle's equations of motion can be integrated using a much larger integration time step. The inputs to the predictive simulation include the current vehicle stage, the prelaunch wind measurement, and a set of trajectory shape parameters.

The numerical optimization scheme uses the negative of the on-orbit mass as the objective function it will minimize. This is equivalent to maximizing on-orbit mass. Whenever the optimization scheme is required to evaluate its objective function at a given set of trajectory parameters, it utilizes the predictive simulation.

A conjugate gradient method was chosen for the numerical optimization scheme because it requires only the objective function and the gradient of the objective function while showing a high speed of convergence. The gradient of the objective function, the derivatives of the on-orbit mass function with respect to the trajectory parameters is approximated with finite differencing.

1.3 Overview

The vehicle model used in this thesis is discussed in Chapter 2. The configuration, thrust modelling, mass properties, and aerodynamic characteristics are all presented. The environmental modeling, including atmospheric pressure, density, and wind velocity is discussed. The chapter also describes the kinematics and dynamic equations of motion needed to simulate the vehicle's motion in a pitch plane about a spherical Earth. Finally, the chapter describes the normal aerodynamic load constraint placed upon the A.L.S. by the vehicle designers.

Chapter 3 describes the trajectory design, guidance, and control concepts developed by Boelitz and implemented in the full simulation used for this thesis. At the end of the

chapter, the proposed trajectory optimization procedure is presented and the requirements for such a procedure are described.

The predictive simulation is discussed in Chapter 4. The simplified kinematics and dynamics are presented along with the idealized control approximation. The predictive simulation was compared to the full simulation for several different time steps and the accuracy was very good.

Chapter 5 justifies the choice of the conjugate gradient method for the numerical optimization of on-orbit mass. The underlying theory and procedure is also presented.

The simulation results are presented in Chapter 6. The numerical optimization procedure worked for the trajectory shape initially defined by Corvin but a small modification of the shape was made to improve the procedure's robustness to arbitrary initial guesses of the optimal set of trajectory parameters.

Chapter 7 presents conclusions drawn from the thesis and suggestions for future research.

Chapter Two

VEHICLE DESCRIPTION AND MODELING

2.1 Physical Description of A.L.S. Vehicle

The vehicle model used for this ascent guidance study is based upon a configuration of the Advanced Launch System (A.L.S.) proposed by General Dynamics in 1988. The A.L.S. is under development by NASA and the Air Force to provide an unmanned boost vehicle capable of delivering large payloads to low-Earth orbit.

The basic arrangement of vehicle components is illustrated by Figure 2.1. The vehicle consists of a core stage and a single booster stage arranged in an asymmetric parallel configuration.

Both the core and booster stages have identical, non-throttleable engines fueled by a 6:1 mixture of liquid hydrogen (LH) and liquid oxygen (LOX). Each engine has a vacuum thrust level of approximately 612,000 lbs. The booster has seven such engines while the core has only three engines. The fuel tanks in each stage are identical. The engine nozzles are gimballed in both the pitch and yaw directions to provide thrust direction control. Since the booster has more engines, its fuel tanks will be depleted before those of the core. When this occurs, the booster is separated from the core.

The upper portion of the core contains the payload bay. The diameter of this section is larger than the lower section of the core. The lower section of the core has approximately the same dimensions as the booster stage. The inertial measurement unit (IMU) is located at the base of the core.

The booster's engines, servos, and fuel lines are contained in a Booster Recovery Module (BRM). This is the only recoverable part of the A.L.S. Separation of the BRM from the booster occurs approximately twenty seconds after the booster separates from the core. Parachutes are then deployed to return the BRM to Earth and recovery is made at sea.

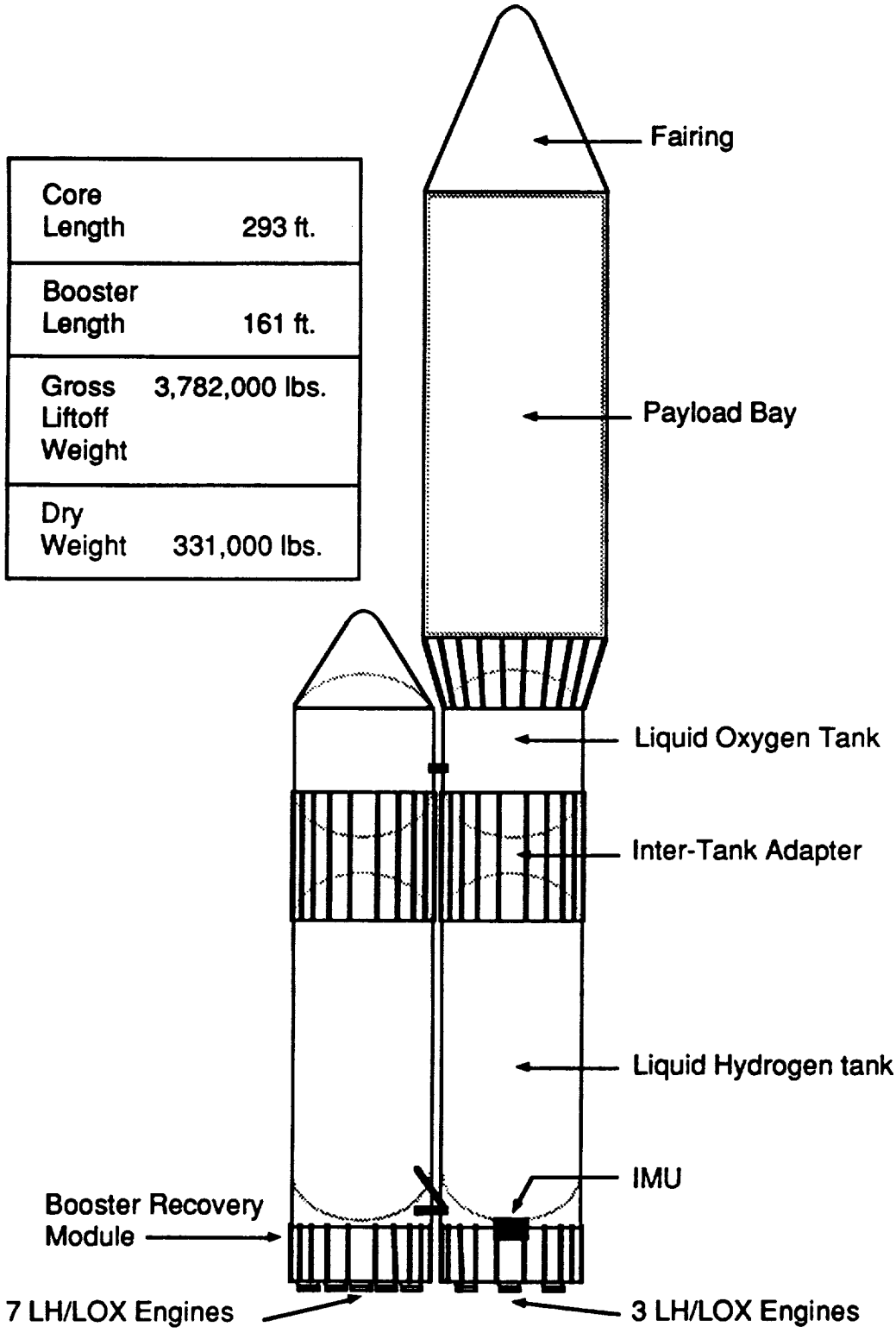

Figure 2.1: A.L.S. Configuration

The A.L.S. vehicle uses a total of 10 gas generator engines. Several important features of the engines are presented in Table 2.1. The engines are non-throttleable, meaning that the thrust level cannot be changed during flight. The mass flow rate and vacuum thrust are both assumed to be constant. The thrust magnitude of each engine within the atmosphere will therefore vary with atmospheric pressure alone.

NAME	SPECIFICATION
Cycle	Gas Generator
Propellants	LOX/LH
Throttling Rage	Fixed
Propellant Flow Rate	1,427 Lbs/sec
Vacuum Thrust	612 KLbs
Weight	6,744 Lbs
Inside Diameter	88.0 in
Length	150 in

Table 2.1: A.L.S. Engine Characteristics

The thrust direction is the only available control input to the system. Each engine is gimballed in both the pitch and yaw planes so that the deflection angle of the engine nozzles can be changed during flight. The limit on the gimballing capability of each engine is $\pm 9°$. Because of the asymmetry of the vehicle, the engines were installed with a 5° cant angle in the pitch plane. This design feature allows the vehicle to have a large gimballing capability to prevent limiting of the engine nozzle deflection angle. The rate of change of the nozzle deflection is limited to 10°/sec.

For this study, it was assumed that the thrust for the set of engines in each stage could be represented by a resultant thrust vector such that two thrust vectors, T_b and T_c, would be controlling the vehicle. This assumption is described by Figure 2.2. As shown, both thrust vectors are limited to a deflection of 9° from the installed cant angle of 5°.

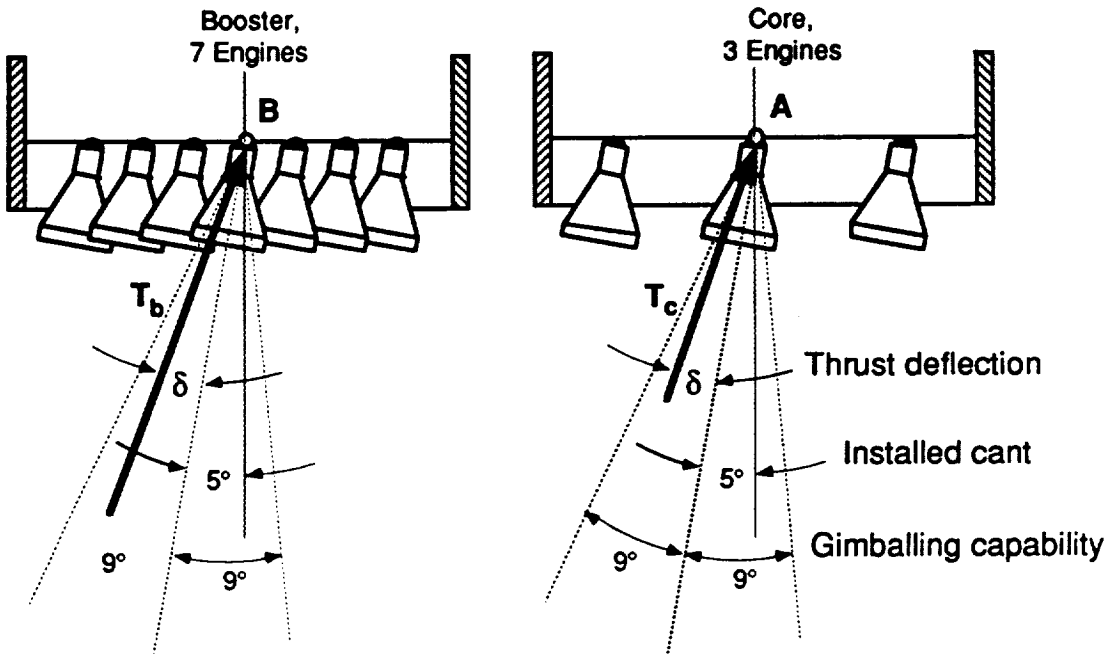

NOTES

1) All 10 engines are installed with a 5° cant.
2) All 10 engines have the same gimballing capability of ± 9° from installed cant.
3) Resultant thrust vector of core, T_c, acts through point **A**.
4) Resultant thrust vector of booster, T_b, acts through point **B**.

Figure 2.2: Thrust Model

It was further assumed that both thrust vectors will be deflected by the same angle, δ. This angle is computed by the flight control system so that the vehicle can maintain control while steering to the trajectory commanded by the guidance system.

2.2 Mass Properties

To simulate the linear and angular acceleration of the vehicle during flight, knowledge is required of the time-varying mass properties: mass (m), cg position, and moment of inertia. The mass decreases as fuel is expended. As the mass is decreased, the cg position and moment of inertia change. It has been assumed in this thesis that the motion of the ALS vehicle is constrained to lie in the pitch plane. Therefore, only the pitch plane components of cg location (x_{cg} and z_{cg}) are required and only the moment of inertia about the pitch axis (I_{yy}) is required.

A calculation of the dry mass properties is computed before launch and is combined with the initial fuel mass properties to give a total vehicle mass property calculation before lift-off. The mass properties can then be updated continuously during flight since mass flow rate is assumed to be constant .

The dry model used is the same as that developed by Boelitz, based upon recommendations from NASA. The vehicle is separated into various geometric solids and shells. All components were assumed to have uniform mass density.

The fuel tanks in both the core and the booster were modelled as hollow shells with the fuel inside modeled as a solid cylinder with time-varying length. The engine modules and payload bay were modeled as solid cylinders. The dry mass properties are presented in Table 2.2 below:

Vehicle Component:	m (slugs)	x_{cg} (ft)	z_{cg} (ft)	I_{yy} (slug ft^2)
Core	10,924	138.0	0	56,872,200
Booster	5,781	63.5	0	16,945,000
TOTAL:	16,705	112.2	-11.1	98,671,000

Table 2.2: Dry Mass Properties (Datum at base of core)

2.3 Aerodynamic Characteristics

In order to compute the aerodynamic forces and moment in the pitch plane, it is necessary to know the coefficients of aerodynamic normal and axial force. These coefficients are vehicle dependent and are functions of both Mach number and angle of attack. NASA provided CSDL with updated aerodynamic data in 1989. Lift, drag, and moment coefficients were provided for 0<Mach<8 and for angles of attack between -14° and +14°. The vehicle simulations used in this study interpolated between these data points to obtain coefficients for the current vehicle state. Linear interpolation was used between consecutive Mach numbers and cubic spline interpolation was used between consecutive angle of attack values.

2.4 Environmental Conditions

In addition to the aerodynamic coefficients described above, knowledge is required of the atmospheric model (pressure, density, and speed of sound) and of the winds to determine the aerodynamic forces. The vehicle simulations used in this study implement the equations for atmospheric pressure, density, and speed of sound given in the 1976 US Standard Atmosphere. These parameters are all defined as functions of altitude with a range of 0 to 282,000 feet. Above this range, the air density and pressure are assumed to be zero and the speed of sound is assumed to be the same as the vacuum speed of sound.

It is assumed in this thesis that the A.L.S. vehicle will not be capable of sensing winds during flight. The winds will be measured one half hour before launch using the Jimsphere radar-tracked balloon system. It is assumed that this is the only wind information that can be used in trajectory design, both before launch and during flight.

For this study, NASA provided a wind profile from Vandenberg AFB. A certain percentage of the wind profile is used for trajectory design before launch, and a different percentage of the wind profile is used for the in-flight simulation. The goal of this variation

is to test the guidance system for robustness in the presence of unexpected wind disturbances.

Because this study is limited to the pitch plane, the winds were assumed to lie in the pitch plane and act in a direction that is parallel to the local Earth-relative horizontal. Also, the wind profiles were linearized using straight line approximations between a finite number of data points. The profile used by this study and its linearized approximation is shown in Appendix A. In this profile, the winds dissipated above 66,000 ft.

2.5 Coordinate Frames and Kinematics

Three reference frames are used in this study to simulate the motion of the vehicle about a spherical Earth. They are defined as:

(1) Inertial Earth-Centered Reference Frame: (**X**, **Y**, **Z**)

All equations of motion are referred to this non-rotating reference frame. The origin is at the center of the earth. The **Z** axis points through the North Pole. The **X** axis points through zero longitude and the **Y** axis completes the right-handed set.

(2) Local Geographic Frame: ($\mathbf{u_N}$, $\mathbf{u_E}$, $\mathbf{u_G}$)

The origin is at the center of gravity of the vehicle. The positive $\mathbf{u_G}$ axis points towards the center of the earth. The $\mathbf{u_N}$ axis lies on the plane formed by the **Z** axis and $\mathbf{u_G}$ and points north. The $\mathbf{u_E}$ axis completes the right-handed set. The wind directions and all earth-relative angles are calculated within this reference frame.

(3) Body-Fixed Frame: (x_B, y_B, z_B)

The origin of this frame is fixed to the vehicle's center of gravity and assumes there will be no rotation of the vehicle about the x_B axis. As stated earlier, this thesis constrains the vehicle to unrolled motion in the pitch plane. The x_B axis is parallel to the centerline of the vehicle and points towards the nose cone. The y_B axis is in the direction of the cross product of u_G and x_B. The z_B axis completes the right-handed set. All forces and torques on the vehicle are computed in this frame.

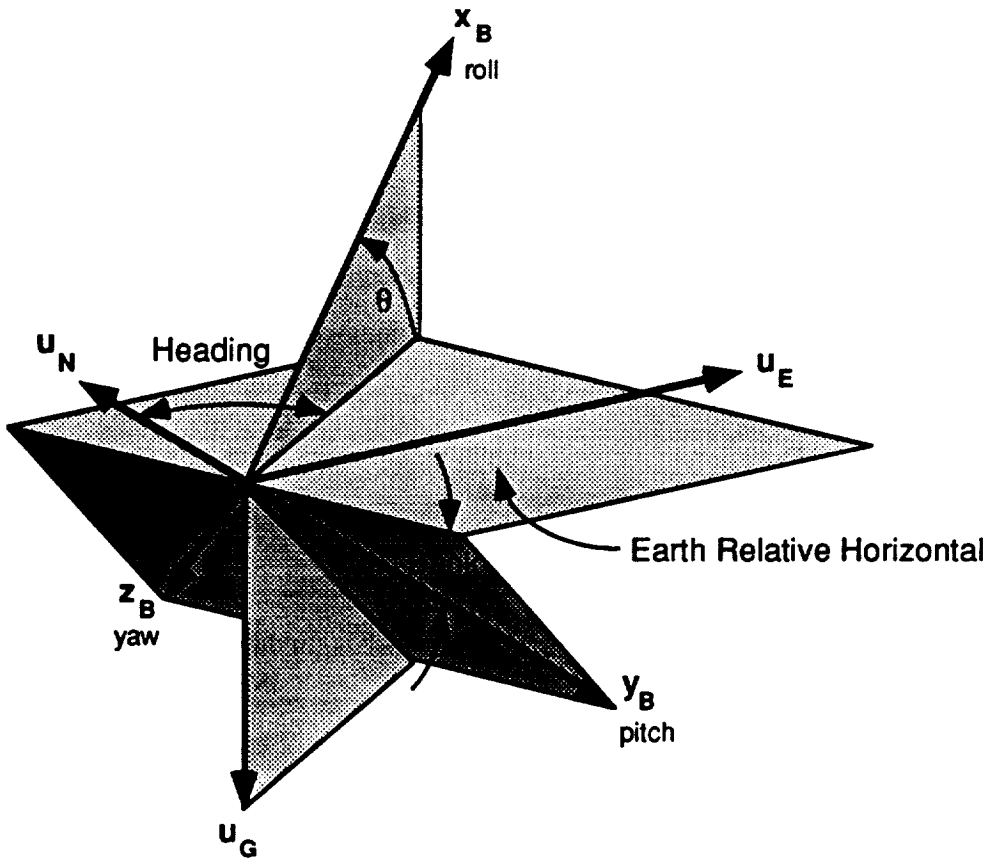

Figure 2.3: Relationship Between Body and Local Geographic Frames

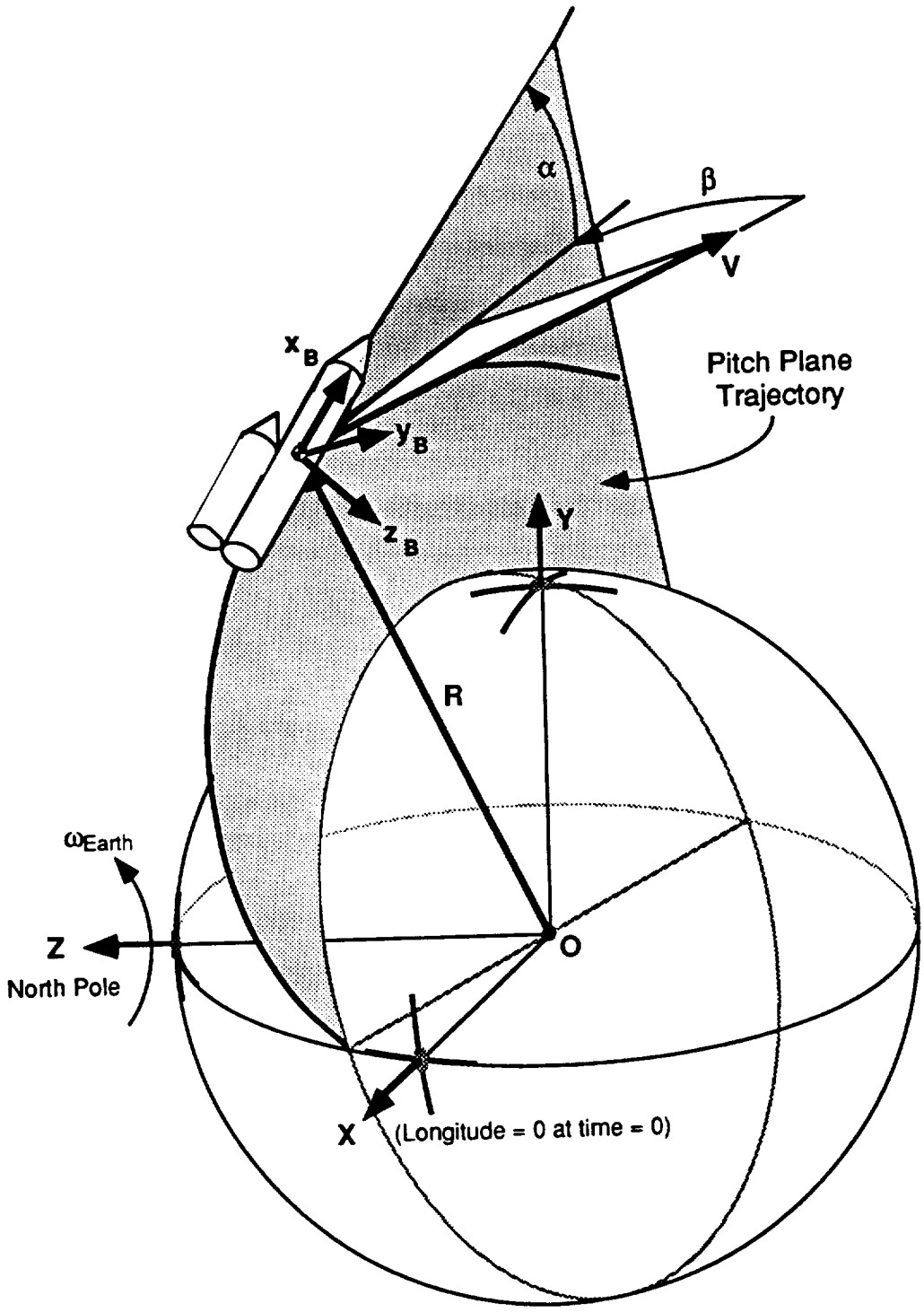

Figure 2.4: Inertial and Body Frame Relationship With Pitch Plane

The relationship between the body and local geographic reference frames is shown in Figure 2.3. Again, because this study is concerned only with the pitch plane dynamics, the heading is determined solely from the initial launch azimuth and the bank angle is set to zero. The Earth-relative pitch attitude is the only variable of interest.

The relationship between the inertial and the body reference frames and the pitch plane is illustrated in Figure 2.4. The angle of attack with respect to the Earth-relative velocity, α, and the sideslip angle, β, are also depicted in this figure.

The rotation of the inertial frame into the body frame was described by an Euler angle set, (Ψ, Θ, Φ) representing a sequential azimuth, elevation, and bank transformation. This transformation is described in Etkin. The rotation matrix obtained using this transformation is:

$$[C] = \begin{bmatrix} \cos\Theta\cos\Psi & \cos\Theta\sin\Psi & -\sin\Theta \\ \sin\Phi\sin\Theta\cos\Psi - \cos\Phi\sin\Psi & \sin\Phi\sin\Theta\sin\Psi + \cos\Phi\cos\Psi & \sin\Phi\cos\Theta \\ \cos\Phi\sin\Theta\cos\Psi + \sin\Phi\sin\Psi & \cos\Phi\sin\Theta\sin\Psi - \sin\Phi\cos\Psi & \cos\Phi\cos\Theta \end{bmatrix} \tag{2.1}$$

The rotation matrix is used to resolve the components of a vector known in the inertial frame into the body-fixed frame and vice-versa. If a vector **B** is known in the inertial frame such that:

$$\mathbf{B} = x_I\,\mathbf{u}_{XI} + y_I\,\mathbf{u}_{YI} + z_I\,\mathbf{u}_{ZI} = x_B\,\mathbf{u}_{XB} + y_B\,\mathbf{u}_{YB} + z_B\,\mathbf{u}_{ZB} \tag{2.2}$$

but the components x_B, y_B, and z_B are not known, then these components can be determined from the following relation:

$$\begin{Bmatrix} x_B \\ y_B \\ z_B \end{Bmatrix} = [C] \begin{Bmatrix} x_I \\ y_I \\ z_I \end{Bmatrix} \tag{2.3}$$

The rotation matrix, $[C]$, is orthogonal so that $[C]^{-1} = [C]^{T}$. Therefore, a vector which is known in the body-fixed frame can be expressed in the inertial frame with the relation:

$$\begin{Bmatrix} x_I \\ y_I \\ z_I \end{Bmatrix} = [C]^T \begin{Bmatrix} x_B \\ y_B \\ z_B \end{Bmatrix} \tag{2.4}$$

2.6 Dynamics and Rigid Body Equations

Figure 2.5 shows the angular rate and moment notation used for the body-fixed frame where:

L = rolling moment	ω_r = rate of roll
M = pitching moment	ω_p = rate of pitch
N = yawing moment	ω_y = rate of yaw

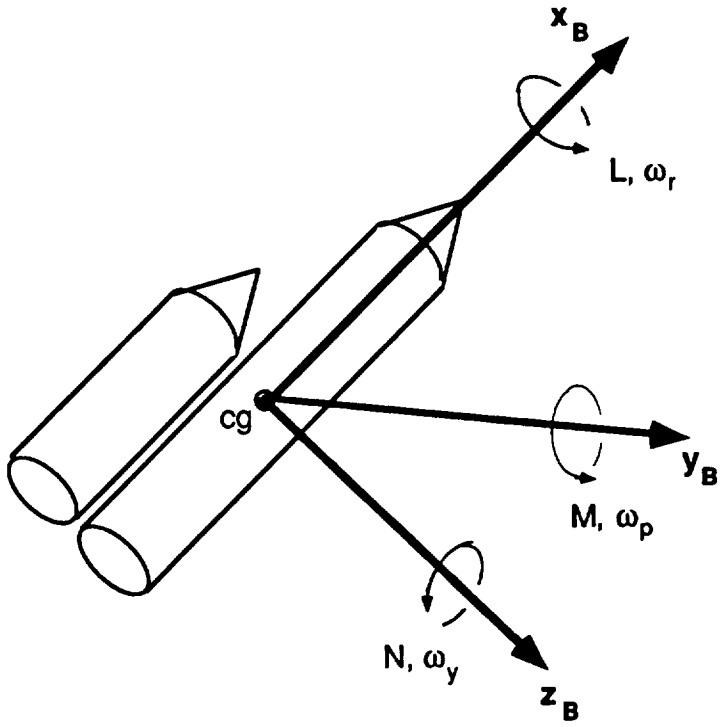

Figure 2.5: Angular Rates in Body Frame

Since this study is limited to the pitch-plane motion, it was assumed that the vehicle experiences no roll or yaw torques:

$$L = N = 0 \tag{2.5}$$

The roll and yaw rates are therefore also zero:

$$\omega_r = \omega_y = 0 \tag{2.6}$$

and the sideslip angle, β, is zero.

2.6.1 Flight Orientation Parameters

The following flight orientation parameters, pictured in Figure 2.6, are used to describe the state of the vehicle in the trajectory plane:

θ = earth-relative pitch attitude

α = angle of attack with respect to the air-relative velocity

α_E = angle of attack with respect to the Earth-relative velocity

α_W = angle of attack contribution from winds = $\alpha - \alpha_E$

γ = flight path angle

$\mathbf{V_E}$ = Earth-relative velocity

$\mathbf{V_W}$ = wind velocity

$\mathbf{V_A}$ = air-relative velocity = $\mathbf{V_E} - \mathbf{V_W}$

The air-relative velocity is the difference between the Earth-relative velocity and the wind velocity. The angle of attack with respect to the air-relative velocity is equal to the sum of the Earth-relative angle of attack and the angle of attack produced by winds. The angle of attack contribution from winds is defined as positive if the cross product of $\mathbf{V_A}$ with $\mathbf{V_E}$ points in the positive y_B direction. The angle of attack with respect to the air-relative velocity is used in the calculation of the aerodynamic coefficients.

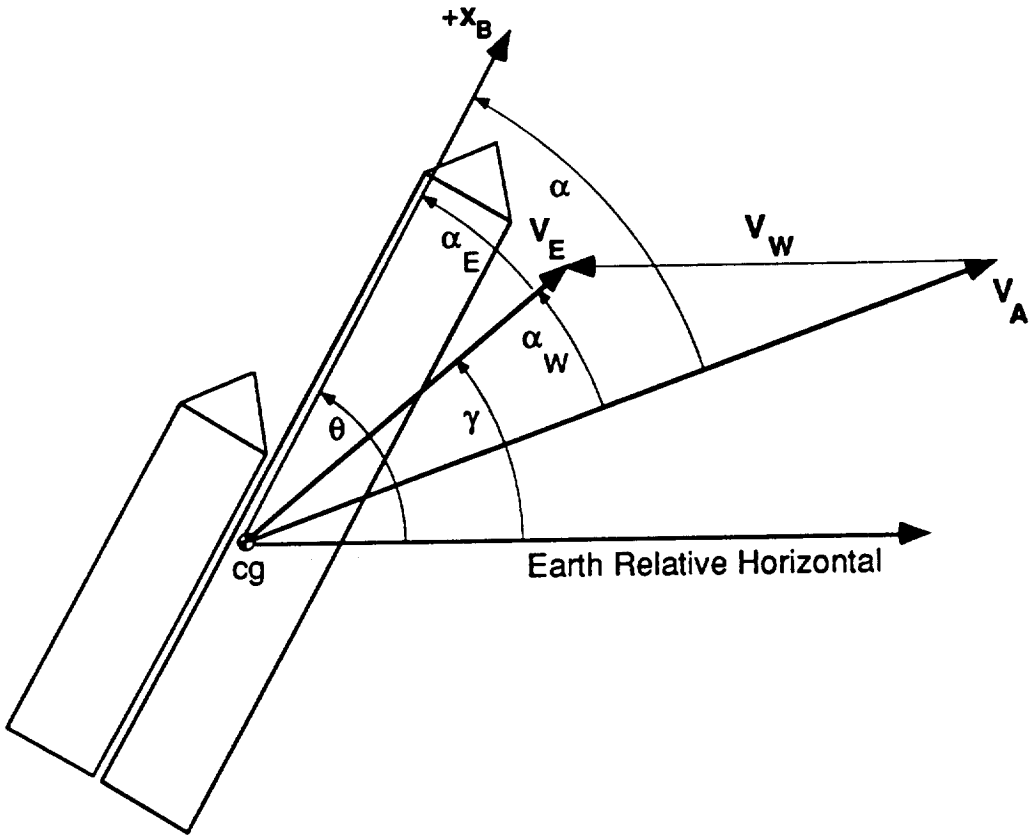

Figure 2.6: Flight Orientation Parameters

2.6.2 Forces and Torques

The forces that act on the vehicle during endoatmospheric flight are: the thrust forces ($\mathbf{T_b}$ and $\mathbf{T_c}$), the aerodynamic forces ($\mathbf{F_N}$ and $\mathbf{F_A}$), and the force of gravity ($\mathbf{F_g}$). A free body diagram of the vehicle in the pitch plane is given in Figure 2.7.

The aerodynamic force acts at the vehicle center of pressure and can be resolved into the body-fixed coordinate frame. For an unrolled vehicle with zero sideslip angle, the normal aerodynamic force acts in the $-\mathbf{z_B}$ direction and the axial aerodynamic force acts in $-\mathbf{x_B}$ direction. These forces can be written in the body-fixed frame as:

$$\mathbf{F_N} = - S\, Q\, C_N\, \mathbf{u_{ZB}} \tag{2.7}$$

$$\mathbf{F_A} = - S\, Q\, C_A\, \mathbf{u_{XB}} \tag{2.8}$$

where:

S = reference area = constant

Q = dynamic pressure = $\rho V_A^2 / 2$

ρ = air density

V_A = magnitude of air-relative velocity

C_N = coefficient of aerodynamic normal force = $C_N(\alpha, \text{Mach})$

C_A = coefficient of aerodynamic axial force = $C_A(\alpha, \text{Mach})$

$\mathbf{u_{ZB}}$ = unit vector in z-direction of body-fixed frame

$\mathbf{u_{XB}}$ = unit vector in x-direction of body-fixed frame

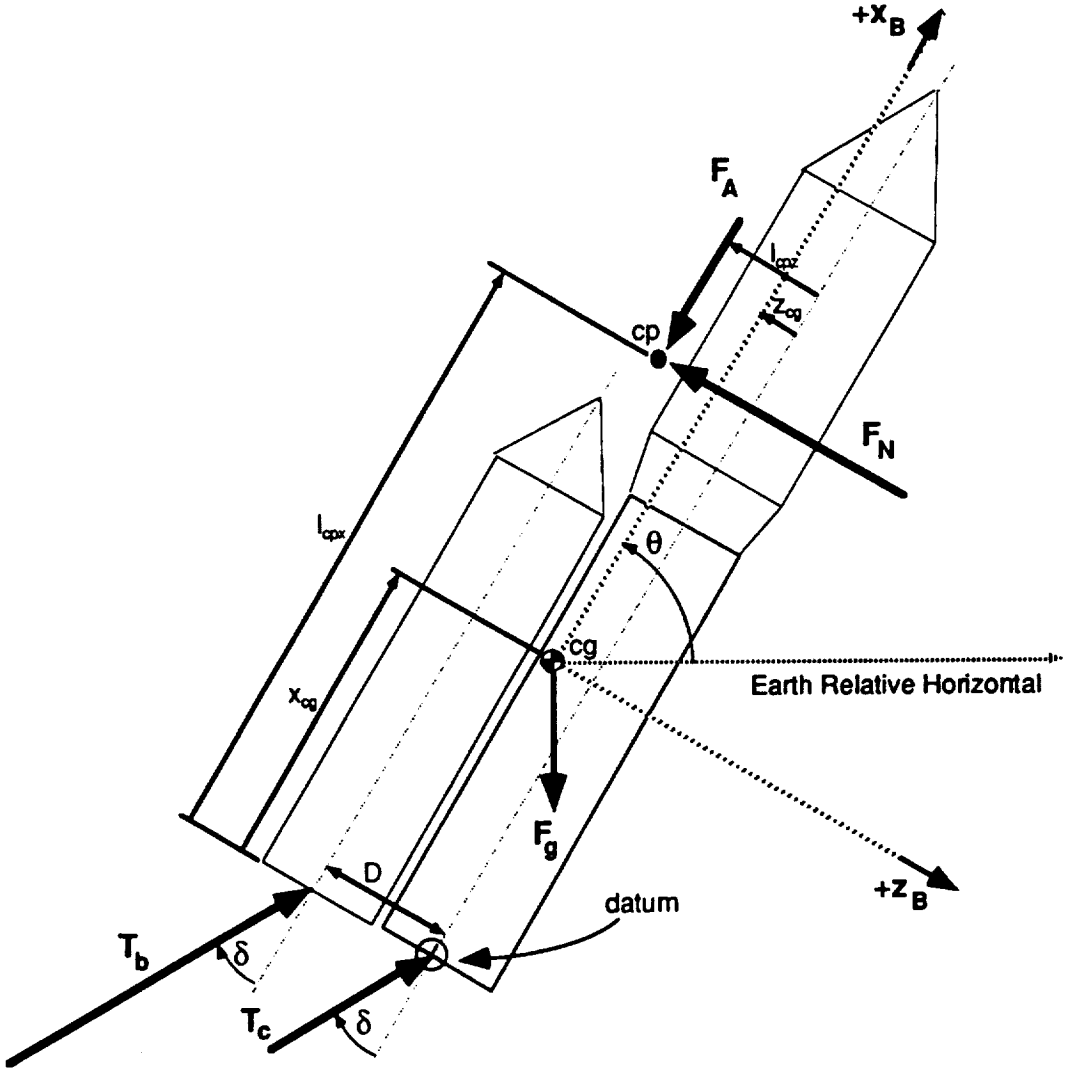

Figure 2.7: Vehicle Free Body Diagram in the Pitch Plane

The aerodynamic pitching moment is expressed in a similar form:

$$M_{AERO} = S\,Q\,C_N\,(l_{cpx} - x_{cg}) + S\,Q\,C_A\,(-l_{cpz} + z_{cg}) \tag{2.9}$$

where:

l_{cpx} = location of center of pressure with respect to datum

l_{cpz} = location of center of pressure with respect to centerline of core

For this study, both l_{cpx} and l_{cpz} were assumed to be constants.

The two thrust forces, $\mathbf{T_b}$ and $\mathbf{T_c}$, are expressed in the body-fixed frame as:

$$\mathbf{T_b} = T_b \cos\delta\ \mathbf{u_{XB}} + T_b \sin\delta\ \mathbf{u_{ZB}} \tag{2.10}$$

$$\mathbf{T_c} = T_c \cos\delta\ \mathbf{u_{XB}} + T_c \sin\delta\ \mathbf{u_{ZB}} \tag{2.11}$$

where:

T_b = booster thrust

T_c = core thrust

δ = nozzle deflection

The thrust contribution to the pitching moment exerted on the vehicle is:

$$M_{THRUST} = T_b\,x_{cg} \sin\delta + T_c\,x_{cg} \sin\delta - T_b\,(D + z_{cg}) \cos\delta - T_c\,z_{cg} \cos\delta \tag{2.12}$$

where:

x_{cg} = body x-axis cg position (measured from datum at base of core) ≥ 0

z_{cg} = body z-axis cg position (measured from centerline of core) ≤ 0

D = distance between centerlines of core and booster = constant

The force of gravity points toward the center of the Earth along $\mathbf{u}_G$ and can be expressed in the inertial frame as:

$$\mathbf{F_g} = - m\, g\, (\mathbf{R}/R) \tag{2.13}$$

where:

$\mathbf{R}$ = position vector of vehicle expressed in inertial coordinates

R = magnitude of inertial position vector

$m = m(t)$ = vehicle mass at time t

2.6.3 Rigid Body Equations of Motion

The forces acting on the vehicle can be summed in the body-fixed frame to give the resultant force in body-fixed coordinates:

$$\mathbf{F_{NET}} = \mathbf{F_N} + \mathbf{F_A} + \mathbf{T_b} + \mathbf{T_c} + \mathbf{F_g} \tag{2.14}$$

This force can be resolved into the inertial frame by the use of equation 2.4. The translational equations of motion are then:

$$\frac{d\mathbf{R}}{dt} = \mathbf{V} \tag{2.15}$$

$$\frac{d\mathbf{V}}{dt} = \left(\frac{1}{m}\right) \mathbf{F}_{\mathrm{NET}} \tag{2.16}$$

The rotational equations of motion are calculated using the angular momentum principle:

$$\mathbf{M} = \frac{d([I]\omega)}{dt} = \frac{\partial([I]\omega)}{\partial t}_{\substack{\text{relative to} \\ \text{body frame}}} + \omega \times [I]\omega \tag{2.17}$$

This set of equations can be expanded into the following:

$$\mathbf{M} = \frac{\partial [I]}{\partial t}\omega + [I]\frac{\partial \omega}{\partial t} + \omega \times [I]\omega \tag{2.18}$$

where M is the total moment acting on the vehicle and is expressed in the body-fixed frame as:

$$\mathbf{M} = \begin{Bmatrix} L \\ M \\ N \end{Bmatrix} \tag{2.19}$$

and ω is the angular velocity of the body expressed in the body-fixed frame as:

$$\vec{\omega} = \begin{Bmatrix} \omega_r \\ \omega_p \\ \omega_y \end{Bmatrix} \tag{2.20}$$

and $[I] = [I(t)]$ = vehicle inertia at time t

To simplify equation 2.18, two assumptions can be made. First, the body-fixed axes are assumed to form a principal axes set for the vehicle so that the inertia matrix, $[I]$, is diagonal. Second, the term that consists of the product of the time derivative of inertia with angular rate was found to form a very small contribution to the total moment and was therefore neglected. Using these assumptions, equation 2.18 can be written in scalar form as:

$$L = I_{xx}\frac{d\omega_r}{dt} - \omega_p\omega_y(I_{yy} - I_{zz}) \tag{2.21}$$

$$M = I_{yy}\frac{d\omega_p}{dt} - \omega_y\omega_r(I_{zz} - I_{xx}) \tag{2.22}$$

$$N = I_{zz}\frac{d\omega_y}{dt} - \omega_r\omega_p(I_{xx} - I_{yy}) \tag{2.23}$$

These equations are known as Euler's equations of motion. However, we stated earlier that: the rolling moment, yawing moment, rate of roll, and rate of yaw are all equal to zero:

$$L = N = \omega_r = \omega_y = 0 \tag{2.24}$$

Therefore, equations 2.21 and 2.23 are both trivial and equation 2.22 simplifies to:

$$\frac{d\,\omega_p}{dt} = I_{yy}^{-1}\, M \tag{2.25}$$

where the pitching moment, M, acting on the vehicle is the sum of the contributions from the thrust forces and from the aerodynamic forces:

$$M = M_{AERO} + M_{THRUST} \tag{2.26}$$

The Euler angle rates are then calculated from the body rates by the use of the following non-orthogonal rate transformation matrix:

$$[W] = \begin{bmatrix} 1 & \sin\Phi\tan\Theta & \cos\Phi\tan\Theta \\ 0 & \cos\Phi & -\sin\Phi \\ 0 & \sin\Phi\sec\Theta & \cos\Phi\sec\Theta \end{bmatrix} \tag{2.27}$$

Using this transformation matrix, the time rate of change of the Euler angle set which describes the attitude of the vehicle with respect to the inertial frame is given by:

$$\frac{d}{dt}\begin{bmatrix}\Phi\\ \Theta\\ \Psi\end{bmatrix} = [W]\begin{bmatrix}\omega_r\\ \omega_p\\ \omega_y\end{bmatrix} \tag{2.28}$$

where:

$\omega_r = \omega_y = 0$ for all time t (assumption made for pitch plane analysis)

ω_p = body pitchrate = $d\theta/dt$

In summary, the equations of motion implemented in the six degree of freedom simulation used for this thesis are:

Translational:

$$\frac{d\mathbf{R}}{dt} = \mathbf{V} \tag{2.29}$$

$$\frac{d\mathbf{V}}{dt} = \left(\frac{1}{m}\right)\mathbf{F}_{NET} \tag{2.30}$$

Rotational:

$$\frac{d\,\omega_p}{dt} = I_{yy}^{-1}\,M \tag{2.31}$$

$$\frac{d}{dt}\begin{bmatrix}\Phi\\ \Theta\\ \Psi\end{bmatrix} = [W]\begin{bmatrix}\omega_r\\ \omega_p\\ \omega_y\end{bmatrix} \tag{2.32}$$

2.7 Constraints

The normal aerodynamic force can produce a large bending moment on the vehicle.as the vehicle moves through the atmosphere. Structurally, there is a limit on the magnitude of the bending moment that the vehicle can sustain without failure. Therefore, it is necessary to constrain the normal aerodynamic force during flight.

Recalling equation 2.7, the magnitude of the normal aerodynamic force can be expressed as:

$$F_N = S\,Q\,C_N \tag{2.33}$$

where:

S = reference area = constant

Q = dynamic pressure = $\rho V_A^2 / 2$

ρ = air density

V_A = magnitude of air-relative velocity

C_N = coefficient of normal aerodynamic force = $C_N(\alpha, \text{Mach})$

For small values of angle of attack, the coefficient of normal aerodynamic force can be approximated as a linear function of angle of attack. Given this approximation, the coefficient can be expressed as:

$$C_N \approx C_{N\alpha}\,\alpha \tag{2.34}$$

where:

$$C_{N\alpha} = \left[\frac{\partial C_N}{\partial \alpha}\right] \tag{2.35}$$

The normal aerodynamic force can then be approximated by:

$$F_N \approx S\,Q\,C_{N\alpha}\,\alpha \tag{2.36}$$

Since S is a constant and $C_{N\alpha}$ is approximately equal to a constant, the normal aerodynamic force is roughly proportional to the product of dynamic pressure, Q, and the angle of attack, α. Therefore, to control the normal aerodynamic force, the vehicle is usually controlled to limit the product of Q and α. A limit on $Q\alpha$ has been specified by the designers of the A.L.S. vehicle. This limit is the primary constraint on the vehicle's trajectory during endoatmospheric flight.

The dynamic pressure is proportional to the product of air density, ρ, and the square of the magnitude of the air-relative velocity, V_A. The air-relative velocity monotonically increases from zero during flight while the air density monotonically decreases with altitude. The result of these effects is that the dynamic pressure rises from zero to a maximum within the atmosphere and then decreases back to zero when the vehicle has left the Earth's atmosphere. A typical dynamic pressure profile showing this behavior is illustrated in Figure 2.8.

There are several methods which have been developed to control the $Q\alpha$ product so that the constraint on normal aerodynamic force is not exceeded. Corvin, in his Shuttle II study, used the throttling capability of that vehicle's engines to control velocity and thus dynamic pressure. Boelitz, in the initial A.L.S. study, used an angle of attack limiting mode within the control system. Both Corvin and Boelitz found that appropriate trajectory shaping could also help to keep the $Q\alpha$ product below the specified limit.

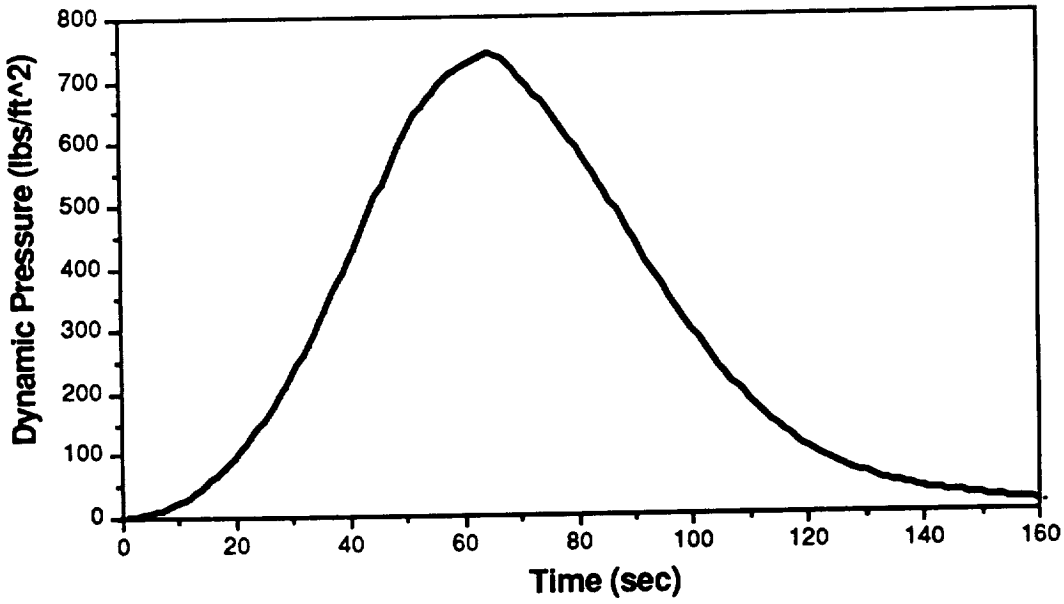

Figure 2.8: Typical Dynamic Pressure Profile

Chapter Three

TRAJECTORY DESIGN, GUIDANCE, AND CONTROL CONCEPTS

3.1 Introduction

The new trajectory design and guidance concepts developed in this study are based upon those developed by Boelitz. Trajectory design is the process of choosing a trajectory, based upon objectives and constraints, for the guidance system to command during flight. Boelitz's objective for the trajectory design of the guidance commands was to achieve as high an "on-orbit mass" as possible while constraining the vehicle to fly within the designer specified $Q\alpha$ limit. The "on-orbit mass" is defined as the mass of the vehicle when it has just been inserted into the desired, elliptical orbit. An advantage of maximizing on-orbit mass is that it allows more fuel to be available for any post boost maneuvers. Also, minimizing the fuel needed for endoatmospheric boost will allow the A.L.S. to carry larger payloads into orbit.

A disadvantage of the Boelitz study was that the guidance was implemented in an open-loop manner such that the trajectory was not updated during flight. Consequently, if wind dispersions from the pre-launch measurement occur or if an engine-out failure occurs, then the trajectory designed before flight might not be optimal for on-orbit mass. In this thesis, an attempt is made to update the trajectory during flight using the vehicle's current state, a predictive simulation for on-orbit mass, and a numerical optimization scheme to maximize for on-orbit mass. The control and estimation concepts used in this thesis are the same as those used in the previous study.

This chapter reviews the work done by Boelitz and introduces the improvements that are made in trajectory design and guidance. Section 3.2 describes the mission of the vehicle and how its flight is divided into separate phases. Each phase necessitates the use

of different guidance and control schemes. Section 3.3 describes which signals can be sensed and which signals must be estimated. This section then reviews the estimators that Boelitz used for angular velocity, angle of attack, dynamic pressure, and acceleration direction. The guidance and control concepts used in flight are discussed in Section 3.4. Section 3.5 reviews the pre-launch trajectory design profiles and methods for each phase. Finally, Section 3.6 introduces the method for automating the pre-launch trajectory design and updating the trajectory in flight.

3.2 Mission and Flight Phases

The A.L.S. must be able to carry payloads through the atmosphere to a low-Earth parking orbit. The amount of lead-time and planning for the mission must be kept to a minimum. The vehicle must also have the capability to tolerate wind dispersions from pre-launch measurements and still have enough fuel left after atmospheric ascent to maneuver into the desired parking orbit.

The ascent trajectory of the A.L.S. can be divided into four distinct phases. Each phase involves different constraints and thus different guidance and control schemes. A schematic of the ascent is shown in Figure 3.1.

Phase 1 is a vertical rise from the launch pad so that the vehicle can clear the launch tower. The pitch attitude of the vehicle during this phase must be held constant at 90°. Attitude control is thus used to meet this objective.

Phase 2 is characterized by a rapid pitchover designed to orient the vehicle to the initial state required by Phase 3. The state required at the start of Phase 3 is very different from the state achieved at the end of Phase 1. Therefore, Phase 2 must quickly pitch over the vehicle while the dynamic pressure, Q, is still small enough so that the $Q\alpha$ product remains well below the designer specified $Q\alpha$ limit. The guidance profile used in this phase is based on pitch attitude rate calculated as an analytical function of time.

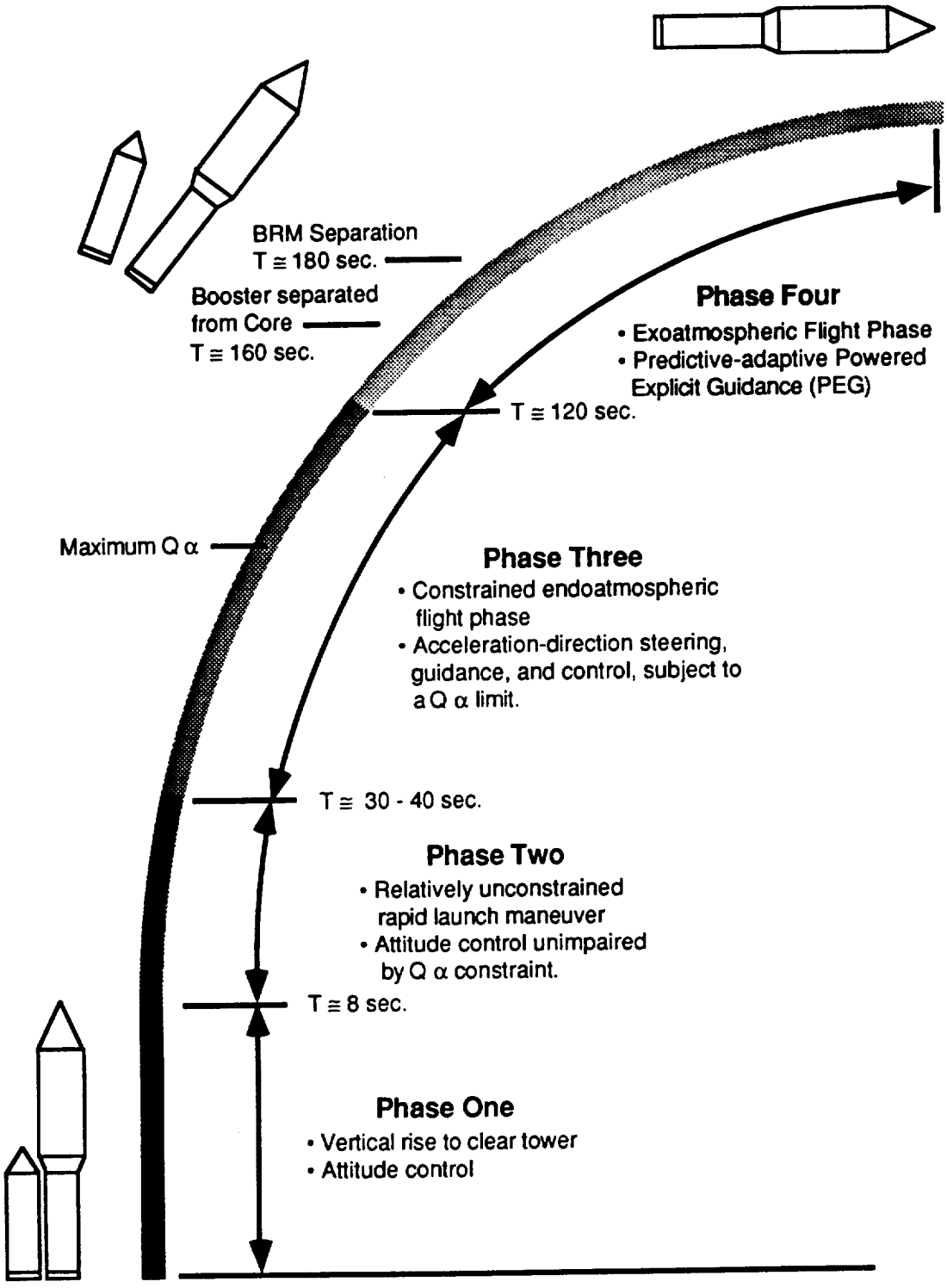

Figure 3.1: A.L.S. Flight Phases

Phase 3 is the endoatmospheric phase during which the trajectory may be constrained by the $Q\alpha$ limit. The $Q\alpha$ product reaches its maximum during this stage and could rise above the specified $Q\alpha$ limit if it were not constrained. During this phase, the guidance command profile is a stored acceleration-direction trajectory. A dual-mode control system is used that will follow the acceleration-direction profile if the $Q\alpha$ product is below the specified limit, but will switch to a $Q\alpha$ limiting control mode if the $Q\alpha$ product is above the limit.

Phase 4 begins when the atmospheric density has fallen to a sufficiently small value so that the dynamic pressure is low once again. The transition from endoatmospheric to exoatmospheric flight occurs during this phase. A modification of the Space Shuttle Powered Explicit Guidance system (PEG) is used to guide the vehicle. Because Phase 4 starts in the upper atmosphere, the PEG algorithm neglects aerodynamic forces. At the end of this phase, the vehicle is inserted into low Earth orbit. The specified parameters for this orbit are:

(1) Radius of perigee = r_{pe} = 80 nautical miles

(2) Radius of apogee = r_{ap} = 150 nautical miles

(3) Horizontal velocity at perigee:

$$V_{perigee} = \left[\frac{2\mu \left(\frac{r_{ap}}{r_{pe}} \right)}{r_{ap} + r_{pe}} \right]^{1/2}$$

where μ = gravitational constant

3.3 In-Flight Guidance and Control

This section presents a review of the guidance and control concepts developed by Boelitz in the previous A.L.S. study. This thesis involves modifications of the guidance but does not attempt to improve on the control concepts. The control loops and estimators used in this study are therefore the same as used in the previous study.

3.3.1 Phase 1 and 2 Guidance and Control

Figure 3.2 shows a general block diagram describing the guidance and control for both Phase 1 (vertical rise) and Phase 2 (launch maneuver). The guidance commands of both Phase 1 and Phase 2 are based on pitch attitude rate, ω_c. For Phase 1 the vehicle must rise vertically to clear the tower and so:

$$\begin{aligned} &\omega_c(t) = 0 \\ &\theta_{c_{INIT}} = 90^\circ \\ &\theta_c(t) = \theta_{c_{INIT}} = 90^\circ \end{aligned} \tag{3.1}$$

For Phase 2, the vehicle must start at the final conditions for Phase 1 and then orient itself to meet the starting conditions for Phase 3. Corvin and Boelitz both used a sinusoidal pitch attitude rate for this purpose whose form is given by the following relation:

$$\omega_c(t) = \Omega\left\{ 1 - \cos\left[\frac{2\pi}{T_{Kick}}\,(t - T_{Vert})\right]\right\}\Bigg|_{T_{Vert} \le t \le T_{Kick} + T_{Vert}} \tag{3.2}$$

where:

Ω = half the maximum pitch rate

T_{Vert} = duration of Phase 1 (time required for vehicle to clear launch tower)

T_{Kick} = duration of Phase 2

The shape of this maneuver is shown in Figure 3.3. Both Ω and T_{Kick} are constants determined by the trajectory design process discussed in the next section. With this analytical function, the integration of ω_c shown in Figure 3.2 can be performed analytically giving the following relation for commanded pitch attitude:

$$\theta_c(t) = \Omega\left\{ (t - T_{Vert}) - \frac{T_{Kick}}{2\pi}\sin\left[\frac{2\pi}{T_{Kick}}\,(t - T_{Vert})\right]\right\} + \theta_{c_{INIT}}\Bigg|_{T_{Vert} \le t \le T_{Kick} + T_{Vert}} \tag{3.3}$$

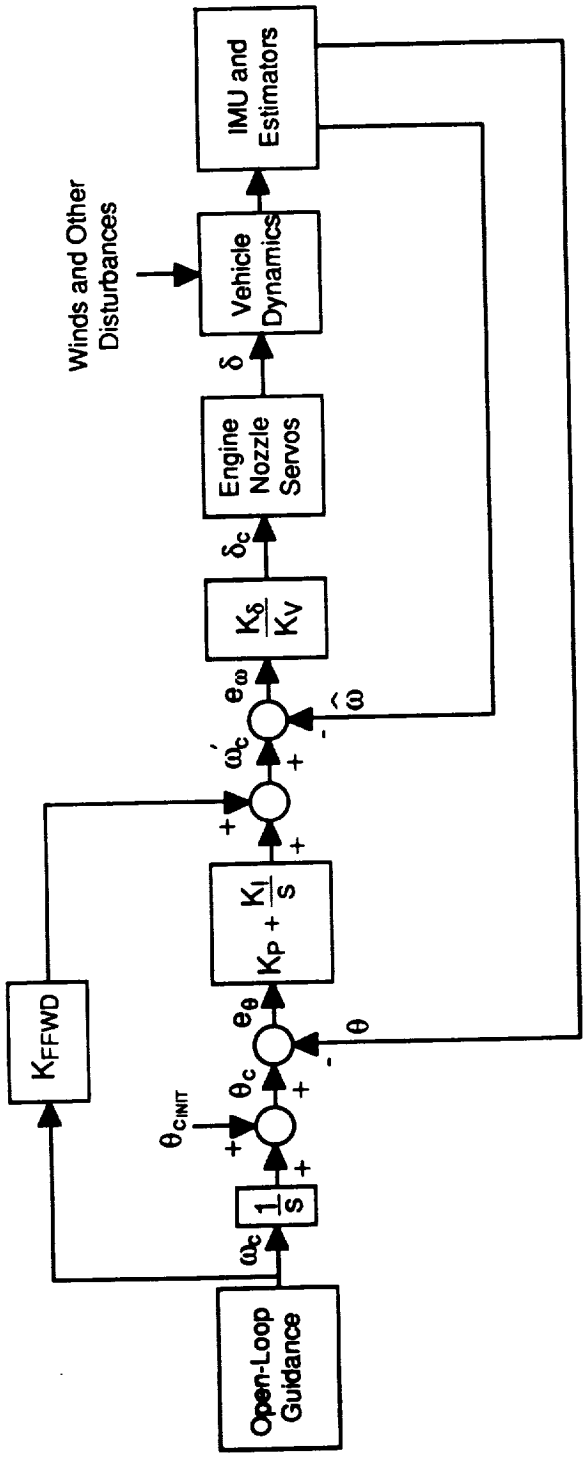

Figure 3.2: Phase 1 and 2 Guidance and Control Block Diagram

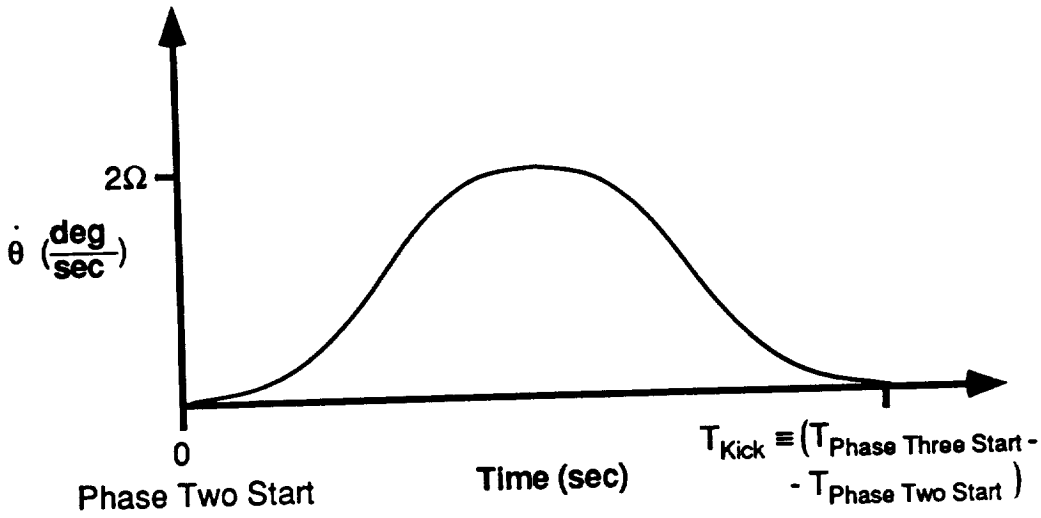

Figure 3.3: Phase 2 Attitude Rate Profile

Referring again to Figure 3.2, the guidance employed in both Phase 1 and Phase 2 is open-loop, meaning that the guidance commands to the control system are designed prior to launch and are not updated during flight. This study did not attempt to close the guidance loop during Phase 1 and 2 because it was decided that the altitude of the vehicle during both of these phases was sufficiently low so that wind dispersions were not a serious problem.

The attitude commands generated by the open-loop guidance system are fed directly into the control system which tries to null the error between the commanded attitude and the sensed attitude, e_θ. The attitude error is compensated by proportional-integral control. The resulting signal is then summed with the fed-forward commanded pitch rate, ω_c, to produce a net pitch rate command, ω_c'. This signal is compared to the estimated pitch rate resulting in a pitch rate error signal, e_ω.

This error signal is multiplied by a proportional gain, K_δ/K_V, to provide an engine nozzle angle command to the engine nozzle servos. Boelitz linearized the vehicle dynamics, using the assumption of a planar trajectory, to find a transfer function between engine nozzle deflection, δ, and pitch attitude, θ. On the basis of this linearization, the gain of this vehicle dynamics transfer function is approximately K_V where:

$$K_V = \frac{T\, x_{cg}}{I_{yy}} \tag{3.4}$$

This is a quantity which monotonically increases with time. Therefore, K_V, is used in the denominator of the proportional gain to keep the total inner loop forward gain constant.

For this thesis, the engine nozzle servos were idealized such that the commanded nozzle deflection was perfectly achieved:

$$\delta = \delta_c \tag{3.5}$$

3.3.2 Phase 3 Guidance and Control

Traditionally, launch vehicles have used "acceleration direction" steering for this phase of flight. The "acceleration direction" is the inertial acceleration of the vehicle excluding the acceleration caused by gravity. The control loop is commanded to follow either an acceleration direction or a pitch attitude command from the guidance system. In addition to the nominal acceleration direction (or attitude) and attitude rate feedback signals in the control loop, a parallel "load relief" signal is added. This add-on load relief employs a signal proportional to the measured ΔV component acting normal to the vehicle's longitudinal axis. At low frequencies, this signal is approximately proportional to the angle of attack. The effect of the add-on load relief is to rotate the vehicle in the direction of the air-relative velocity vector and thereby reduce the angle of attack. The disadvantage of the add-on load relief concept is that the load relief is in conflict with the acceleration direction control and can produce significant deviations from the desired trajectory in the presence of winds. The control concept used in this thesis is one which overcomes some of the disadvantages of the traditional load-relief concept. It is a dual mode, acceleration direction/$Q\alpha$-limiting guidance and control scheme that was first developed by Bushnell. Boelitz later applied the concept to the A.L.S. vehicle in his study.

A general block diagram for Phase 3 acceleration direction/$Q\alpha$-limiting guidance and control is shown in Figure 3.4. The control system has two modes. In the primary mode, the vehicle's "sensed" acceleration is commanded to follow a stored acceleration direction profile. The sensed acceleration includes only the contributions to vehicle acceleration from thrust and aerodynamic forces. Gravity forces are not included. The secondary mode (the

$Q\alpha$ limiting mode) is only activated when the vehicle experiences large aerodynamic loads. These loads are constantly monitored by comparing the predicted angle of attack, α_{pred}, to an angle of attack limit defined by the division of the $Q\alpha$ limit by the estimated dynamic pressure, $\hat{Q}$:

$$\alpha_{pred} = \hat{\alpha} + e_A \tag{3.6}$$

$$\alpha_{lim} = \frac{|Q\alpha|_{lim}}{\hat{Q}} \tag{3.7}$$

where:

$\hat{\alpha}$ = estimated angle of attack

e_A = acceleration-direction error

If the predicted angle of attack is greater than the angle of attack limit, then the control system will switch to the secondary mode and thus null out any difference between the two signals. Using this dual-mode concept, acceleration-direction trajectory following is unimpaired by an add-on load relief function and the vehicle autopilot will only perform load relief, in the form of $Q\alpha$-limiting, when needed.

The option for either closed-loop or open-loop guidance is shown on the block diagram in Figure 3.4. For closed-loop guidance, a new acceleration direction profile can be provided by trajectory design in flight and a new $Q\alpha$-limit can be used for the angle of attack limit calculation. This closed-loop guidance concept will be discussed further in section 3.6.

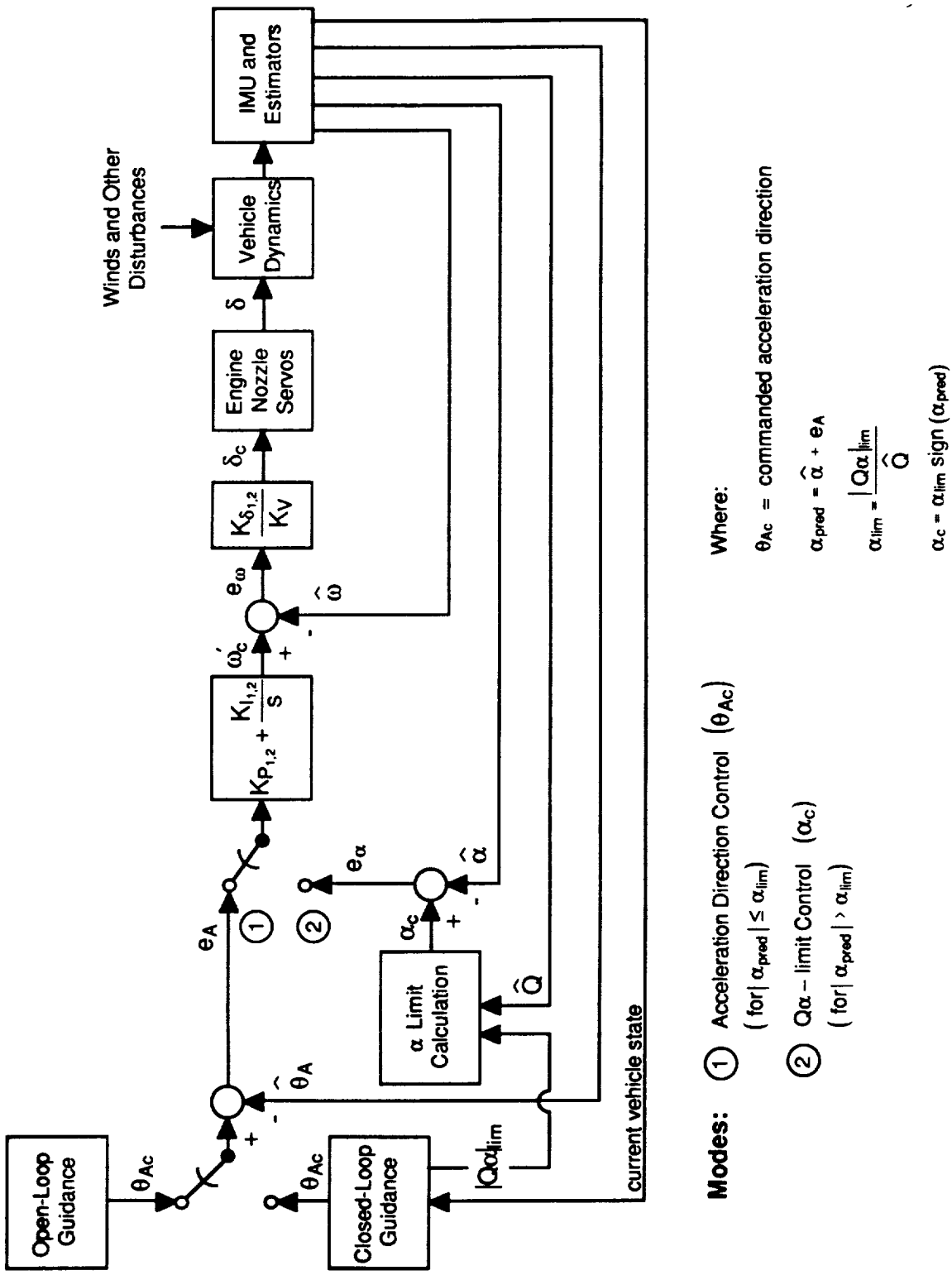

Figure 3.4: Phase 3 Guidance and Control Block Diagram

The control system shown to the right of the mode switch in Figure 3.4 is similar in form to that used for Phase 1 and 2. The switch provides either an acceleration direction error signal, e_A, or an angle of attack error, e_α, to the control system. The error signal used will be modified by proportional-integral control producing a commanded pitch attitude rate, ω_c'. This signal is compared to the estimated pitch rate, ω. The resulting error in pitch rate, e_ω, is multiplied by a time-varying proportional gain, K_δ/K_V, to provide an engine nozzle deflection command, δ_c, to the engine nozzle servos. Again, the nozzle servos are idealized such that the commanded nozzle deflection is perfectly achieved.

Because the two control modes have different dynamic characteristics, different sets of control gains must be used. The alternative sets of gains are designated by the two different subscripts in the gains $K_{P_{1,2}}$, $K_{I_{1,2}}$, and $K_{\delta_{1,2}}$ shown in Figure 3.4. Boelitz, using a linear approximations for the system, showed how the two modes involved different dynamics and did a stability analysis for each. He also reset the integrator error so that the nozzle command would be continuous when switching between modes.

3.4 Sensing and Estimation

3.4.1 Sensed Signals

It is assumed for this thesis that the Inertial Measurement Unit (IMU) contains an attitude measuring device that measures vehicle attitude with respect to an inertial reference frame. The measured attitude is defined by a set of Euler angles. In addition, the IMU contains an integrating accelerometer that measures "sensed" inertial velocity. This velocity is the integral of sensed acceleration- i.e. acceleration produced by thrust and aerodynamic forces and excluding gravity. The IMU signals are processed to yield the following signals required for guidance and control:

1) Vehicle pitch attitude relative to a local earth horizontal: θ
2) Inertial velocity increments: ΔV

3) Inertial velocity: V

- this signal is the sum of the sensed inertial velocity and the integral of gravity, where gravity is specified by a gravity model

4) Inertial position: R

- the integral of inertial velocity

In addition to these four processed signals, the nozzle deflection, δ, is determined from nozzle actuator measurements.

There are several signals needed for the guidance and the control of the vehicle that cannot be measured directly during flight. These are the pitch angular rate (ω), the angle of attack with respect to the air-relative velocity (α), the dynamic pressure (Q), and the acceleration direction of the vehicle excluding gravity (θ_A). All of these signals must be estimated during flight.

3.4.2 Angular Rate

The pitch angular rate estimate, $\hat{\omega}$, is used as the inner loop feedback variable during flight phases 1, 2, and 3. It is also used for the estimation of angle of attack, $\hat{\alpha}$ to account for the effects of tangential and centripetal acceleration at the IMU. Because there can be significant quantization and intrinsic noise in the IMU attitude measurement, it is not sufficient to use a derived rate signal based only on the quotient of pitch attitude change and the sampling period. The noise in the attitude signal will be magnified in the derived attitude rate, especially if the sampling period is small.

Boeltiz used an angular rate estimator based on a first order digital complementary filter which has both derived rate (change in pitch attitude over a sampling interval) and estimated angular acceleration as inputs. A continuous-time representation is shown in Figure 3.5. Derived rate is the low frequency input and is passed through a low-pass filter to produce a rate estimate that is accurate at low frequencies. In the implementation of the high frequency path, an equivalent representation is used in which an estimate of angular acceleration is passed through a low-pass filter. This procedure gives the same results as

high-pass filtering a high frequency rate signal based upon integration of angular acceleration. The angular acceleration estimate is based upon the IMU-measured inertial velocity, the engine deflections, and corrections for any small errors in the modelling of the thrust and aerodynamic forces.

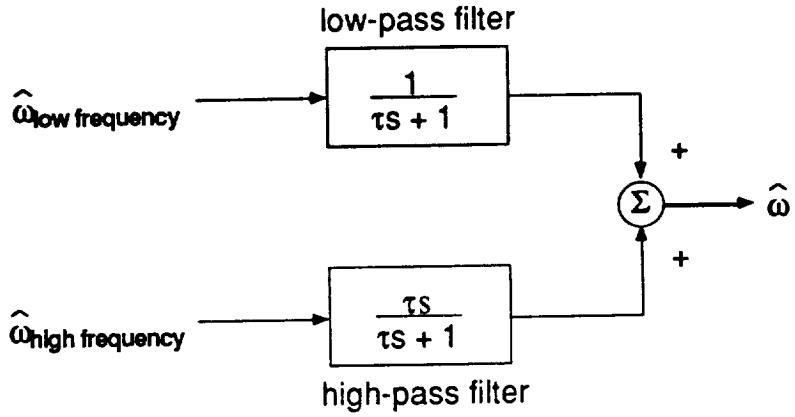

Figure 3.5: Continuous Signal Representation of Angular Rate Estimator

3.4.3 Angle of Attack

The angle of attack estimate, $\hat{\alpha}$, is employed in Phase 3. It is used in the mode switching logic and it is the primary outer-loop feedback variable in the control system of the $Q\alpha$ limiting mode. Boeltiz used a second order digital complementary filter for this estimator. The continuous-time representation of the filter is shown in Figure 3.6. The low frequency input, $\hat{\alpha}_{\text{low frequency}}$, is an angle of attack estimate determined from the following procedure:

1) Estimate the normal acceleration at the center of gravity from the IMU sensed velocity increments and estimated angular rate and angular acceleration.
2) Subtract the thrust contribution to the estimated normal acceleration to isolate the component produced by normal aerodynamic force.
3) Estimate the magnitude of the normal aerodynamic force by multiplying the estimated normal acceleration produced by this force with the vehicle mass.

4) Determine the normal aerodynamic force coefficient by dividing the estimated normal aerodynamic force by the product of the reference area and the estimated dynamic pressure.

5) Use the normal aerodynamic force coefficient and Mach number to search through the aerodynamic data tables to find a corresponding value of angle of attack.

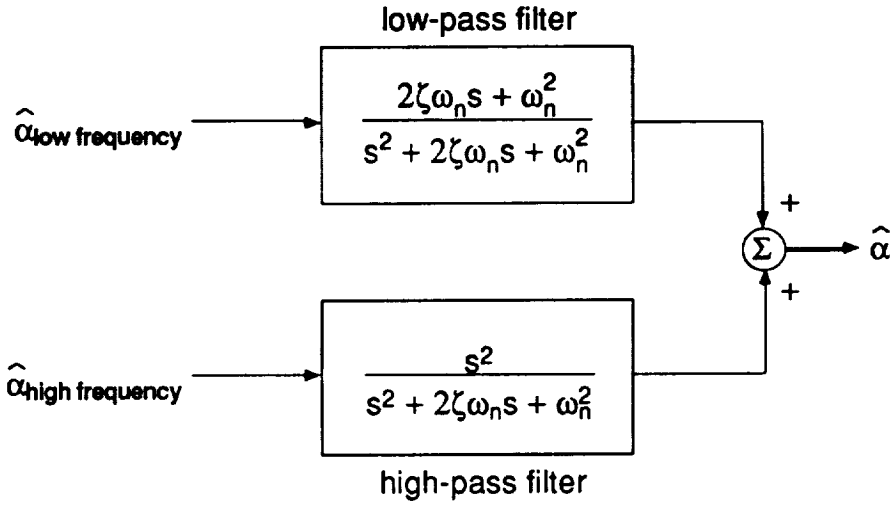

Figure 3.6: Continuous Signal Representation of Angle of Attack Estimator

The high frequency input to the complementary filter is based upon pitch attitude. Referring back to Figure 3.6, it can be seen that an *s* multiplying the high frequency input, $\hat{\alpha}_{high\ frequency}$, is equivalent to using $\dot{\hat{\alpha}}_{high\ frequency}$ as the high frequency input into a lower order filter. The equivalent filter is shown in Figure 3.7.

The problem now lies in estimating a discrete-time $\dot{\hat{\alpha}}_{high\ frequency}$. As shown in Chapter 2, the angle of attack can be expressed as:

$$\alpha = \theta - \gamma + \alpha_W \tag{3.8}$$

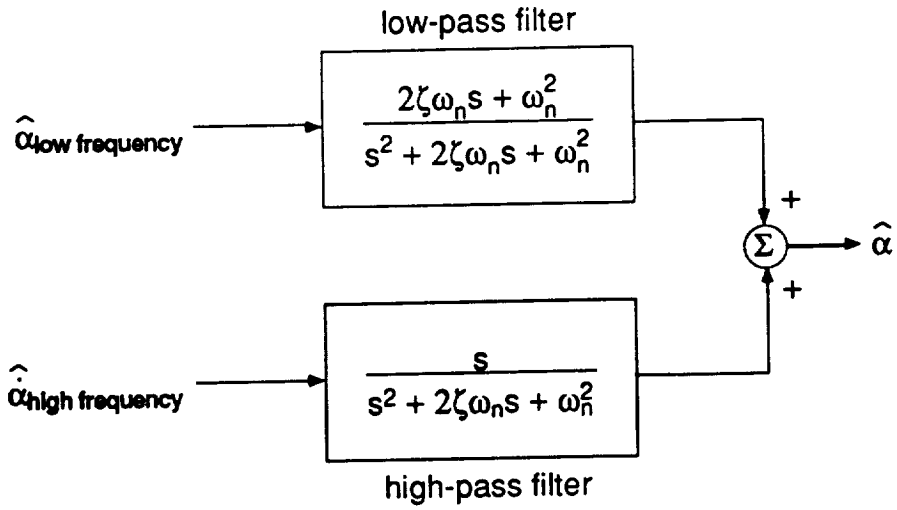

Figure 3.7: Alternate Representation of Angle of Attack Estimator

Taking the derivative of both sides yields:

$$\dot{\alpha} = \dot{\theta} - \dot{\gamma} + \dot{\alpha}_W \tag{3.9}$$

This equation can be expressed in the discrete-time domain as:

$$\Delta\alpha = \Delta\theta - \Delta\gamma + \Delta\alpha_W \tag{3.10}$$

The incremental change $\Delta\alpha_W$ is cause by variations in the winds normal to the velocity vector. Because these variations cannot be measured, this quantity is neglected in the angle of attack estimation. The quantity $\Delta\gamma$ is also neglected to yield the relationship:

$$\Delta\alpha = \Delta\theta \tag{3.11}$$

The omission of the incremental change in flight path angle can cause a small time-varying bias in the estimation of $\Delta\alpha$. A second order complementary filter is used for the angle of attack estimation so that this bias can be attenuated.

3.4.4 Dynamic Pressure

Phase 3 utilizes estimated dynamic pressure, $\hat{Q}$, in both the mode switching logic and in the $Q\alpha$ limiting mode. The dynamic pressure estimate is also used in the angle of attack estimator.

The dynamic pressure is a function of both atmospheric density and the magnitude of the air-relative velocity of the vehicle. The atmospheric density is assumed to be known during flight based upon a standard atmospheric model. However, because the vehicle has no wind sensors, the magnitude of the air-relative velocity must be estimated. Boelitz used the earth-relative velocity measurement from the IMU along with the estimated angle of attack and the assumption of horizontal winds to accomplish this task.

3.4.5 Acceleration Direction

The estimated acceleration direction, $\hat{\theta}_A$, is used as a feedback signal in the acceleration direction mode of Phase 3. The only measurements that are used to estimate this quantity are the inertial velocity increments processed from the IMU accelerometer measurements. Each control cycle, the inertial velocity increments are expressed in the body frame as:

ΔV_1 = increment in velocity along the vehicle x (roll) axis

ΔV_2 = increment in velocity along the vehicle y (pitch) axis.

ΔV_3 = increment in velocity along the vehicle z (yaw) axis.

The direction of the acceleration vector is then computed in terms of the pitch and yaw angles, β_p and β_y:

$$\beta_p = \tan^{-1}(-\Delta V_3/\Delta V_1) \tag{3.12}$$

$$\beta_y = \tan^{-1}(\Delta V_2/\Delta V_1) \tag{3.13}$$

The ΔV measurements are noisy signals because of IMU quantization. Therefore, the pitch and yaw acceleration angles are each sent through a low-pass filter with the following continuous-time form:

$$\frac{\tilde{\beta}(s)}{\beta(s)} = \frac{1}{\tau_\beta s + 1} \tag{3.14}$$

where τ_β is the filter time constant. The unit vector, $\hat{\mathbf{U}}_A$, representing the estimated filtered acceleration direction in body axes is calculated as:

$$\hat{U}_A = \text{Unit value of} \begin{bmatrix} 1 \\ \tan\left(\tilde{\beta}_y\right) \\ \tan\left(-\tilde{\beta}_p\right) \end{bmatrix} \tag{3.15}$$

The estimated acceleration direction angle in the pitch plane is then:

$$\hat{\theta}_A = \tan^{-1}\left(\frac{-\hat{U}_{A_3}}{\hat{U}_{A_1}}\right) \tag{3.16}$$

In the simulation of the acceleration direction control system, the error signal between the commanded acceleration direction, θ_{Ac}, and the estimated acceleration direction is determined by the following procedure. The cross product between $\mathbf{U}_{Ac}$ (the commanded acceleration direction unit vector) and $\hat{\mathbf{U}}_A$ is calculated:

$$\mathbf{C} = \hat{\mathbf{U}}_A \times \mathbf{U}_{Ac} \tag{3.17}$$

The angle, β_A, between the two vectors is:

$$\beta_A = \sin^{-1} |\mathbf{C}| \tag{3.18}$$

The vector composed of the error angles in roll, pitch, and yaw is then:

$$\hat{\mathbf{U}}_E = \beta_A [\text{ unit}(\mathbf{C})] \tag{3.19}$$

The pitch component of this vector is the error signal, e_A, shown in Figure 3.4.

3.5 Pre-Launch Trajectory Design

3.5.1 Introduction

A guidance system which is implemented in an open-loop manner in flight will utilize commands that were determined prior to launch by a trajectory design scheme. In the previous A.L.S. study, the guidance for phases 1 through 3 was open-loop. The guidance for Phase 4 was calculated closed-loop by a version of the Powered Explicit Guidance (PEG) program used in the current Space Shuttle system. This program neglects the effects of aerodynamic forces and can only be used after the vehicle has reached the upper atmosphere.

Suitable trajectories must meet the desired objectives while satisfying the specified constraints. For the A.L.S. vehicle, the primary objective of trajectory design is to reach orbit with as much fuel left as possible. The vehicle should have a high on-orbit mass, m_{final}. A large on-orbit mass will allow for any post-boost maneuvers that might be needed. Minimizing the fuel needed for endoatmospheric boost would also allow for heavier payloads to be carried into orbit. The primary constraint on the trajectory design is that the $Q\alpha$ product experienced during flight must be within the designer specified limit at all times.

The trajectory design process is greatly simplified if a trajectory shape or form is specified for each phase. The trajectory shapes for the first three phases are described by:

Phase 1: The altitude the vehicle must reach at the end of the vertical rise.

Phase 2: The sinusoidal function of pitch attitude rate versus time.

Phase 3: The three parameters of an angle of attack profile.

The remainder of this section is devoted to the explanation of the trajectory shapes and the pre-launch trajectory design concepts that Boelitz developed in his thesis. For the present study, the entire pre-launch trajectory design procedure has been automated using a

numerical optimization technique. The automation of the pre-launch trajectory design process is discussed in Section 3.6. Section 3.7 discusses how this same technique is applied to in-flight trajectory design.

3.5.2 Phase 1: Vertical Rise

The only parameter that can be varied for this phase is the altitude the vehicle is required to reach at the end of the vertical rise. Although this parameter has the possibility of affecting the rest of the trajectory, it was decided to hold this parameter constant at 400 feet.

3.5.3 Phase 2: Launch Maneuver

This phase is very important to the overall trajectory of the vehicle. It must be able to take the vehicle from the final state of Phase 1 to the initial state required for Phase 3. The launch maneuver must accomplish this quickly while the vehicle remains well below the $Q\alpha$ limit.

As discussed earlier in this chapter, the trajectory shape used for this phase is based on a sinusoidal function of pitch angular rate:

$$\omega_c = \Omega\left\{ 1 - \cos\left[\frac{2\pi}{T_{Kick}}\,(t - T_{Vert})\right]\right\}\Big|_{T_{Vert} \le t \le T_{Kick} + T_{Vert}} \tag{3.20}$$

where:

Ω = half the maximum commanded pitch rate

T_{Vert} = duration of Phase 1

T_{Kick} = duration of Phase 2

Integration of this equation yields:

$$\Omega = \frac{\theta_f - \theta_i}{T_{Kick}} \tag{3.21}$$

where:

θ_f = final pitch attitude of the vehicle at the end of the launch maneuver

θ_i = initial pitch attitude of the vehicle at the start of the launch maneuver = 90°

It should be noted that because phase 1 involves a vertical rise from the launch tower, θ_i will always be 90°. With this knowledge, the only two parameters that can be adjusted to change the shape of the pitch rate profile are θ_f and T_{Kick}.

A constraint on the choice of these parameters is that the angle of attack reached by the end of the launch maneuver, α_f, must match the angle of attack desired for the beginning of Phase 3. With this constraint in mind, Boelitz developed a procedure that automated the design of this phase of the trajectory. He chose θ_f and α_f as the two inputs to the procedure. The procedure used a reduced order/idealized control simulation to predict the vehicle state at the end of the launch maneuver. Using this simplified simulation of the vehicle's motion, he iterated on the value of T_{Kick} until the magnitude of the difference between the desired final angle of attack, α_f, and the predicted final angle of attack was less than a small tolerance. The golden section search in one dimension was used for this task.

3.5.4 Phase 3: Angle of Attack Profile

In Phase 3, the trajectory design process is based upon a simple angle of attack profile. As the trajectory design program simulates the vehicle following this angle of attack profile, the acceleration direction of the vehicle is calculated and stored away for use in the guidance loop during flight.

The shape of this angle of attack profile is shown in Figure 3.8. Figure 3.9 shows the angle of attack guidance and control system used for the trajectory design simulation of this phase. The error in angle of attack is sent into the same control system that was used for attitude control in phases 1 and 2. The angle of attack is first commanded to be a constant value, α_1. This value of angle of attack must be equal to the final angle of attack, α_f, achieved at the end of Phase 2. The angle of attack limit is continuously monitored by dividing a specified $Q\alpha$ limit by the current Q. When this limit becomes less than α_1, the

vehicle is commanded to fly along the limit. Because the specified $Q\alpha$ limit is a constant, the angle of attack limit is inversely proportional to the dynamic pressure. This results in a "bucket" shape for the angle of attack limit. The vehicle can move off of the limit once the limit becomes larger than a second constant angle of attack, α_2. There are therefore three parameters which define the shape of this trajectory: α_1, α_2, and the specified $Q\alpha$ limit. This profile is constrained in several ways:

1) The $Q\alpha$ limit used must be less than the designer specified $Q\alpha$ limit by a finite amount so that the normal loads on the vehicle will not be larger than structural limits.
2) Phase 2 must be able to meet α_1.
3) The need for α_2 to be compatible with Phase 4 requirements so that a "smooth" transition to Phase 4 can occur.

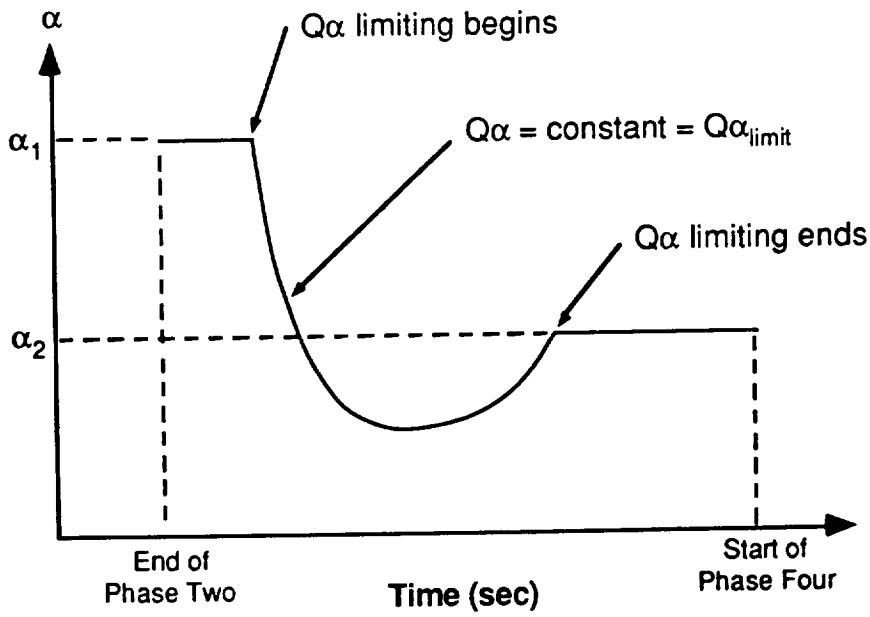

Figure 3.8: Phase 3 Angle of Attack Profile for Trajectory Design

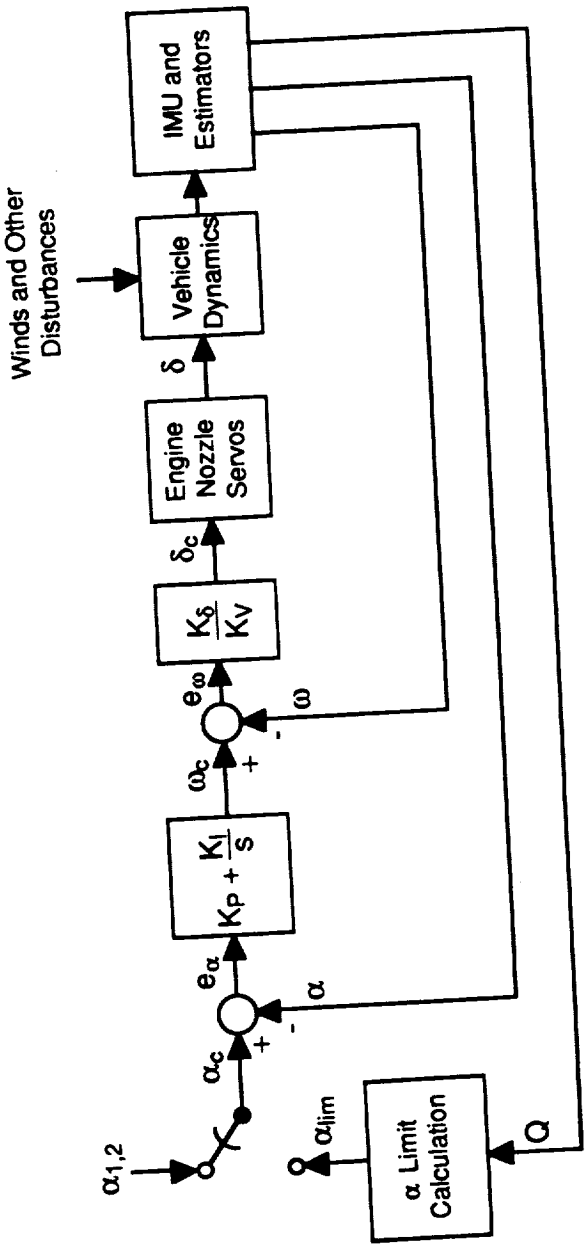

Figure 3.9: Phase 3 Control System For Trajectory Desgin

3.5.5 Phase 4: Powered Explicit Guidance

Phase 4 is initiated when the vehicle is in the upper atmosphere and aerodynamic forces are at a minimum. For this phase, a version of the Powered Explicit Guidance (PEG) program used on the Space Shuttle is used to guide the vehicle into the desired orbit. This guidance program is closed-loop in that it produces its own guidance commands in flight. It is not necessary to do any trajectory design prior to launch for this phase of flight. However, this program is very important to the overall trajectory design because it is used to predict the on-orbit mass of the vehicle. The primary objective of the overall trajectory design is to produce a high on-orbit mass.

The method updates the commanded acceleration direction angle in pitch every six seconds using a "linear tangent guidance law" of the form:

$$\tan \theta_A = K_0 + (t - t_0) K_1 \tag{3.22}$$

where θ_A is the commanded acceleration direction angle in the pitch plane and K_0, t_0, and K_1 are parameters which the program adjusts to minimize the propellant required to bring the vehicle into orbit, thus maximizing on-orbit mass.

This program treats the vehicle as a point mass so that rotational dynamics are neglected and the model is reduced from six degrees of freedom to three degrees of freedom. The only variable inputs to this program are the vehicle's inertial position, velocity, acceleration and acceleration of gravity vectors. The program is then used to predict the on-orbit mass of the vehicle.

3.6 Automation of Trajectory Design

The trajectory of the vehicle has been segmented into distinct phases with each phase defined in terms of a simple "shape". Using these shapes, the endoatmospheric boost portion of flight, phases 1 through 3, can be completely described with the following set of trajectory parameters:

1) θ_f = final pitch attitude of the vehicle at the end of Phase 2

2) α_1 = final angle of attack for phase 2 = initial angle of attack for Phase 3

3) α_2 = final angle of attack for Phase 3

4) $Q\alpha$ limit = specified $Q\alpha$ limit for mission < vehicle designer specified $Q\alpha$ limit

This is a very simple shape because only four parameters are needed to describe the trajectory. The problem is then how to choose these four parameters so that the on-orbit mass is maximized while the vehicle flies within all of the constraints considered in Section 3.5.

Boelitz tuned each of these parameters by trial and error using the full six degree of freedom simulation until it seemed that on-orbit mass had reached an maximum. This method is time-consuming and does not guarantee that an maximum has been reached.

In this thesis, a method has been developed which will "automatically" determine the set of trajectory parameters which maximize on-orbit mass. This method is based upon a numerical optimization scheme which uses on-orbit mass as the objective function it seeks to maximize. A predictive simulation is used to calculate the on-orbit mass. A simplified schematic of the automated trajectory design process is shown in Figure 3.10.

The predictive simulation is initialized with the current state of the vehicle. The only disturbance information available to the simulation is the pre-launch wind measurement. The optimization algorithm supplies the set of trajectory parameters. The predictive simulation will integrate the equations of motion from the current time to the time when PEG is used to predict on-orbit mass. The optimization algorithm will continue a multivariable search for the trajectory parameters which optimize on-orbit mass until a maximum on-orbit mass has been found.

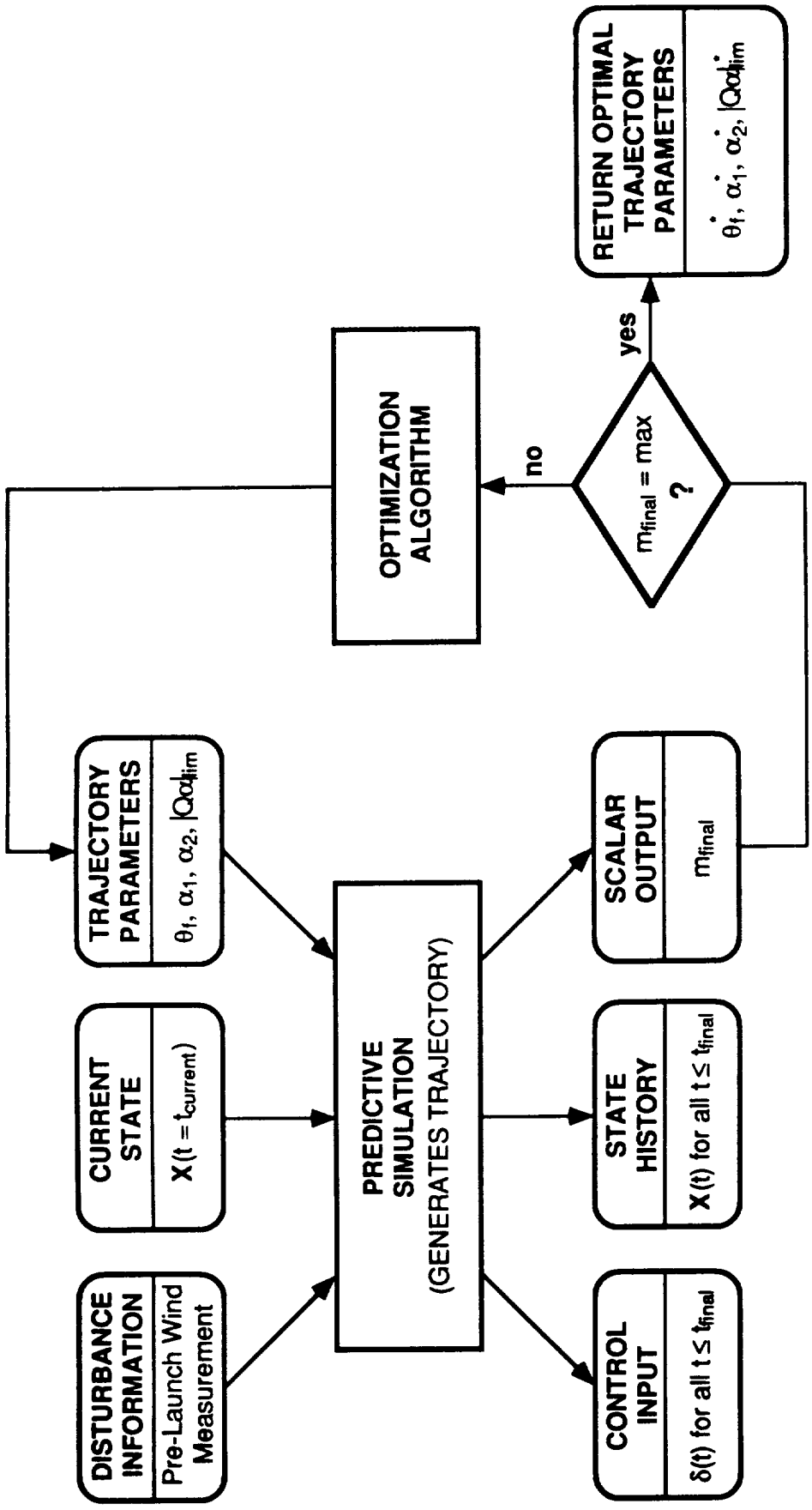

Figure 3.10: Automated Trajectory Design Process

This scheme is used before launch to reduce launch preparation time and to allow for unexpected changes in payload weight. However, because this scheme is "automatic" it can be used in flight to update the trajectory in the event of wind dispersions from the pre-launch measurement. The predictive simulation stores the complete state history so that a new acceleration direction profile can be used for guidance. In flight, there are no aerodynamic sensors so the disturbance information is assumed to be the same as it was prior to launch. However, if there are wind dispersions, these will affect the current state of the vehicle. This updated state information can then be used to determine a new set of flight parameters for the calculation of an updated acceleration direction profile.

The following two chapters describe the components of this scheme in detail. Chapter 4 discusses the predictive simulation. A reduced order/ idealized control simulation is used to speed computation by increasing the integration time step. Chapter 5 discusses the numerical optimization scheme chosen for this problem. A conjugate gradient method is used because the problem is highly nonlinear. The gradient is approximated with finite differencing.

Chapter Four

PREDICTIVE SIMULATION

4.1 Introduction

In Chapter 3, a procedure was described for selecting trajectory parameters to maximize on-orbit mass for specified values of the $Q\alpha$ limit. In order to automate this process, a numerical optimization scheme is employed for which the objective function is the on-orbit mass. The prediction of on-orbit mass is computationally expensive because the vehicle's equations of motion must be integrated from the given initial conditions to the desired end conditions. A simplified predictive simulation has been written which greatly reduces the amount of computation needed to calculate the on-orbit mass. This chapter describes the characteristics of this simulation and compares its performance with the full six degree of freedom simulation (which includes the control systems described in Chapter 3).

Section 4.2 justifies and details the reduced-order model used for the predictive simulation. In order to increase the integration time step of the simulation, an idealized control system was developed. This approximation is described in Section 4.3. Section 4.4 describes the program flow and presents results for various wind conditions. Remarks and conclusions are given in Section 4.5.

4.2 Reduced-Order Model

The vehicle's pitch dynamics can be reduced to only three degrees of freedom for this study since the vehicle motion is restricted to the trajectory pitch plane. By choosing the inertial y axis such that it is perpendicular to the trajectory plane, only one angle is needed to specify the orientation of the vehicle. In addition, only two translational variables are needed to describe the location of the vehicle center of gravity with respect to the origin of the inertial frame. For the predictive simulation, it is still necessary to calculate mass

properties, aerodynamic data, environmental conditions, and thrust in the same way as for the 6DOF simulation, but the coordinate frame kinematics and equations of motion of the vehicle are greatly simplified by choosing the inertial frame in this manner.

The two reference frames used in the predictive simulation are shown in Figure 4.1 and are defined as:

(1) Inertial Reference Frame: (**x**,**y**, **z**)

The equations of motion used in the predictive simulation are referred to this reference frame. The origin is fixed to the surface of the flat Earth at the launch site. The **z** axis points toward the center of the Earth and the **x** axis points downrange. The **y** axis completes the right-handed set.

(2) Body-Fixed Frame: ($\mathbf{x_B}$, $\mathbf{y_B}$, $\mathbf{z_B}$)

The origin of this frame is fixed to the vehicle's center of gravity and assumes no roll motion. The $\mathbf{x_B}$ axis is parallel to the centerline of the vehicle and points towards the nose cone. Because the vehicle is restricted to pitch rotation only, the $\mathbf{y_B}$ axis is in the same direction as the inertial **y** axis. The $\mathbf{z_B}$ axis completes the right-handed set.

The motion of the body-fixed frame with respect to the inertial frame is constrained to translation in the inertial **x**-**z** plane and rotation about the inertial **y** axis. The position vector, **R**, locates the origin of the body-fixed frame with respect to the inertial origin. The rotation of the inertial frame into the body frame is described by a single angle θ, the pitch attitude. The rotation matrix that transforms a vector from inertial to body coordinates is given by:

$$[C]_{\text{predictive sim}} = \begin{bmatrix} \cos\theta & 0 & -\sin\theta \\ 0 & 1 & 0 \\ \sin\theta & 0 & \cos\theta \end{bmatrix} \tag{4.1}$$

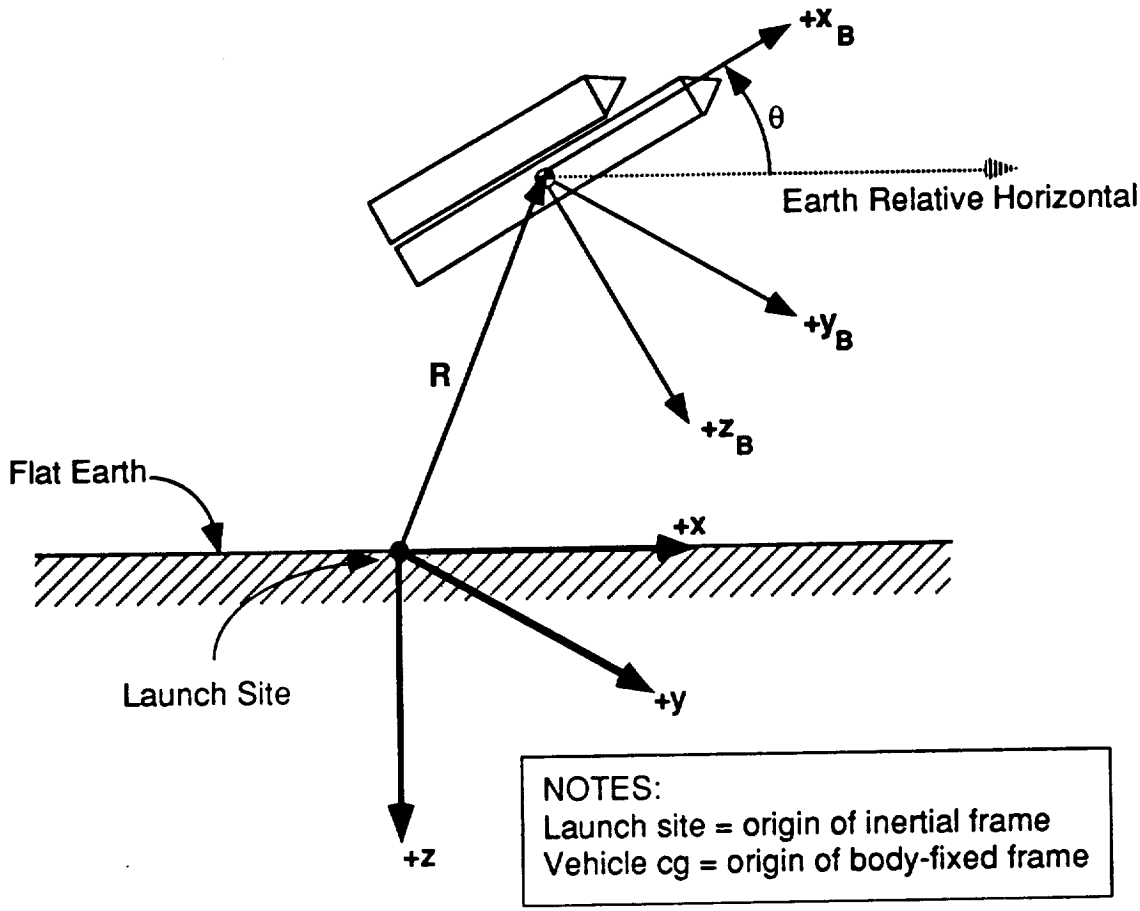

Figure 4.1: Predictive Simulation Coordinate Frames

The aerodynamic and thrust forces are defined the same way in the predictive simulation as they were in the full 6DOF simulation:

$$\mathbf{F_N} = - S\,Q\,C_N\,\mathbf{u_{ZB}} \tag{4.2}$$

$$\mathbf{F_A} = - S\,Q\,C_A\,\mathbf{u_{XB}} \tag{4.3}$$

$$\mathbf{T_b} = T_b \cos\delta\,\mathbf{u_{XB}} + T_b \sin\delta\,\mathbf{u_{ZB}} \tag{4.4}$$

$$\mathbf{T_c} = T_c \cos\delta\,\mathbf{u_{XB}} + T_c \sin\delta\,\mathbf{u_{ZB}} \tag{4.5}$$

The angle that the vehicle subtends around the Earth during boost is very small and so it is possible to approximate the Earth as being flat during boost. Using this approximation, the gravity vector will always point in the direction of the positive inertial z axis:

$$\mathbf{F_g} = m\, g\, \mathbf{u_Z} \tag{4.6}$$

The aerodynamic and thrust forces are resolved from the body-fixed frame into the inertial frame by using the inverse of the rotation matrix defined in equation 4.2. These forces are then summed with the gravity force in the inertial frame to give the net force acting on the vehicle in inertial coordinates:

$$\mathbf{F_{NET}} = \mathbf{F_N} + \mathbf{F_A} + \mathbf{T_b} + \mathbf{T_c} + \mathbf{F_g} \tag{4.7}$$

Since it is assumed that there are no out-plane-forces acting on the vehicle, the y-component of the net force is always equal to zero:

$$\mathbf{F_{NET}} = F_{NET_X}\, \mathbf{u_X} + (0)\, \mathbf{u_Y} + F_{NET_Z}\, \mathbf{u_Z} \tag{4.8}$$

The translational equations of motion have the same form as for the 6DOF simulation:

$$\frac{d\mathbf{R}}{dt} = \mathbf{V} \tag{4.9}$$

$$\frac{d\mathbf{V}}{dt} = \left(\frac{1}{m}\right) \mathbf{F}_{NET} \tag{4.10}$$

where $\mathbf{V}$ = inertial velocity = V_E

Because there are no out-of-plane forces, the y-component of both position and velocity is always equal to zero:

$$\mathbf{R} = R_X\, \mathbf{u_X} + (0)\, \mathbf{u_Y} + R_Z\, \mathbf{u_Z} \tag{4.11}$$

$$\mathbf{V} = V_X\, \mathbf{u_X} + (0)\, \mathbf{u_Y} + V_Z\, \mathbf{u_Z} \tag{4.12}$$

The total moment acting on the vehicle is the same as was derived in Chapter 2:

$$M = (T_b + T_c)\, x_{cg} \sin\delta - T_b\,(D + z_{cg}) \cos\delta - T_c\, z_{cg} \cos\delta + S\,Q\,C_N\,(l_{cpx} - x_{cg}) + S\,Q\,C_A\,(-l_{cpz} + z_{cg}) \tag{4.13}$$

The rate of pitch is then derived from:

$$\frac{d\,\omega_p}{dt} = I_{yy}^{-1}\, M \tag{4.14}$$

The pitch attitude, θ, is the only angle needed to specify the attitude of the vehicle and is defined by:

$$\frac{d\,\theta}{dt} = \omega_p \tag{4.15}$$

4.3 Idealized Control

Boelitz used the full 6DOF simulation for pre-launch trajectory design and tuned the flight parameters by trial and error. When the full 6DOF simulation was used for trajectory design, pitch attitude control was utilized for phases 1 and 2 and angle of attack control was used for phase 3. The pitch attitude controller and angle of attack controller (described in Chapter 3) were digitally implemented in the 6DOF simulation with a sampling time of 0.1 seconds.

A larger integration time step is desired for the predictive simulation so that it will have a faster computational speed than the 6DOF simulation. To achieve this goal, an idealized control system was developed for the predictive simulation that replaces both the pitch attitude and angle of attack control systems. The idealized system is designed to approximate the low frequency response of the actual control systems. The idealized control system has several benefits that significantly reduce computation time. The replacement of the control systems with idealized control allows a very large integration time step to be used for the simulation. Also, the computations required to determine the

actuator commands for the actual control systems are replaced by much simpler computations for the idealized system. Finally, since the 6DOF control system always commands either pitch attitude or angle of attack the use of idealized control allows pitch attitude to either be specified or calculated directly from angle of attack. Thus, the rotational equation of motion need not be integrated twice to solve for pitch attitude.

The predictive simulation is used for trajectory design purposes so it must mimic the control systems used by the full 6DOF simulation for trajectory design. For the full simulation, the trajectory design procedure uses pitch attitude control for phases 1 and 2. Angle of attack control is used for phase 3 trajectory design. If the control systems are idealized then the assumption is made that the commanded control variable will be perfectly achieved:

Phase 1:

$$\theta = \theta_c = 90^\circ \tag{4.16}$$

Phase 2:

$$\theta = \theta_c = \Omega\left\{ (t - T_{Vert}) - \frac{T_{Kick}}{2\pi} \sin\left[\frac{2\pi}{T_{Kick}} (t - T_{Vert})\right]\right\} + \theta_{C_{INIT}} \tag{4.17}$$

Phase 3:

$$\alpha = \alpha_c = \begin{Bmatrix} \alpha_1 \\ \alpha_{lim} \\ \alpha_2 \end{Bmatrix} \tag{4.18}$$

Using the idealized control assumption, at least one flight orientation parameter has been specified for each phase. However, both pitch attitude and angle of attack must be known at all times during flight. Pitch attitude is needed to specify the kinematics of the body frame with respect to the inertial frame and the angle of attack is needed to determine the aerodynamic coefficients and thus the forces acting on the vehicle.

Using the relationships between the flight orientation parameters shown in Figure 4.2, it is possible to calculate the angle of attack from the idealized pitch attitude and vice versa.

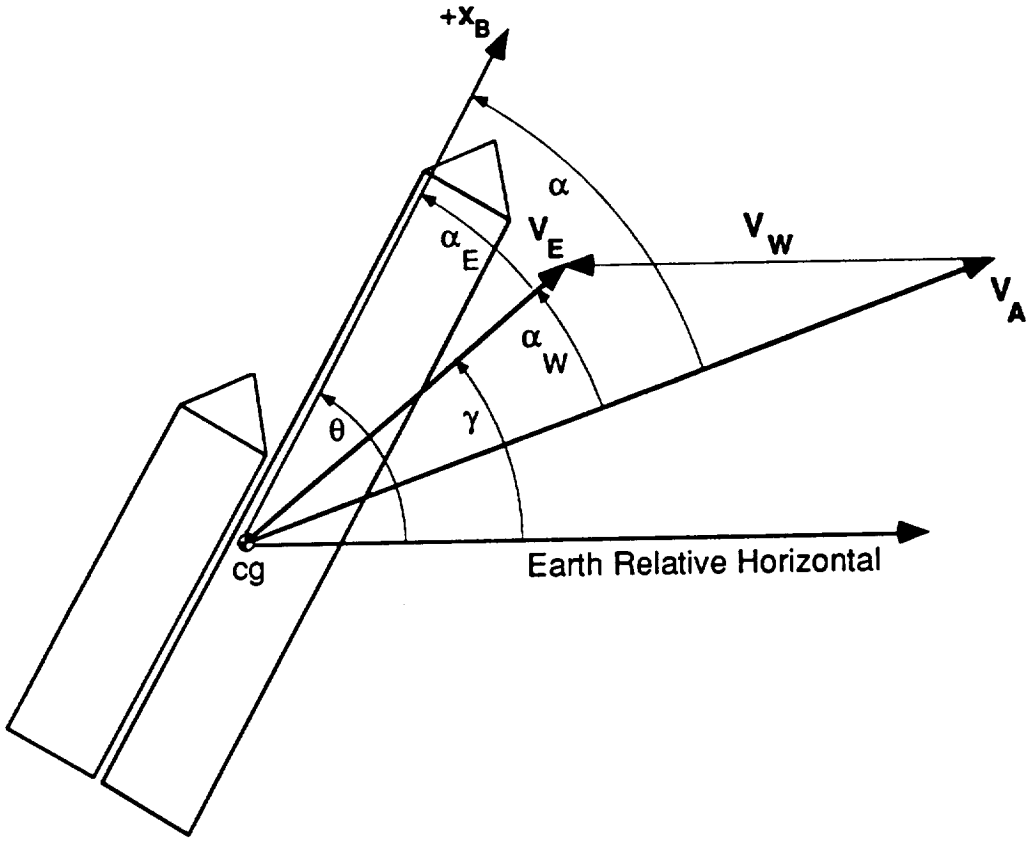

Figure 4.2: Flight Orientation Parameters

The following equation can be derived from Figure 4.2:

$$\theta = \alpha + \gamma - \alpha_W \tag{4.19}$$

where:

θ = earth-relative pitch attitude

α = angle of attack with respect to the air-relative velocity (V_A)

α_W = angle of attack contribution from winds = $\alpha - \alpha_E$

α_E = angle of attack with respect to the Earth-relative velocity

γ = flight path angle

Both the flight path angle, γ, and the angle of attack contribution from winds, α_W, can be determined from the assumed wind model and the translational equations of motion. Only one flight orientation parameter is specified by the idealized control assumption at a time, either pitch attitude or angle of attack. The unkown flight parameter can always be determined from equation 4.20 or equation 4.21:

$$\text{Phase 1 \& 2: } \theta = \theta_c \text{ therefore } \alpha = \theta - \gamma + \alpha_W \tag{4.20}$$

$$\text{Phase 3: } \alpha = \alpha_c \text{ therefore } \theta = \alpha + \gamma - \alpha_W \tag{4.21}$$

The 6DOF control systems of phases 1, 2, and 3 were used to determine the nozzle deflection, δ, necessary to rotate the vehicle to meet either the commanded attitude or angle of attack. With these control systems idealized, the question becomes how to deflect the engine nozzles to meet the assumptions given in equations 4.17 and 4.18.

It is possible to solve for the nozzle deflection angle from the pitch moment given by equation 4.14. This equation can be rewritten using the small angle approximation where $\sin(\delta) = \delta$ and $\cos(\delta) = 1$:

$$M = I\ddot{\theta} = (T_b + T_c)\, x_{cg}\delta - T_b\, D - (T_b + T_c)\, z_{cg} + SQC_N (l_{cpx} - x_{cg}) + SQC_A (-l_{cpz} + z_{cg}) \tag{4.22}$$

The above equation can now be solved for nozzle deflection:

$$\delta = \frac{T_b\, D + T\, z_{cg} - SQC_N (l_{cpx} - x_{cg}) - SQC_A (-l_{cpz} + z_{cg}) + I\ddot{\theta}}{T\, x_{cg}} \tag{4.23}$$

The pitch moment, $I\ddot{\theta}$, is the only term in the above equation that cannot be computed in flight from knowledge of the current vehicle state. The vehicle's pitch moment is known analytically for the first and second phases of flight using the idealized pitch attitude control assumption:

$$\textbf{Phase 1: } I\ddot{\theta} = I\ddot{\theta}_c = 0 \tag{4.24}$$

$$\textbf{Phase 2:}\quad I\ddot{\theta} = I\ddot{\theta}_c = \Omega\left(\frac{2\pi}{T_{Kick}}\right)\sin\left[\frac{2\pi}{T_{Kick}}\,(t - T_{Vert})\right] \tag{4.25}$$

The vehicle's pitch moment during the third phase has a very small average value because the pitchrate is only slowly varying after the launch maneuver. Therefore, for the purpose of determining nozzle deflection, it was decided to approximate the pitch moment of the vehicle as zero during phase 3:

$$\textbf{Phase 3:}\quad I\ddot{\theta} = 0 \tag{4.26}$$

4.4 Predictive Simulation Flow and Results

A flowchart of the predictive simulation is shown in Figure 4.3. The predictive simulation is initialized with the current vehicle state. The vehicle can be either on the launch pad or somewhere in flight. The wind information given to the predictive simulation will always be the wind profile measured prior to launch. The vehicle and environmental calculations are the same as those used in the 6DOF simulation. These computed variables include mass properties, atmospheric density and pressure, aerodynamic coefficients, winds, and kinematic transformations.

The guidance procedure commands pitch attitude during phases 1 and 2 and angle of attack during phase 3. The idealized control routine then assumes perfect control of one of the two flight parameters, attitude or angle of attack, and computes the unknown flight parameter. The pitch moment is specified (zero for phases 1 and 3, nonzero for phase 2) and is used to calculate the nozzle deflection needed to achieve perfect control. The net acceleration is then calculated in the inertial reference frame and the equations of motion are integrated using the fourth-order Runge-Kutta method. All of the vehicle, environmental, guidance and control calculations are updated in the middle of the time step. The simulation continues until the Powered Explicit Guidance (PEG) routine is called upon to predict the on-orbit mass, m_f, at 120 seconds. At this time, the aerodynamic forces are small in comparison to the thrust forces.

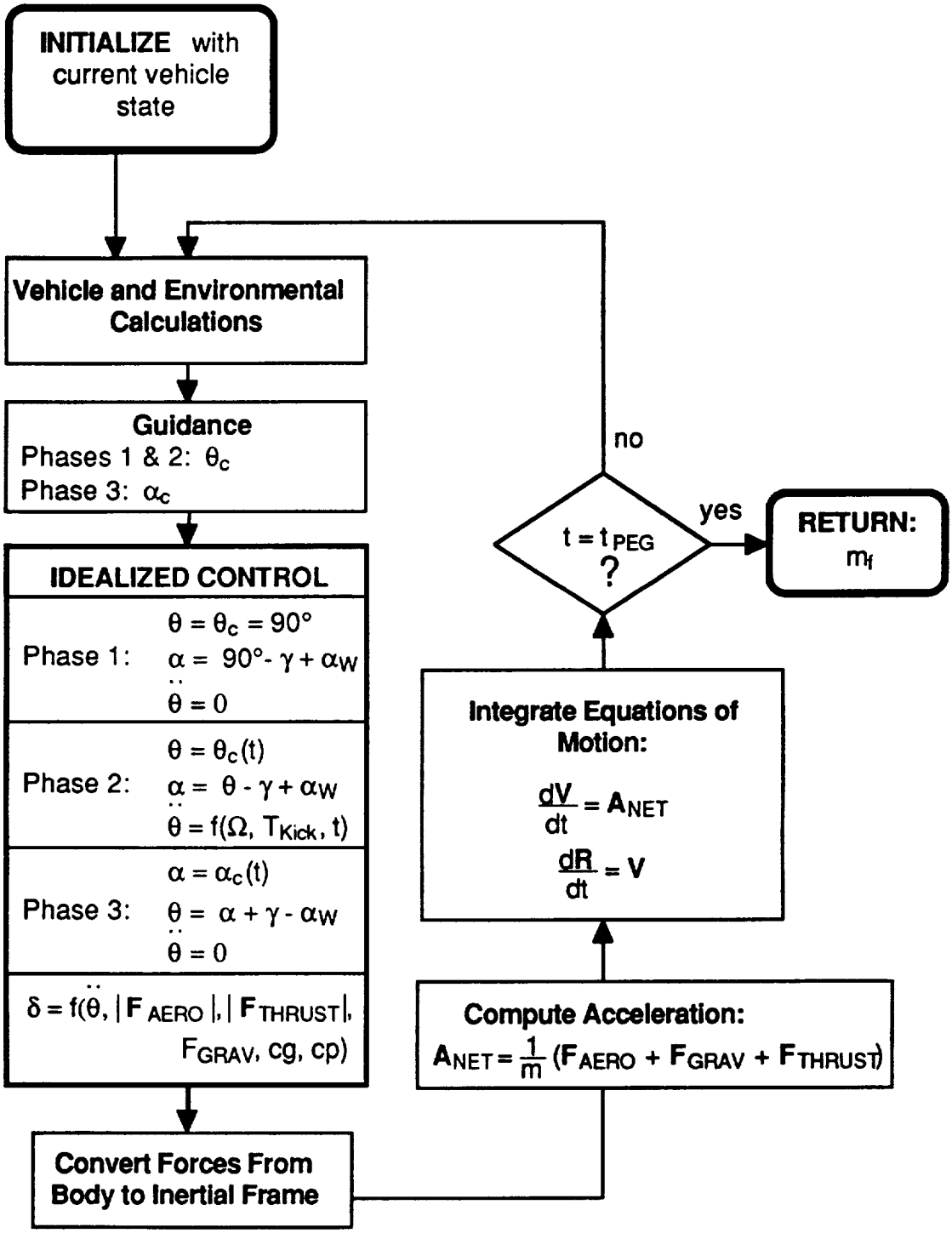

Figure 4.3: Predictive Simulation Flow Chart

To facilitate the comparison between the two simulations, it was decided to use an equatorial trajectory in the 6DOF simulation. This eliminated a complicated kinematic transformation of the predictive simulation's position, velocity, and acceleration into an inclined trajectory plane which would have been required for comparison of results. The relationship between the inertial reference frames of the 3DOF predictive simulation and the 6DOF simulation is shown in Figure 4.4. Because both frames are inertial, the transformation between the two frames is constant. The position, velocity, and acceleration vectors of the predictive simulation are expressed in the inertial coordinates of the 6DOF simulation at the transition to PEG.

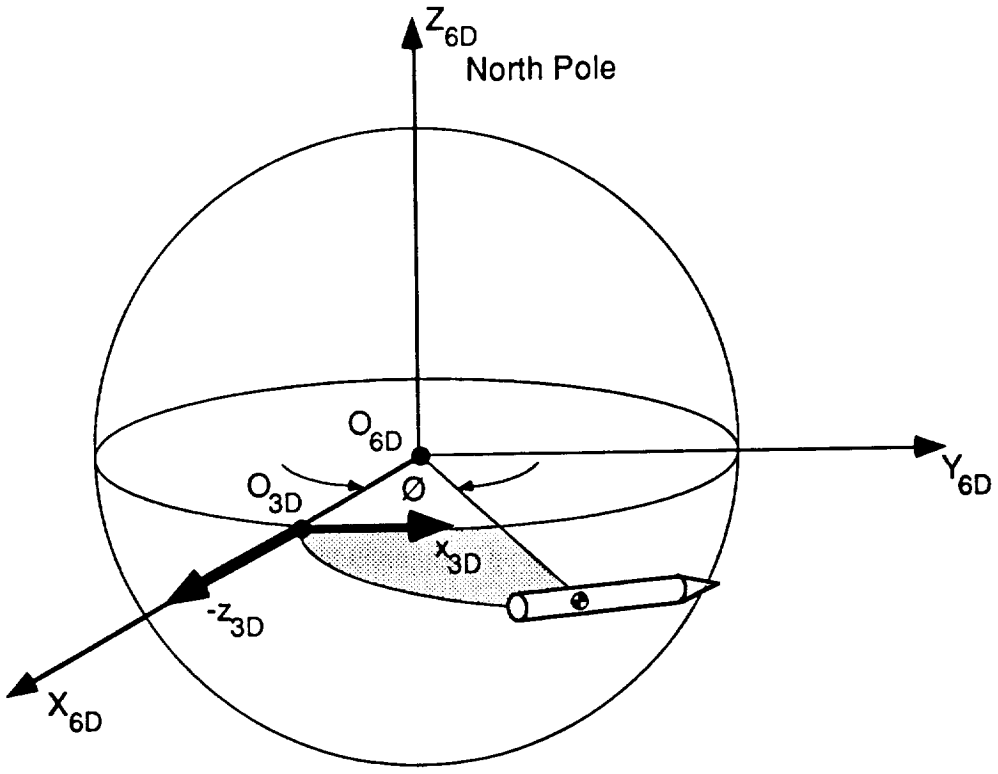

Figure 4.4: Relationship Between Inertial Reference Frames of Full (6DOF) and Predictive (3DOF) Simulations

The objective of the predictive simulation is to give an accurate prediction of the vehicle's flight while keeping computation to a minimum. To illustrate the performance of the predictive simulation, the following states were compared to those produced by the full 6 DOF simulation:

(1) angle of attack *(α)*

(2) flight path angle *(γ)*

(3) height *(H)*

(4) nozzle deflection angle *(δ)*

Two sets of comparisons were run. The first set corresponded to starting both the 6DOF simulation and the predictive 3DOF simulation at $t = 0$ (i.e. at launch) and running both until $t = 120$ seconds. This set will be referred to as the "entire" boost set because the predictive simulation flies the entire trajectory. The second set of comparisons was made by initializing the predictive simulation with the vehicle state given by the 6DOF simulation at $t = 60$ seconds. The predictive simulation then flew until $t = 120$ seconds. Thus, the predictive simulation flew only a "partial" boost trajectory. This test was done to demonstrate improvement in accuracy of the predictive simulation when it is initialized with the vehicle state at a later time in flight.

A study was made to select a value of integration time step for the predictive simulation. It was observed that the performance was greatly enhanced by using a small time step, *dt*, of 0.1 seconds for phases 1 and 2. This is due to the fact that the dynamics of the vehicle during the launch maneuver are much faster than during the rest of the flight. For phase 3, four different time steps were considered:

$$dt = \{0.1, 0.3, 0.5, 1.0\} \text{ seconds} \tag{4.27}$$

The first set of comparison runs corresponding to "entire" boost is shown in Figures 4.5 to 4.8. The entire state history is shown. For each plot, the solid line represents the state variable computed by the 6DOF simulation. The four dashed lines represent the state variable computed by the 3DOF simulation for the four different time steps given above.

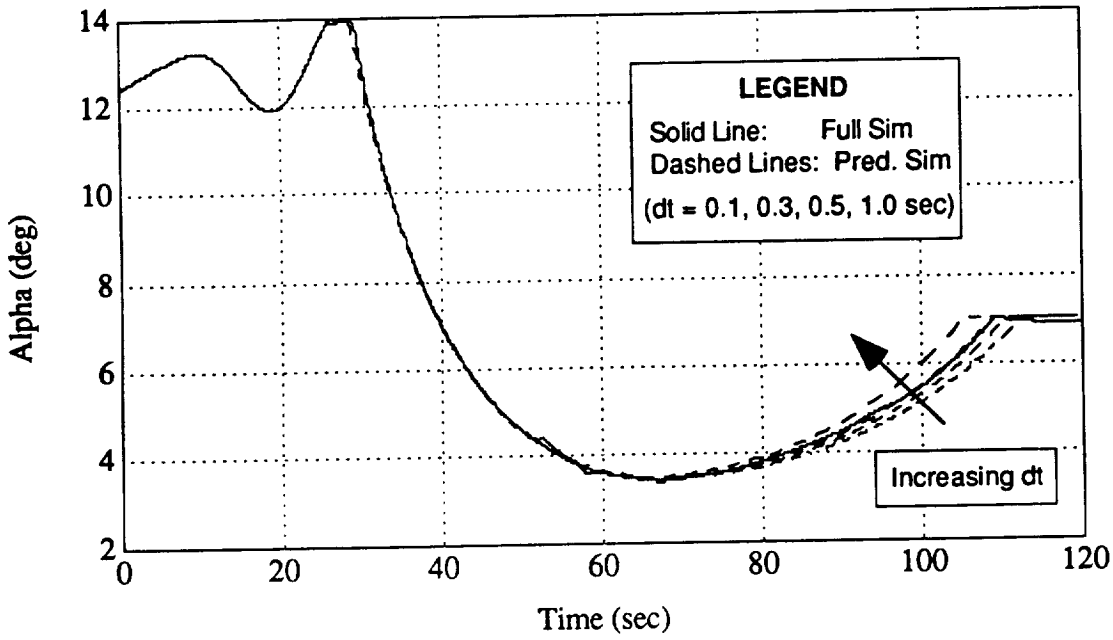

Figure 4.5: Angle of Attack Comparison Between Full and Predictive Simulations For Entire Boost

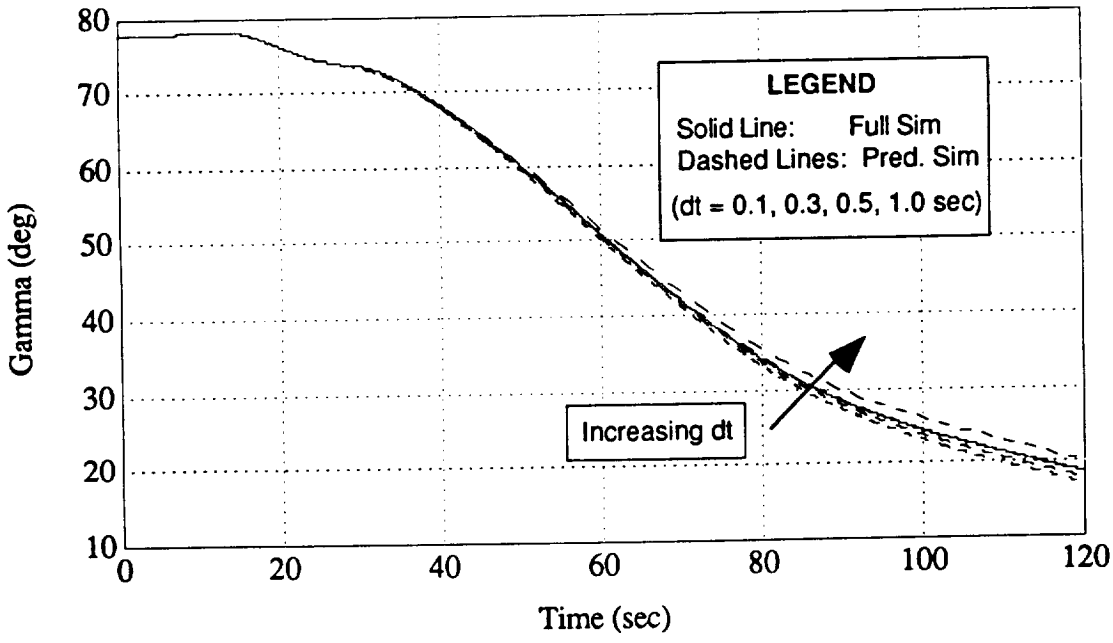

Figure 4.6: Flight Path Angle Comparison Between Full and Predictive Simulations For Entire Boost

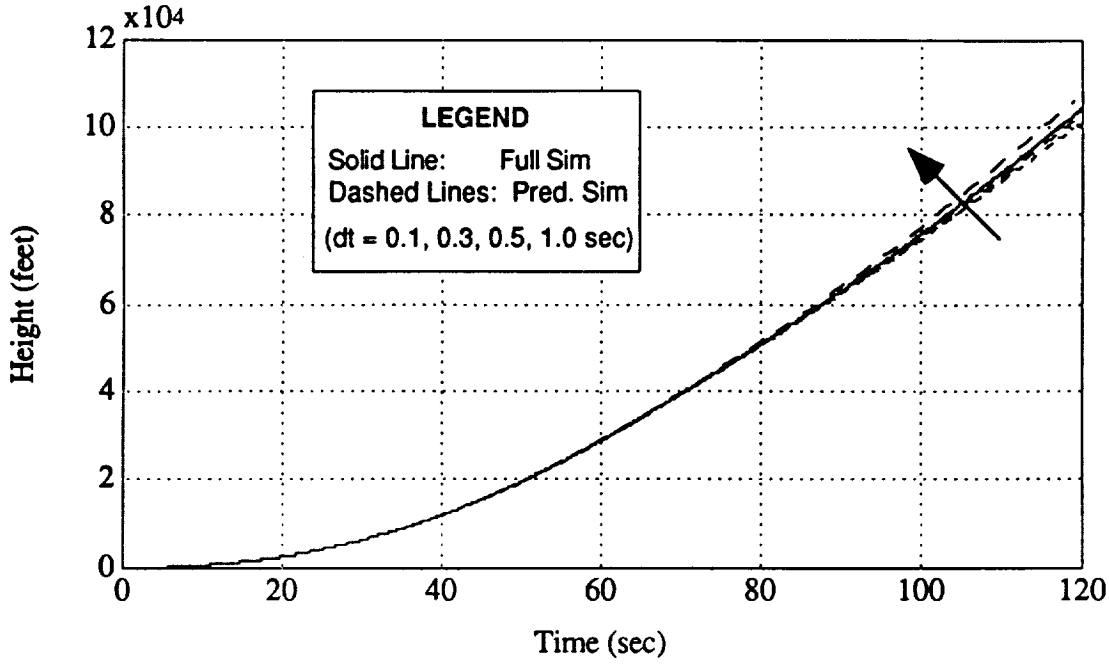

Figure 4.7: Height Comparison Between Full and Predictive Simulations For Entire Boost

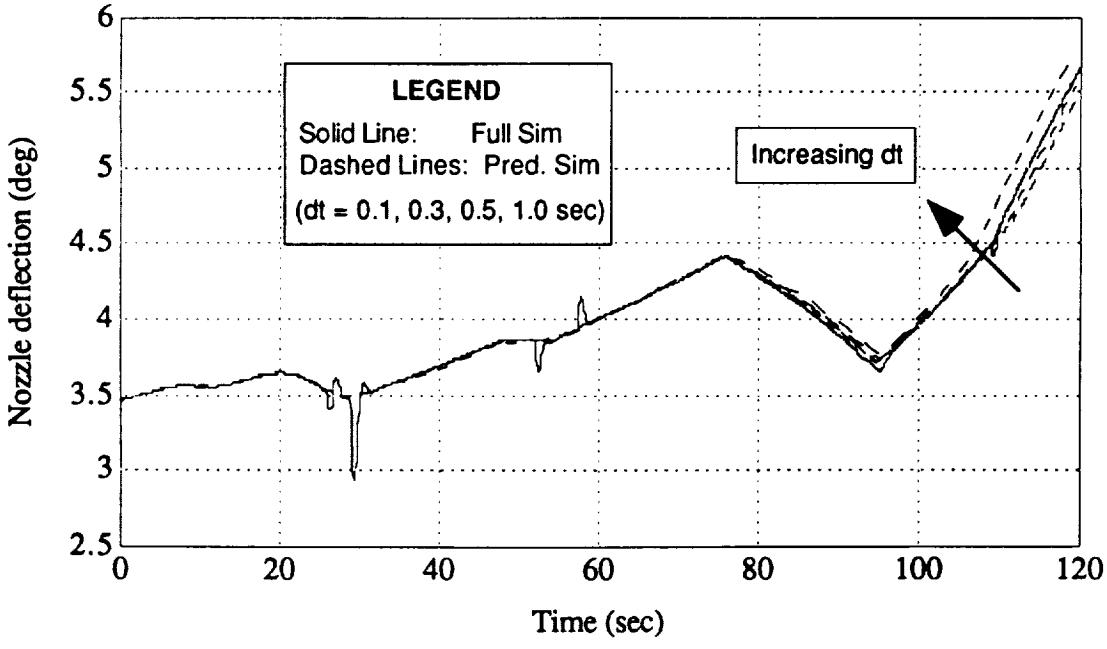

Figure 4.8: Nozzle Deflection Comparison Between Full and Predictive Simulations For Entire Boost

The arrow on the plots represents the direction of increasing integration time step for the predictive simulations.

Figure 4.5 shows the comparison in angle of attack between the simulations. The correspondence between the predictive simulation and the 6DOF simulation during phases 1 and 2 was very good. During phase 3, the 6DOF simulation utilizes proportional-integral control for angle of attack while the 3DOF utilizes idealized control. Even though the control is idealized for the predictive simulations, errors occur during the $Q\alpha$ limiting because the angle of attack limit is computed as the quotient of the $Q\alpha$ limit and Q. The dynamic pressure, Q, is a function of the air-relative velocity and this variable is calculated from the integration of the translational equations of motion. Increasing the time step of the predictive simulation causes integration errors to build in the air-relative velocity. The errors in air-relative velocity, through dynamic pressure, can thus enter into the calculation of the angle of attack limit. The predictive simulation will always steer perfectly to the angle of attack limit, but this limit may not be the same as for the 6DOF simulation because of the error in air-relative velocity.

It can also be seen in Figure 4.5 that the angle of attack given by the 6DOF simulation falls in between the angle of attack predicted by the 3DOF simulations for time steps of dt = 0.3 and 0.5 seconds. Thus, the angle of attack predicted by the 3DOF simulation with dt = 0.5 seconds is more accurate than the angle of attack predicted by the 3DOF simulation with dt = 0.1 seconds. This is a result of the fact that there are two main sources of error resulting from the use of the predictive 3DOF simulation. These error sources tend to produce angle of attack errors of opposite sign. The idealized control produces a negative error in angle of attack and the use of large time steps produces a positive error. For time steps between .3 and .5 seconds the errors tend to be offsetting.

Figures 4.6 and 4.7 illustrate the errors in flight path angle and height. The height for the 6DOF simulation also falls within the height curves generated by the 3DOF simulations. The errors between the 3DOF simulations and the 6DOF simulation build steadily with time because of integration errors in the equations of motion.

Figure 4.8 illustrates the error in engine nozzle deflection. The nozzle deflection shown includes the initial cant of 5°. The nozzle deflection of the 6DOF simulation has distinct spikes whereas the nozzle deflections of all of the 3DOF simulation runs are missing these spikes. The spikes in the 6DOF occur around the times when the wind profile has a discontinuity in slope. The vehicle must compensate for these discontinuities by rapidly pitching over. The pitch moment during these times is thus larger than normal. As a result, the zero pitch moment approximation used for phase 3 of the idealized control in the 3DOF simulation is not valid at these times. The average error of the nozzle deflection in the 3DOF simulations grows with time yet is still very small.

Table 4.1 shows the absolute errors in the final states of the predictive simulations at time = 120 seconds. The absolute error in predicted on-orbit mass is presented along with the percentage error of fuel left in the core on-orbit. This quantity is calculated as follows:

$$\%\, fuel_f \text{ error} = \frac{m_{f_{6DOF}} - m_{f_{3DOF}}}{fuel_{f_{6DOF}}} \tag{4.28}$$

where:

$fuel_{f,6DOF}$ = core fuel on-orbit for 6DOF sim = $m_{f,6DOF} - m_{DRY}$

m_{DRY} = dry mass of core

3DOF dt (sec)	α error (deg)	γ error (deg)	H error (feet)	δ error (deg)	m_f error (slugs)	$\%\, fuel_f$ error
0.1	0.61	1.55	2,850	0.16	7.0	5.0
0.3	0.25	0.83	1,390	0.07	2.8	2.0
0.5	0.06	0.15	20	0.01	6.9	4.9
1.0	0.60	1.43	3,260	0.17	15.3	10.9

Table 4.1: End State Error Comparison Between Full (6DOF) and Predictive (3DOF) Simulations After Entire Boost

The second set of comparison runs corresponding to "partial" boost is shown in Figures 4.9 to 4.12. As stated above, this set of runs was made by initializing the predictive simulation at the state given by the 6DOF simulation at time = 60 seconds. The accuracy of the predictive simulations is improved because the modeling and control errors have less time to grow. This improvement in accuracy is demonstrated in Figure 4.11 where the difference between simulations cannot even be observed over the time history of height. The absolute errors in end states for this set of runs and the on-orbit mass errors are shown in Table 4.2. The errors in the end states for the partial boost runs are significantly smaller than those that were produced in "entire" boost runs. Also, the percentage error of the core fuel left on-orbit is improved for most of the time steps.

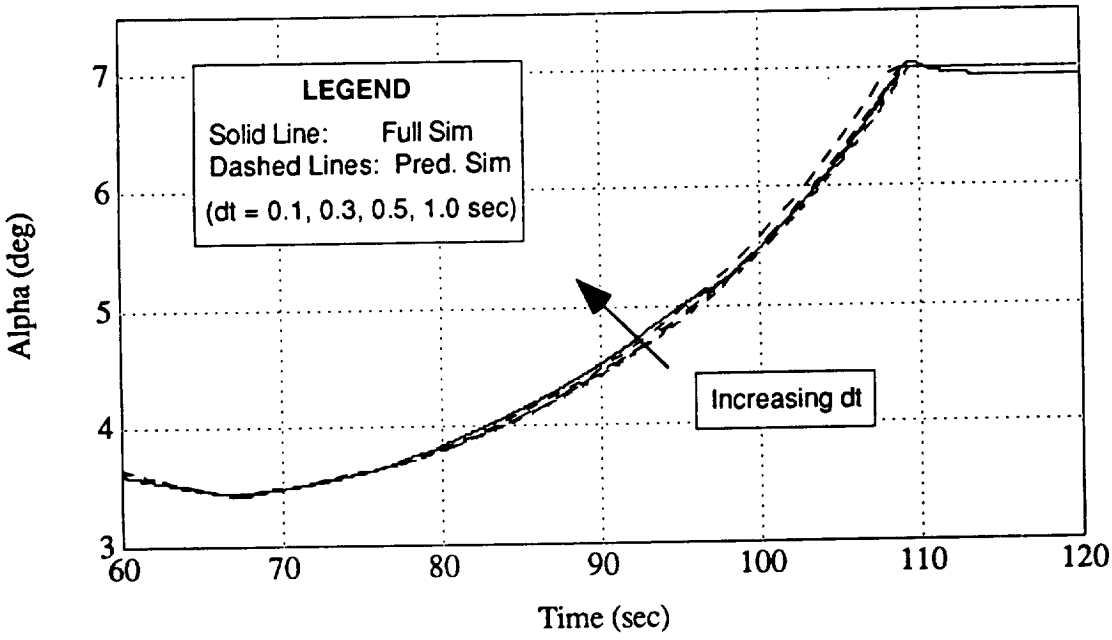

Figure 4.9: Angle of Attack Comparison Between Full and Predictive Simulations For Partial Boost

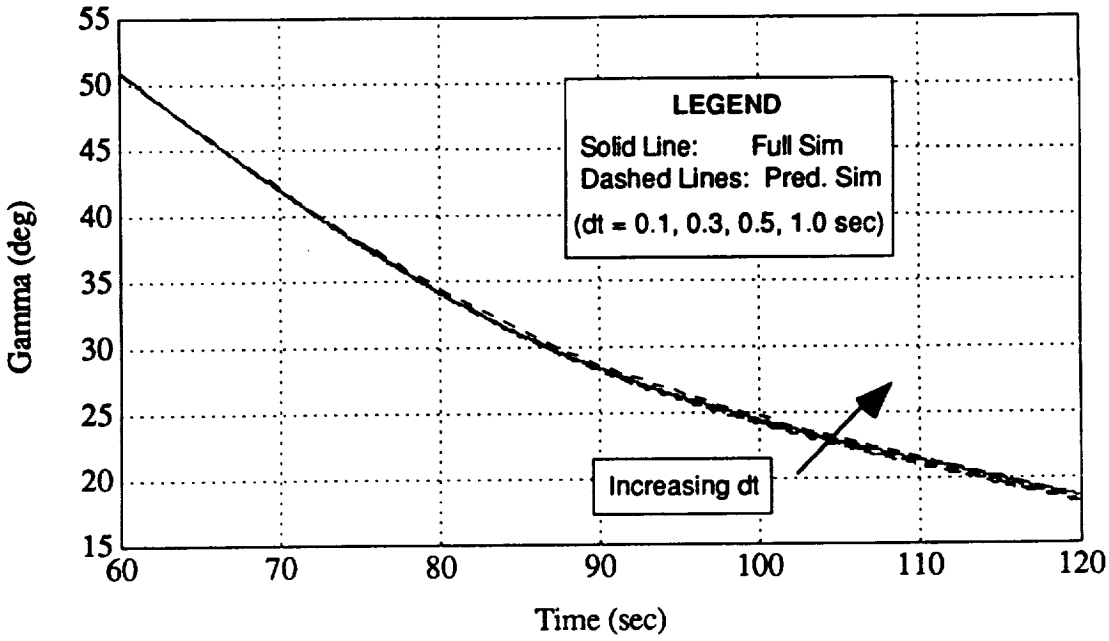

Figure 4.10: Flight Path Angle Comparison Between Full and Predictive Simulations For Partial Boost

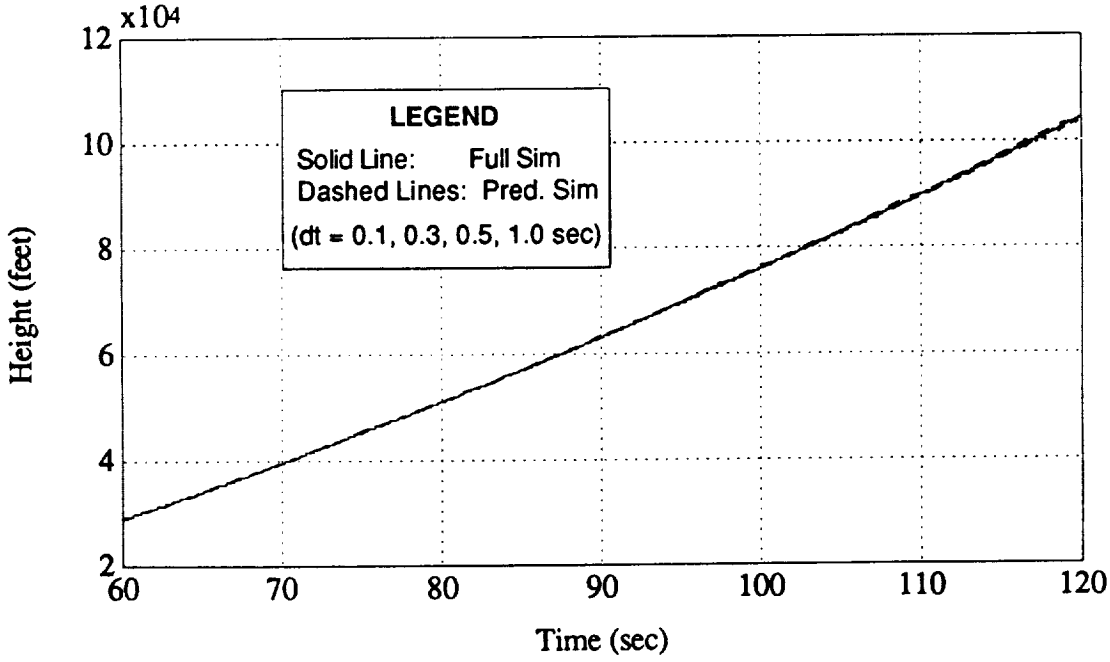

Figure 4.11: Height Comparison Between Full and Predictive Simulations For Partial Boost

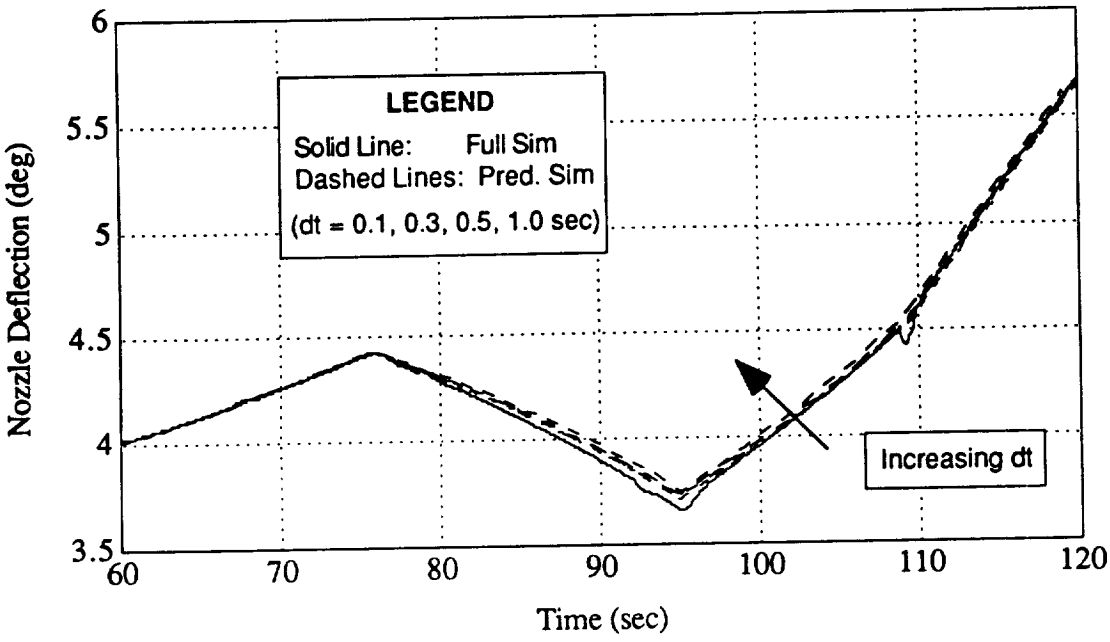

Figure 4.12: Nozzle Deflection Comparison Between Full and Predictive Simulations For Partial Boost

3DOF dt (sec)	α error (deg)	γ error (deg)	H error (feet)	δ error (deg)	m_f error (slugs)	% $fuel_f$ error
0.1	0.09	1.48	630	0.0277	3.1	2.2
0.3	0.03	0.38	240	0.0035	4.3	3.1
0.5	0.04	0.22	140	0.0002	5.4	3.9
1.0	0.17	1.11	460	0.0328	8.1	5.8

Table 4.2: End State Error Comparison Between Full (6DOF) and Predictive (3DOF) Simulations After Partial Boost

4.5 Conclusions

The predictive (3DOF) simulation developed for this thesis eliminates the kinematics and dynamics for the more complete simulation. The idealized control assumption also significantly reduces computation time and allows the use of a larger integration time step. These simplifications and assumptions greatly reduce the computational load of the predictive simulation. The accuracy of the predictive simulation has been shown to be very good in comparison to the 6DOF simulation.

Chapter Five

NUMERICAL OPTIMIZATION

5.1 Introduction

The primary objective of trajectory design for the A.L.S. is the maximization of on-orbit mass. An optimization procedure is described in this chapter which will maximize on-orbit mass. This mass is determined by the trajectory that is flown and is, therefore, a function of the particular parameters chosen to specify the trajectory shape. For a given set of trajectory parameters, the on-orbit mass is determined by using the predictive simulation described in the previous chapter. The simulation approach is required because it is not practical to develop a closed-form solution for the on-orbit mass. Consequently, the on-orbit mass function is not analytical. Any optimization procedure which seeks to maximize on-orbit mass must, therefore, be numerical in form. For the approach used in this thesis, the on-orbit mass function is multidimensional because as many as three parameters are used to define the trajectory shape.

This chapter first compares in Section 5.2 several multi-dimensional numerical optimization algorithms that are described in the current literature. The particular method chosen was a version of the conjugate gradient method. The overall procedure for implementing the conjugate method and some of the underlying theory is described in Section 5.3. Sections 5.4 and 5.5 describe separate subroutines that had to be performed in conjunction with the algorithm. Section 5.4 describes how the on-orbit mass function was optimized along a specific search direction. Section 5.5 describes how the gradient of the on-orbit mass function was approximated using finite differencing.

5.2 Comparison of Numerical Optimization Methods

There are many multi-dimensional numerical optimization algorithms that have been developed over the years. To determine the method most suitable for the optimization problem of this thesis, the current literature was studied. Two primary sources were used: Scales[3] and Press et. al.[4] .

All numerical optimization schemes rely on function information and sometimes derivative information. To understand these methods and the differences between them, it is important to provide some background information and notation relating to the definition of a multi-dimensional function and its derivative information. An objective function, $F(\mathbf{x})$, which a function of n independent variables must be defined. These variables form the column vector $\mathbf{x}$ of length n. All of the optimization methods studied were designed to minimize the objective function. The objective of A.L.S. trajectory design is the maximization of on-orbit mass. Since the maximization of on-orbit mass is equivalent to the minimization of the negative of on-orbit mass, the objective function will be defined as:

$$F(\mathbf{x}) = - m_f \tag{5.1}$$

where m_f is the on-orbit mass of the A.L.S. and is determined from the predictive simulation. There are three parameters that define the shape of the trajectory in the predictive simulation (θ_f, α_1, and α_2) and so the vector $\mathbf{x}$ is:

$$\mathbf{x} = [\theta_f \;\; \alpha_1 \;\; \alpha_2]^T \tag{5.2}$$

---

[3] Scales, L.E., Introduction to Non-Linear Optimization. 1985. London: MacMillan Education LTD., pp. 1-106.

[4] Press, W.H., Flannery, B.P., Teukolsky, S.A., Vetterling, W.T., Numerical Recipes. 1986. Cambrdige: Cambridge University Press., pp. 274-311.

The gradient vector of an objective function, **g**, is comprised of the n first partial derivatives of the objective function evaluated at **x**:

$$\mathbf{g} = \nabla F(\mathbf{x}) \tag{5.3}$$

and provides information on the shape of the function. For the objective function based upon on-orbit mass, this gradient is not available analytically and must be approximated with finite differencing. This procedure is discussed in Section 5.5.

Further information on the shape of a function is provided by a matrix composed of the n^2 second partial derivatives of $F(\mathbf{x})$ which is called the Hessian matrix:

$$\mathbf{G}(\mathbf{x}) = \nabla^2 F(\mathbf{x}) \tag{5.4}$$

and can be represented by the following tensor notation:

$$G_{ij} = \frac{\partial^2 F}{\partial x_i \partial x_j} \tag{5.5}$$

This matrix is also not analytical if on-orbit mass is used to define the objective function. To approximate this matrix with finite differencing would require a large number of function evaluations and would be computationally expensive.

The objective function is used in all numerical optimization schemes. The gradient vector and Hessian matrix can also be used in the optimization process because they provide information about the shape of the objective function. It was found that the current numerical optimization schemes can be divided into three main groups based upon the kind of function information they utilize.

The members of the first group are commonly called "direct search methods". These methods use only function evaluations. No information about the gradient vector or Hessian matrix is utilized. Without any knowledge of the shape of the function, these methods may take an excessively long time to converge to a minimum.

An improvement to the direct search methods is provided by a second group of algorithms that utilize first derivative information in addition to function evaluations. Specifically, they require knowledge of the gradient vector, g. Included in this category are the method of steepest descent, the conjugate gradient methods and variable metric methods. Using the derivative information, these algorithms are able to change the vector x in a direction that will tend to minimize the objective function. The first derivative information makes these methods more efficient than direct search methods because these methods tend to avoid examining any points that would increase function value. Direct search methods are useful for highly discontinuous functions where the gradient vector can be singular. However, for the trajectory problem in this thesis, the on-orbit mass is not a discontinuous function. For continuous functions, with continuous first derivatives, the gradient methods show faster convergence than direct search methods.

The third group requires information about the Hessian matrix of the objective function in addition to the gradient vector. Thus, more information about the shape of the function is utilized. This group includes Newton's method and variations of Newton's method. These methods show fast convergence for functions with a known Hessian matrix, but the cost in computer time of approximating a non-analytical Hessian matrix and the inaccuracies that could be introduced through such an approximation makes this method impractical for the optimization of on-orbit mass.

A member of the second group has been chosen for this study because it is possible to approximate the gradient of the on-orbit mass function using finite differencing. Of this group, the method of steepest descent was eliminated from consideration because its convergence is usually slower than the conjugate gradient method. The comparison between these two methods is presented in the following section. Both the conjugate gradient method and the variable metric methods require only gradient information. The variable metric methods construct a rough approximation to the Hessian matrix with gradient information collected over a successive number of iterations. Of these two methods, the conjugate gradient method was chosen over the variable metric methods for its simplicity.

5.3 Conjugate Gradient Method

Gradient methods, like other search methods, are all iterative: they begin with an initial guess of the vector **x** that will produce a minimum of the objective function, and iterate on **x** until the function is minimized to within some tolerance. The iteration on **x** is achieved by the following relationship:

$$\mathbf{x}_{k+1} = \mathbf{x}_k + \eta_k \mathbf{p}_k \tag{5.6}$$

where $\mathbf{x}_k$ is the previous estimate of the state which will minimize the objective function and $\mathbf{x}_{k+1}$ is the updated estimate. The vector $\mathbf{p}_k$ is defined as the "search vector", and η_k is a positive scalar weighting which is chosen to give the greatest decrease in the function $F(\mathbf{x})$, along the search vector. The quantity, η_k, is found by a separate one-dimensional optimization procedure described in Section 5.3.

In the method of steepest descent, the search vector is defined as:

$$\mathbf{p}_k = -\mathbf{g}_k \tag{5.7}$$

where $\mathbf{g}_k$ is the gradient vector. The steepest descent method is useful for a function where the gradient vector always points in the direction of the minimum. Such a function is shown in Figure 5.1 where the function contours are circular in the region around the minimum. In this case, the method of steepest descent would find the minimum in one iteration since all gradient vectors point toward the minimum. In general, this does not occur.

Using the steepest descent method, a new point, $\mathbf{x}_{k+1}$, is computed when an η_k is found which minimizes $F(\mathbf{x})$ along $\mathbf{p}_k$. The gradient at this point, $\nabla F(\mathbf{x}_{k+1})$, is then calculated and is orthogonal to $\mathbf{p}_k$. The new search vector, $\mathbf{p}_{k+1}$, will therefore also be orthogonal to the previous search vector, $\mathbf{p}_k$. If the function contours happen to be elliptical, as illustrated in Figure 5.2, then the method of steepest descent leads in a slowly converging zig-zag pattern to the minimum.

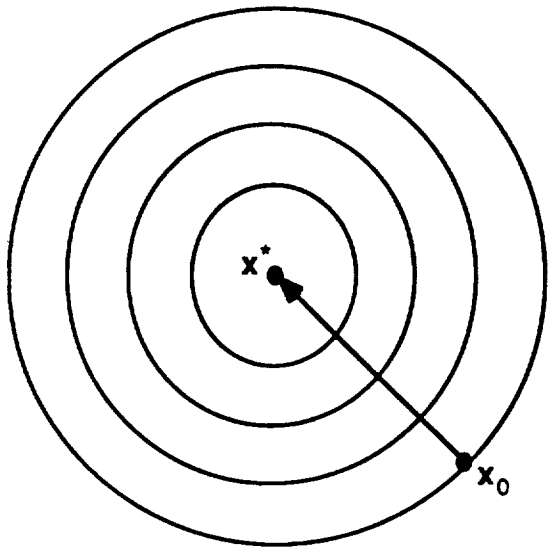

Figure 5.1 Steepest Descent Path for Circular Function Contours

The conjugate gradient method makes an improvement on the definition of the search vector direction and thus shows faster convergence than the method of steepest descent in most cases. To understand the properties of this method, it is useful to examine the case where the objective function to be minimized is a quadratic function of n independent variables:

$$F(\mathbf{x}) = \frac{1}{2}\mathbf{x}^T\mathbf{A}\mathbf{x} + \mathbf{b}^T\mathbf{x} + \mathbf{c} \tag{5.8}$$

where $\mathbf{A}$ is a constant symmetric n by n matrix, $\mathbf{b}$ is a constant n-vector and c is a scalar. The gradient of this function is:

$$\mathbf{g}(\mathbf{x}) = \mathbf{A}\mathbf{x} + \mathbf{b} \tag{5.9}$$

The Hessian matrix for the quadratic function is simply:

$$\mathbf{G}(\mathbf{x}) = \mathbf{A} = \text{a constant matrix} \tag{5.10}$$

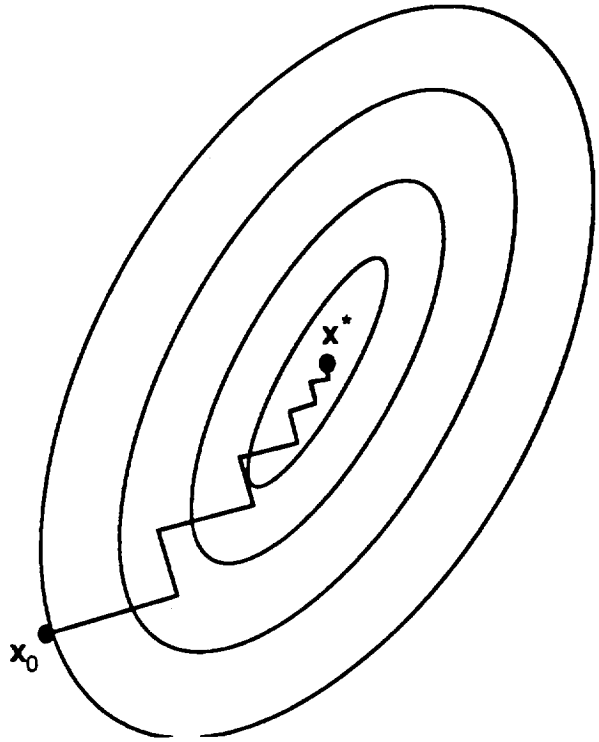

Figure 5.2 Steepest Descent Path for Elliptical Function Contours

If **A**, and thus **G**, is positive definite, then the quadratic function will be convex and have a global minimum with no local minima or saddle points. For the rest of the discussion, it is assumed that the quadratic function defined in equation 5.8 does have a positive definite **A** matrix.

A unique property of quadratic functions can be developed by taking the gradient at a point $\mathbf{x}_1$:

$$\mathbf{g}(\mathbf{x}_1) = \mathbf{A}\mathbf{x}_1 + \mathbf{b} \tag{5.11}$$

and again at a point $\mathbf{x}_2$:

$$\mathbf{g}(\mathbf{x}_2) = \mathbf{A}\mathbf{x}_2 + \mathbf{b} \tag{5.12}$$

Subtracting equation 5.11 from equation 5.10 yields:

$$\mathbf{g}(\mathbf{x}_1) - \mathbf{g}(\mathbf{x}_2) = \mathbf{A}\mathbf{x}_1 - \mathbf{A}\mathbf{x}_2 = \mathbf{A}\,(\mathbf{x}_1 - \mathbf{x}_2) \tag{5.13}$$

Substituting equation 5.10 into the above equation results in the following property which is unique to quadratic functions:

$$\mathbf{g}(\mathbf{x}_1) - \mathbf{g}(\mathbf{x}_2) = \mathbf{G}\,(\mathbf{x}_1 - \mathbf{x}_2) \tag{5.14}$$

Having defined the above property, it now possible to describe the conjugacy property of the conjugate gradient method for a quadratic function. The conjugate gradient method will minimize a quadratic function with a positive definite Hessian matrix in n iterations or less. This is accomplished by choosing the search directions used in equation 5.6 such that they are mutually conjugate to the Hessian matrix:

$$\mathbf{p}_j^T \mathbf{G}\mathbf{p}_k = 0 \quad \text{for } j \neq k \tag{5.15}$$

This conjugacy condition can be changed into a more physically meaningful form by first multiplying both sides of the equation by the scalar η_j:

$$\eta_j\, \mathbf{p}_j^T \mathbf{G}\mathbf{p}_k = 0 \tag{5.16}$$

Using equation 5.6, this is equivalent to:

$$(\mathbf{x}_{j+1} - \mathbf{x}_j)^T \mathbf{G}\mathbf{p}_k = 0 \tag{5.17}$$

Substituting the transpose of equation 5.13 results in:

$$(\mathbf{g}_{j+1} - \mathbf{g}_j)^T \mathbf{p}_k = 0 \tag{5.18}$$

The above equation means that the current search direction, $\mathbf{p}_k$, must be orthogonal to all of the changes in gradients, $(\mathbf{g}_{j+1} - \mathbf{g}_j)$ for $j = 0(1)k\text{-}1$, that were defined previously.

This property assures that the minimum of a quadratic function with a positive definite Hessian matrix will be found in at most n iterations. A proof of this is given in Scales.

Scales also derives the following definition of a search vector which satisfies the conjugacy condition:

$$\mathbf{p}_k = -\mathbf{g}_k + \beta_k \mathbf{p}_{k-1} \tag{5.19}$$

where the initial search vector is:

$$\mathbf{p}_0 = -\mathbf{g}_0 \tag{5.21}$$

There are several versions of the conjugate gradient method and they differ only in the definition of β_k. The particular version chosen for this thesis is the "Polak-Ribiere" method where β_k is given by the expression:

$$\beta_k = \frac{(\mathbf{g}_k - \mathbf{g}_{k-1})^T \mathbf{g}_k}{\mathbf{g}_{k-1}^T \mathbf{g}_{k-1}} \tag{5.20}$$

The Polak-Ribiere algorithm was recommended by both Scales and Press for its efficiency and stability in finding the minimum of a non-quadratic function.

It should be noted that the conjugate gradient method's definition of the search vector does not require any more function evaluations or gradient approximations than the steepest descent method. The previous gradient vectors are simply stored and used in the calculation of the new search vector.

The conjugate gradient method will only calculate search vectors that are mutually conjugate and will converge to a minimum in n iterations if the objective function is quadratic with a positive definite Hessian matrix. Most objective functions used in numerical optimization procedures, including the on-orbit mass function used in this thesis, are not quadratic functions with a known positive definite Hessian matrix. Saddle points and local minima could occur. Therefore, the gradient algorithm will generally go through

more than n iterations for convergence. If local minima are present in the objective function, then convergence to the local minimum is not guaranteed.

The algorithm flow is shown in Figure 5.3. The routine is supplied with an initial guess of the minimum, $\mathbf{x}_0$. The routine then computes the function and gradient, using the predictive simulation, at this initial point. The first conjugate gradient direction chosen is in the direction of the negative gradient because no previous gradient information is available. The routine then begins the main iteration loop. At the start of each iteration, a separate search algorithm (line minimization) finds the scalar, η_{k-1}, that minimizes $\nabla F(\mathbf{x}_{k-1})$ along the search vector direction, $\mathbf{p}_{k-1}$. Equation 5.6 is then used to update the estimate to $\mathbf{x}_k$. The method used for this search algorithm is described in section 5.3. The gradient is then calculated at this new point and the information is used to establish a new search direction, $\mathbf{p}_k$. A convergence check is made between the line minimization block and the gradient calculation block. The convergence is based on the difference of the function values between separate conjugate directions. If this difference is smaller than a specified tolerance, then the algorithm returns with the most recent estimate of the minimum.

5.4 Minimization Along Search Direction

The one-dimensional minimization of the objective function that must be carried out over η_k for each k-iteration may require many iterations. Recalling equation 5.6:

$$\mathbf{x}_{k+1} = \mathbf{x}_k + \eta_k \mathbf{p}_k \tag{5.22}$$

The scalar η_k must be chosen so that the value of the function at $\mathbf{x}_{k+1}$ is minimized along the search direction $\mathbf{p}_k$. This is accomplished as follows: the one-dimensional minimization algorithm computes a value for the scalar η_k and a separate routine takes this value and substitutes it into equation 5.22 along with the current estimate, $\mathbf{x}_k$, and search direction, $\mathbf{p}_k$. This defines a new estimate $\mathbf{x}_{k+1}$. The function of this new estimate is then evaluated and returned to the one-dimensional minimization algorithm.

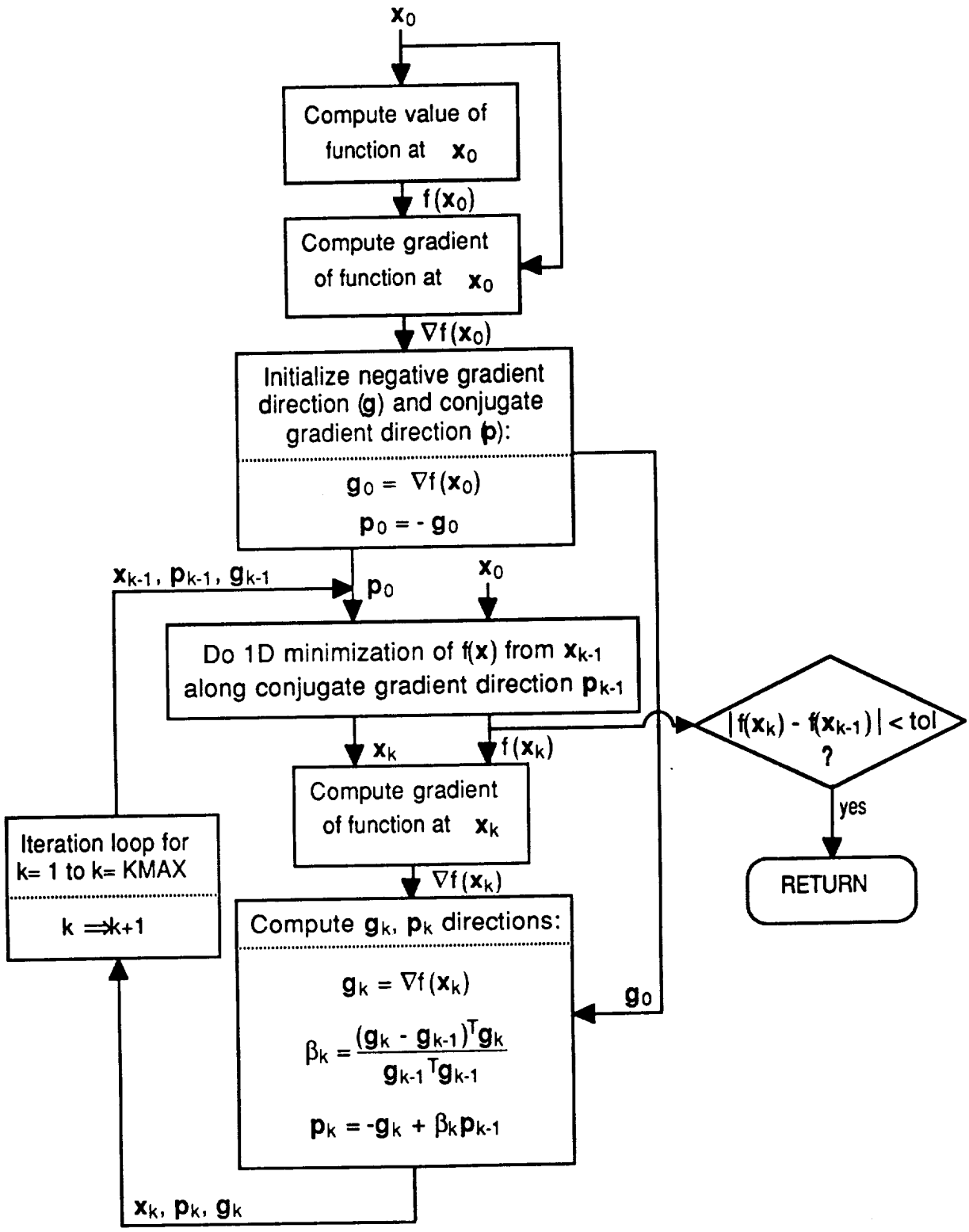

Figure 5.3 Polak-Ribiere Conjugate Gradient Algorithm for Function Minimization

The one-dimensional minimization algorithm used in this thesis was comprised of two separate programs that are described in Press. The first program brackets the minimum with the triplet of abscissas: A, B, and C such that:

$$A < B < C \tag{5.23}$$

and:

$$F(B) < F(A) \tag{5.24}$$

and:

$$F(B) < F(C) \tag{5.25}$$

Equations 5.24 and 5.25 state that, of the three points which bracket a function, B has the lowest function value. If the bracketing conditions shown above are achieved, then a minimum of the function must exist somewhere within the interval $[A, C]$.

Examples that illustrate whether or not a set of three points meet the bracketing condition are shown in Figures 5.4 and 5.5. In Figure 5.4, the first two bracketing conditions are met, but $F(B) < F(C)$ and so the minimum is not bracketed by the three points. Note that the minimum is in between B and C, but two points alone cannot satisfy the defined bracketing condition. In Figure 5.5, the full bracketing equation is met and the minimum is located within the interval $[A,C]$.

The method that this routine uses is based upon parabolic curve fitting. Two initial guess points for A and B are supplied to the routine. If $F(B) > F(A)$, then the values A and B are switched so that $F(B) < F(A)$. The routine then calculates a guess for C such that the relative distance between A and B compared to the distance between A and C is the golden section, G_r :

$$C = B + (2 - G_r)(B - A) \tag{5.26}$$

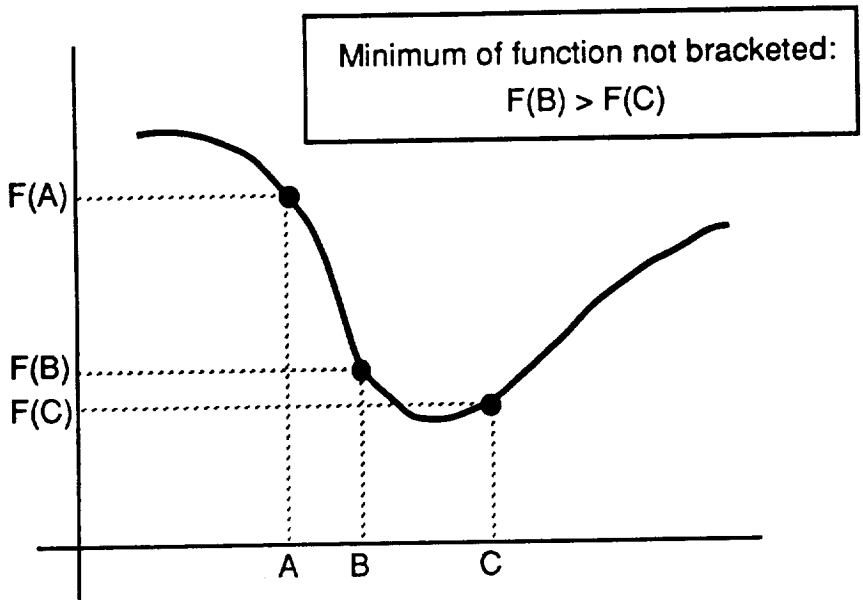

Figure 5.4 Bracketing Interval for Function Minimum not Bracketed by Triplet of Abscissas

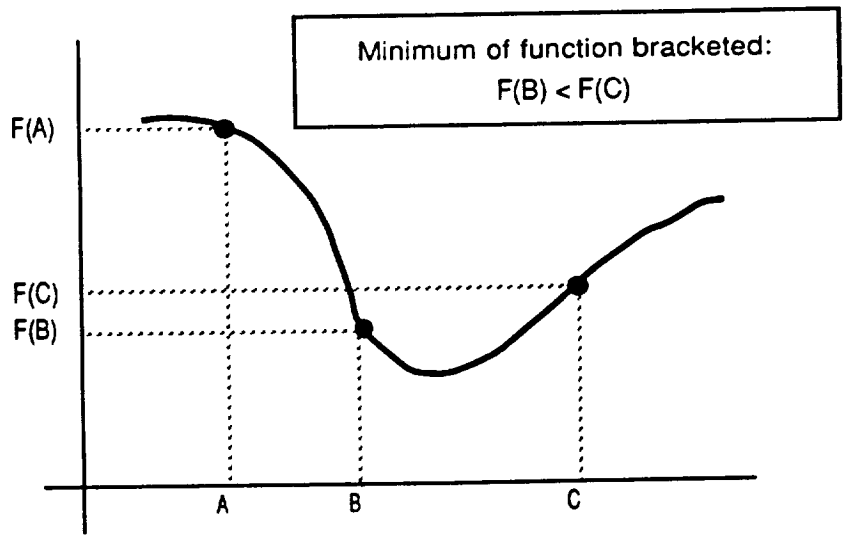

Figure 5.5 Bracketing Interval for Function Minimum Bracketed by Triplet of Abscissas

where:

$$G_r = \frac{3 - \sqrt{5}}{2} \tag{5.27}$$

After C is calculated, the routine does a parabolic curve fit between the three points. The routine solves for the minimum of this parabola and examines the function evaluated at this point.

Examples of this procedure are shown in Figures 5.6 and 5.7 where points A, B, and C do not bracket the function minimum. The abscissa of the parabolic minimum is U. In Figure 5.6, the curve fit results in U being located to the right of C. If the function to be minimized is F_1, then the function value at U is less than than the function value at C. The minimum is not bracketed in this case. If F_2 is the objective function, then the function value at U is greater than the function value at C. In this case, all of the bracketing conditions are met and the minimum is bracketed by B, C, and U.

Figure 5.7 shows what would happen if the parabolic minimum was located between B and C. If the function is defined by F_1, then the function value at U is less than the function value at C. The minimum is bracketed by B, U, and C. If the function is defined by F_2 then the value of the function at U is less than B but still greater at C. The minimum of F_2 is not bracketed.

If the function is not bracketed on the first iteration, then the procedure recalculates another U based on golden section magnification and does another parabolic curve fit with the three lowest points. The routine continues until the minimum has been bracketed.

At this point, the method for choosing the initial points to give this routine will be discussed. Press proposed using the points $A = 0$ and $B = 1$ as the initial test points. For the optimization of on-orbit mass, this initial guess for B was frequently unsuitable.

Minimum of parabolic fit, U, outside [A,B,C]:

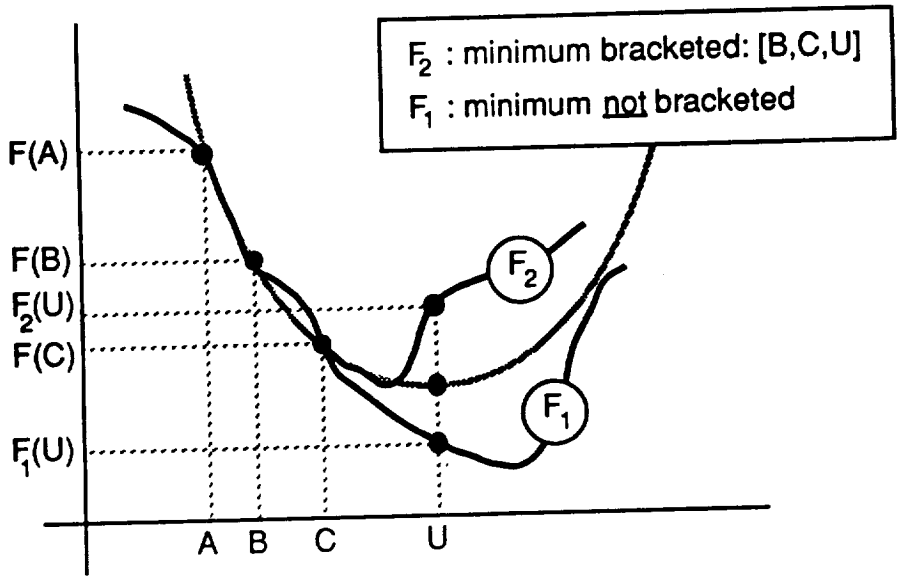

Figure 5.6 Parabolic Curve Fit - Minimum Outside Bracketing Interval

Minimum of parabolic fit, U, inside [A,B,C]:

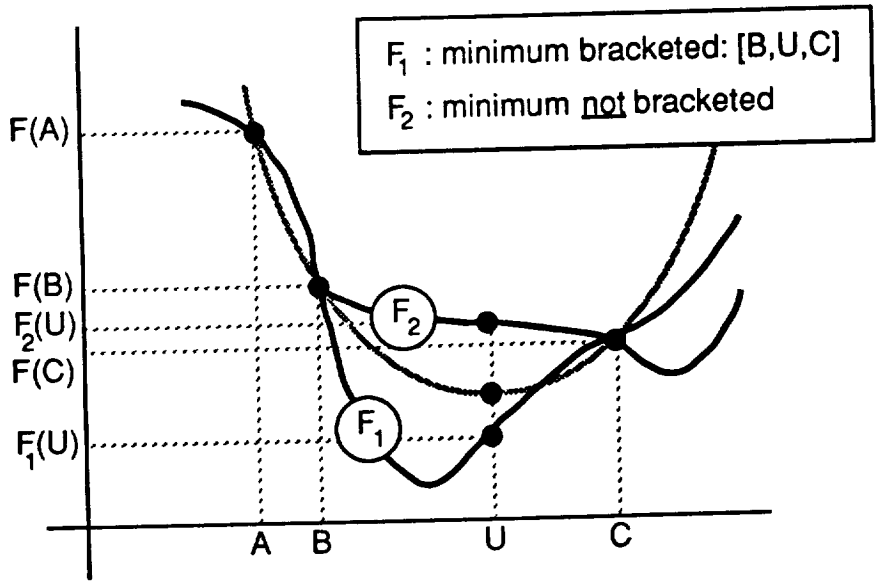

Figure 5.7 Parabolic Curve Fit - Minimum Inside Bracketing Interval

As stated previously, the purpose of the one-dimensional minimization procedure is to find the value of η_k which when multiplied by the search direction, $\mathbf{p}_k$, and added onto the current estimate of the minimum, $\mathbf{x}_k$, would minimize the value of the objective function along the search direction at the new estimate, $\mathbf{x}_{k+1}$. The point $A = 0$ poses no problem because it translates into a test point for η_k that will result in the current estimate, $\mathbf{x}_{k+1}$, being set to the previous estimate, $\mathbf{x}_k$. However, the point $B = 1$ corresponds to adding the entire search vector onto the current estimate. If the search vector is large, then the new estimate that would result from this addition could lie outside of the physical constraints of the trajectory. For example, the attitude at the end of launch maneuver cannot be larger than 90°.

To correct for this problem, the following procedure was developed to find a suitable initial guess for η_k. Suppose the constraints on the estimate $\mathbf{x}$ are specified such that each component of $\mathbf{x}$ has both an upper and a lower bound:

$$l_i < x_i < u_i \quad \text{for } i = 1{:}n \tag{5.28}$$

where:

l_i = lower bound on x_i

u_i = upper bound on x_i

A value of η_k is desired such that when it is used in equation 5.22, none of the components of the new estimate, $\mathbf{x}_{k+1}$, will violate the condition given by equation 5.28. To find such a η_k, $2n$ cases of equation 5.22 can be set up which would take one of the components of the current estimate to one of its constraints. For simplicity, the k subscript has been removed. A set of n equations can be defined to take the components of the estimate to their lower bounds:

$$l_i = x_i + \eta p_i \quad \text{for } i = 1{:}n \tag{5.29}$$

and another set of n equations can be defined which would take the components of the estimate to their upper bounds:

$$u_i = x_i + \eta p_i \quad \text{for } i = 1{:}n \tag{5.30}$$

Each equation will yield a unique value of η. There exist $2n$ values of η:

$$\eta_{desired} \in \{\eta_j\} \text{ for } j = 1{:}\ 2n \tag{5.31}$$

Of the $2n$ possible values of η that could be found from the above equations, only n positive values exist . This is because the search direction will point towards either the upper or lower bound for each component of the estimate. Therefore none of the n negative values of η can be chosen as the initial test point given to the bracketing routine because the optimal η used in equation 5.22 must be positive:

$$\eta_{desired} \in \{\eta_j > 0\} \text{ for } j = 1{:}\ 2n \tag{5.32}$$

The value of $\eta_{desired}$ must finally equal the minimum of the above set divided by the quantity that the bracketing procedure will magnify it by to calculate the first guess of the third point of the bracketing interval, C: If $A = 0$, then the first guess of the quantity, C, is defined by equation 5.26 as:

$$C = B + (2 - G_r)B = (3 - G_r)B \tag{5.33}$$

Since the initial guess for B could be magnified by $(3 - G_r)$:

$$\eta_{desired} = \frac{\text{minimum}\{\eta_j > 0\}}{3 - G_r} \quad for\ j = 1{:}\ 2n \tag{5.34}$$

This value of η guarantees that the initial triplet of abscissas used in the bracketing routine will not violate the constraints imposed on the estimate of the minimum. For the A.L.S. trajectory, the constraints on the trajectory parameters were chosen as:

$$75^\circ < \theta_f < 90^\circ \tag{5.35}$$

$$7^\circ < \alpha_1 < 17^\circ \tag{5.36}$$

$$1^\circ < \alpha_2 < 17^\circ \tag{5.37}$$

After the bracketing routine has found a triplet values of η which satisfy the bracketing constraints, the set is input into a one-dimensional minimization routine. This routine is a variation of Brent's method. Brent's method uses a combination of the golden section search and the parabolic curve fitting procedure described previously for the bracketing routine. Brent's method, however, continues to narrow the bracketing interval until the minimum is found within a specified tolerance. The variation on Brent's method used utilizes the derivative of the objective function with respect to η_k.

An example of this is shown in Figure 5.8. The derivative of the function is evaluated at the middle point of the bracketing triplet, B. If the derivative is positive, the minimum will likely lie between A and B. In the case shown in the figure, the derivative is negative and the minimum of the function lies between B and C. The derivative at C is then evaluated. The two derivative values $DF(B)$ and $DF(C)$ are linearly extrapolated to zero. The abscissa where the zero derivative occurs is used as the next trial point.

The method for calculating the derivative of the objective function with respect to η_k, $DF(\eta_k)$ is defined as follows: A new state estimate is calculated:

$$\mathbf{x}_{k+1} = \mathbf{x}_k + \eta_k \mathbf{p}_k \tag{5.38}$$

The gradient at this estimate is calculated:

$$\mathbf{g}_{k+1} = \nabla F(\mathbf{x}_{k+1}) \tag{5.39}$$

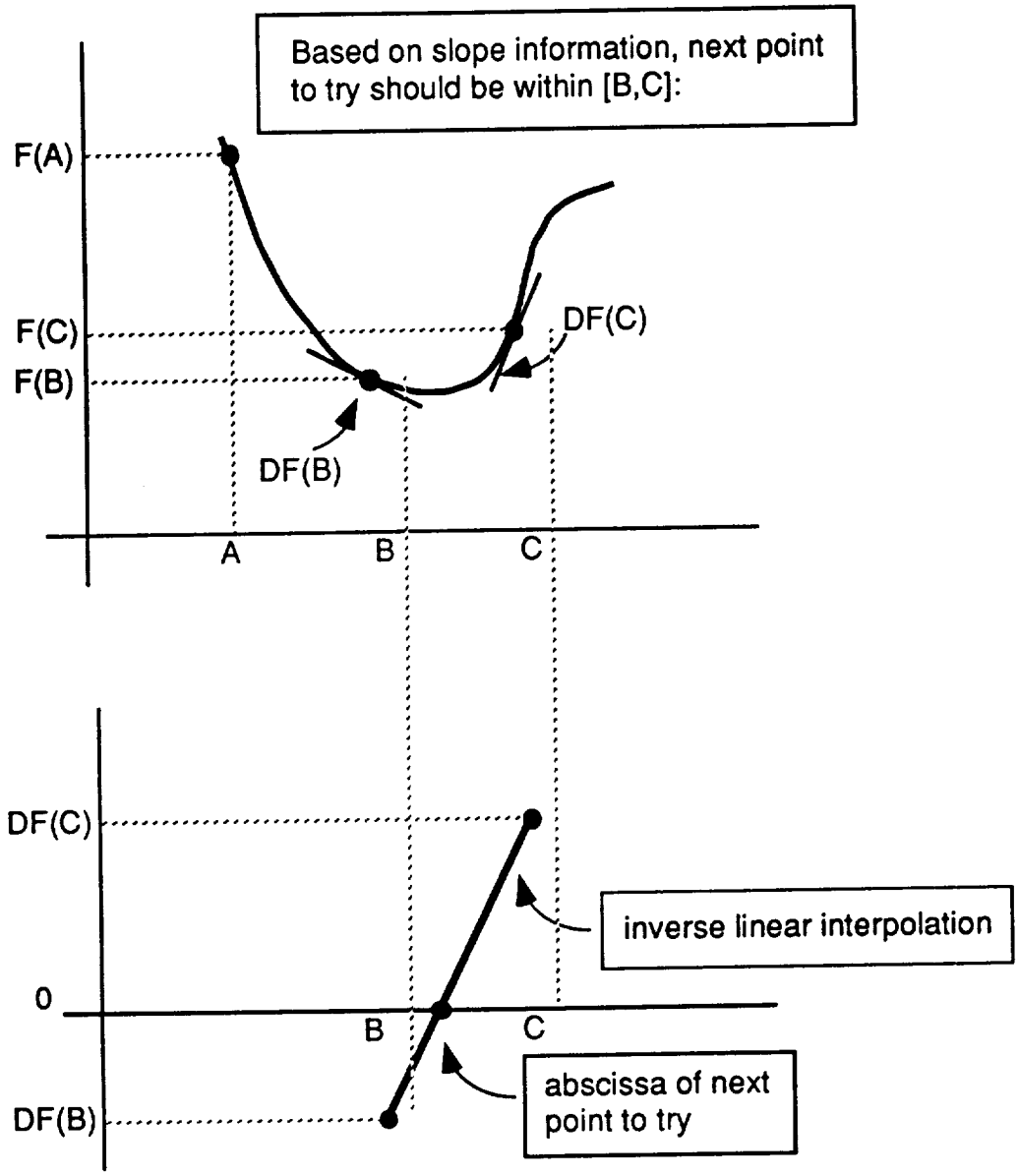

Figure 5.8 Estimating Location of Function Minimum by Extrapolation (or Interpolation) of Slopes to Zero

The derivative of the objective function with respect to η_k is approximated as:

$$DF(\eta_K) = \left(\frac{\partial F}{\partial x}\right)^T \left(\frac{\partial x}{\partial \eta}\right) \approx \mathbf{g}_{k+1}^T \mathbf{p}_k \tag{5.40}$$

5.5 Gradient Approximation

The gradient vector of the objective function can be approximated using the "finite difference technique". For a sufficiently small scalar δ_j, the Taylor Series can be used to approximate to first-order a function of n variables as:

$$F(\mathbf{x} + \delta_j \mathbf{e}_j) \approx F(\mathbf{x}) + \delta_j g_j(\mathbf{x}) \tag{5.40}$$

where:

$\mathbf{e}_j$ = unit vector in the j-th coordinate direction

g_j = j-th component of the gradient vector

The j-th component of the gradient can then be approximated as:

$$g_j(\mathbf{x}) \approx \frac{F(\mathbf{x} + \delta_j \mathbf{e}_j) - F(\mathbf{x})}{\delta_j} \tag{5.41}$$

This form is called the "forward difference approximation" and is exact only for a linear function. Another form can be derived by defining:

$$F(\mathbf{x} - \delta_j \mathbf{e}_j) \approx F(\mathbf{x}) - \delta_j g_j(\mathbf{x}) \tag{5.42}$$

Subtracting of equation 5.42 from 5.40 yields:

$$g_j(\mathbf{x}) \approx \frac{F(\mathbf{x} + \delta_j \mathbf{e}_j) - F(\mathbf{x} - \delta_j \mathbf{e}_j)}{2\delta_j} \tag{5.43}$$

This form is called the "central difference" approximation" and is exact for a quadratic function. However, this form requires twice as many function evaluations as for the forward difference approximation. To reduce the number of computations involved in the optimization procedure, it was decided to approximate the gradient using the forward-difference approximation.

When computing the forward difference approximation of the gradient vector, the objective function, is first evaluated at the current state estimate **x**. Each component of the gradient vector is found by first perturbing the corresponding **x** component by a small amount, subtracting the function value at **x**, and dividing the difference by the perturbation. Thus, if an objective function is defined by n independent variables, then $n + 1$ function evaluations will have to be performed to approximate the gradient vector.

The choice of the values to use for the perturbation δ must take into consideration the accuracy of the predictive simulation and all of the subprograms it uses. If a value is chosen which is smaller than the precision of the simulation, then the value of on-orbit mass which is returned from the predictive simulation will not vary over the perturbation. Many sources, including Scales and Press, recommend using the square root of the machine precision as the perturbation value. This will only work if the procedure used to calculate the objective function has as high an accuracy as the machine. The perturbation used this study was chosen as:

$$\delta = 0.001^{\circ} \tag{5.44}$$

5.6 Conclusions

This chapter compared various numerical optimization methods that could be used to automate A.L.S. trajectory design. The objective of trajectory design is the maximization of on-orbit mass. Because the optimization methods studied are designed to minimize a given objective function, the objective function is defined as the negative of the on-orbit mass . The conjugate gradient method was chosen over direct search methods because it utilizes first derivative information and thus has faster convergence properties. The conjugate gradient method was found to be more practical than Newton's methods for the on-orbit mass optimization problem because it did not require knowledge of the Hessian matrix. This matrix would be take too many function evaluations to approximate with finite differencing.

The chapter then outlined the conjugate gradient method and described the algorithm flow. The conjugate gradient method takes an initial guess for the state vector that will minimize the objective function and iterates on this guess using weighted search directions until the minimum has been located to within some specified tolerance. For a quadratic function of n variables, these search directions are mutually conjugate and will locate the minimum within n iterations.

The one-dimensional minimization along each search direction was also discussed. Two routines that are given in Press were used. The first brackets the minimum with a triplet of points such that the function value at the central point is less than the function value at both of the other points. The second routine takes this bracketing set and continues to narrow the bracketing interval until the minimum is found to within some tolerance.

A procedure was developed for making an initial guess for one of the bracketing points, i.e. the weight that is applied to the current search vector in the calculation of the new estimate. Too large a weight for the search vector would result in the updated estimate being located outside the physical constraints of the problem.

Finally, the finite difference technique used to approximate the gradient vector was discussed. The forward difference approximation was chosen over the central difference approximation because it did not require as many function evaluations. For an objective function of n variables, the forward difference approximation requires $n + 1$ function evaluations.

Chapter Six

SIMULATION AND EVALUATION

6.1 Introduction

The optimization scheme described in the preceding chapter is used in conjunction with the predictive simulation to find the set of trajectory shape parameters which will maximize on-orbit mass for a given $Q\alpha$ limit. The predictive simulation is initialized with the current vehicle state and is provided with a pre-launch wind velocity measurement.

This chapter first describes in Section 6.2 a decision process used to define a $Q\alpha$ limit for pre-launch trajectory optimization. The chosen $Q\alpha$ limit will allow the vehicle to achieve a desired on-orbit mass in the presence of large in-flight wind dispersions from the measured pre-launch wind profile.

Section 6.3 shows the ability of the optimization procedure to define optimal trajectories prior to launch for the trajectory shape described in Chapter 3. However, the use of this trajectory shape made the optimization process sensitive to the initial guess of the optimal trajectory shape parameters.

This problem lead to the definition of a new trajectory shape which is described in Section 6.4. Pre-launch trajectory optimization results are presented for the new trajectory shape. The use of this trajectory shape results in an optimization process which is much less sensitive to the initial guess of the optimal solution.

Section 6.5 discusses the problems encountered in attempting to do trajectory optimization over the flight shape parameters in flight. It was found that, using either trajectory shape, the only option for redesigning the trajectory in flight was to use a different value of the $Q\alpha$ limit than was used in pre-launch trajectory optimization.

6.2 Decision Process for Choice of $Q\alpha$ Limit

The objective of this decision process is to establish a $Q\alpha$ limit to be used for trajectory design- both pre-launch and in flight. This $Q\alpha$ limit must be chosen so that the vehicle will meet a baseline on-orbit mass, $m_{f\ baseline}$, in the presence of the largest wind dispersions from the pre-launch wind measurement that could occur in flight. The baseline on-orbit mass will be specified by mission planning and should include the dry mass of the core stage, the payload, the fuel mass needed for any maneuvers in orbit to deliver the payload, and enough fuel mass to accommodate any problems with the vehicle's insertion into the desired orbit. The vehicle will be able to accomplish this objective by carrying a fuel pad to account for the maximum wind dispersions. The amount of fuel pad needed is defined by mission planning. This decision process assumes that a bound exists for the maximum in-flight wind dispersions from the pre-launch wind measurement.

The other assumptions made by this process are shown in Figure 6.1. This figure shows a hypothetical set of curves corresponding to the maximum on-orbit mass, m_f, that could be obtained (using a trajectory optimization procedure) for a specified $Q\alpha$ limit for different wind profiles. The different wind profiles shown are for a strong headwind, HW_{max}, a strong tailwind, TW_{max}, and no winds, NoW. The amount of on-orbit mass that can be obtained will increase as the winds go from strong head winds to strong tailwinds. Headwinds oppose the vehicle's motion and degrade performance while tailwinds tend to improve performance.

The loci of m_f points are shown as curves that flatten out with increasing $Q\alpha$ limit because there is an upper bound on the on-orbit mass that can be achieved with increasing $Q\alpha$ limit. For a large $Q\alpha$ limit, the on-orbit mass will approach a constant value because the normal force constraint will, in effect, be removed.

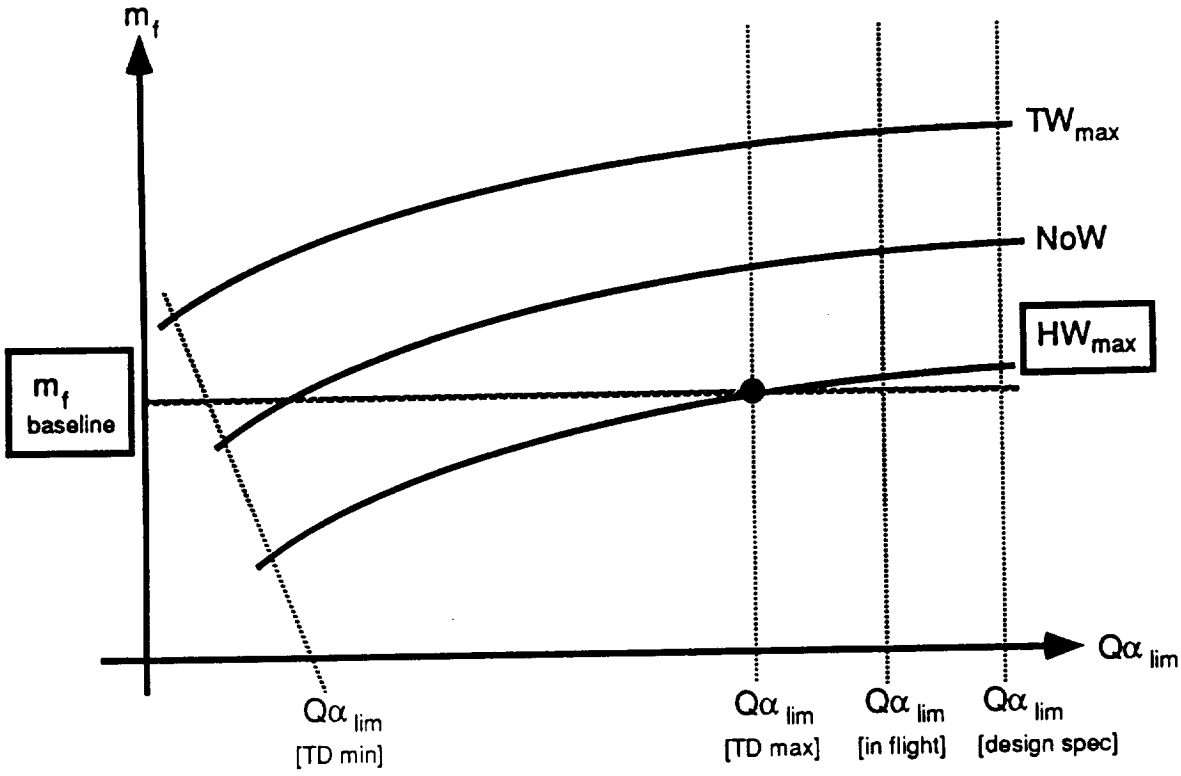

Figure 6.1: Assumptions Made by Decision Process

The abscissas of the $Q\alpha$ limit axis shown in Figure 6.1 are:

$Q\alpha_{lim\ [design\ spec]}$ = $Q\alpha$ limit specified by vehicle design

The $Q\alpha$ experienced by the vehicle in flight cannot exceed this value or normal loads on the vehicle could cause structural damage.

$Q\alpha_{lim\ [in\ flight]}$ = $Q\alpha$ limit to be used in flight for $Q\alpha$ limiting mode switch in Phase 3

This limit must be less than the limit set by vehicle design by a certain factor of safety.

$Q\alpha_{lim\ [TD\ max]}$ = maximum $Q\alpha$ limit to be used for trajectory design

This limit must be less than the limit used for the in-flight $Q\alpha$ limiting mode switch to accommodate excursions in angle of attack caused by the estimator performance, noise, wind spikes, etc.

$Q\alpha_{lim\ [TD\ min]}$ = minimum $Q\alpha$ limit to be used for trajectory design

This limit sets a lower bond on the $Q\alpha$ limit that can be used for trajectory design. A smaller $Q\alpha$ limit than this value will not allow the vehicle to reach orbit. This value will increase in the direction from tailwinds to headwinds.

Having explained the above concepts, it is now possible to outline the steps for the decision process:

1. For the family of curves of on-orbit mass vs $Q\alpha_{lim}$, one of these achieves an on-orbit mass equal to $m_{f\ baseline}$ for a $Q\alpha_{lim}$ equal to $Q\alpha_{lim\ [TD\ max]}$. The headwind profile assumed for this curve is the maximum headwind that is acceptable to accomplish mission objectives. If the winds measured pre-launch are (100-S)% of this value or higher, where S% = percentage of HW_{max} that bounds wind dispersions in flight, then the mission must be cancelled.

2. The reader is now referred to Figure 6.2. If the pre-launch wind measurement is R% of HW_{max}, then the maximum head winds that could be experienced in flight is (R+S)% of HW_{max}.

3. Locate the intersection of the (R+S)% curve and $m_{f\ baseline}$ horizontal line. The $Q\alpha$ limit where this occurs ($Q\alpha_{limTD}$) is the $Q\alpha$ limit to be used for trajectory design for an assumed wind of R% of HW_{max}.

4. The value of the on-orbit mass that can be achieved by the R% wind profile at $Q\alpha_{limTD}$ is $m_{f\ TDinit}$.

5. The initial fuel pad to account for the maximum headwind wind disturbance, S% of HW_{max} is then

$$fp_i = m_{f\ TDinit} - m_{f\ baseline} \tag{6.1}$$

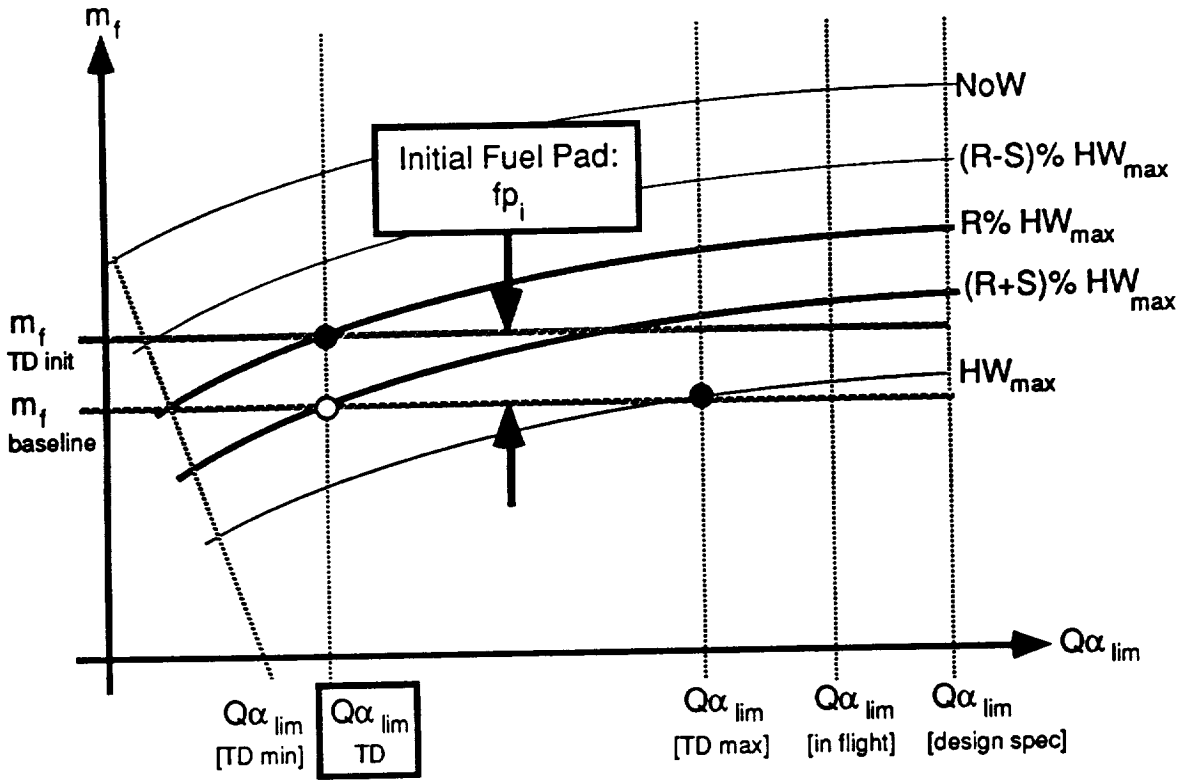

Figure 6.2: Decision Process for a Headwind Pre-Launch Measurement

The fuel pad to be used during endoatmospheric flight should decrease linearly with time to be zero when an altitude is reached where the wind velocity is zero:

$$fp(t) = fp_i\left(1 - \frac{t}{t_{f\,winds}}\right) \tag{6.2}$$

where $t_{f\,winds}$ = the approximate time when the wind velocity has decreased to zero. With this function for the in-flight fuel pad defined, the target mass of any trajectory design updating in flight should be:

$$m_{f\,baseline} + fp(t) \tag{6.3}$$

6.3 Pre-Launch Trajectory Optimization

Four sets of pre-launch trajectory optimization runs were carried out. They utilized the conjugate gradient method in conjunction with the predictive simulation run with a 1.0 second integration time step. The first two sets corresponded to the angle of attack trajectory design profile described in Chapter 3. The second two sets correponded to a new angle of attack profile that was developed in the course of this study. The first two sets of runs will be referred to as the "old alpha profile" runs and the second two sets will be referred to as the "new alpha profile" runs.

The first set of runs for the old alpha profile used 60% of the Vandenburg 69 (Van69) headwind profile and the second set used 100% of Van69. Tables 6.1 and 6.2 show the optimization results of these runs for different values of the $Q\alpha$ limit. The "major iterations" column refers to the number of different conjugate gradient search directions that were required for the on-orbit mass to converge to within a tolerance of 0.5 slugs. The "avg. 1D iterations" column refers to the average number of iterations required for the one-dimensional optimization routine to find the scalar weighting of each search direction. For each run, the maximum on-orbit mass is given along with the values of the optimal set of trajectory shape parameters. Figure 6.3 shows a plot of the maximum on-orbit mass achieved on each run vs. the $Q\alpha$ limit. As expected, the maximum on-orbit mass increases for increasing $Q\alpha$ limit. In addition, the maximum on-orbit mass at each $Q\alpha$ limit is smaller for the 100% Van69 wind profile than for the 60% Van 69. Within the range of $Q\alpha$ limits tested, the plots are both approximately linear.

$Q\alpha$ Limit	Major Iterations	Avg. 1D Iterations	Maximum m_f (slugs)	Optimum θ_f, α_1, α_2 (deg)
2250	3	3	11061.5	88.3, 14.5, 8.3
2500	7	4	11068.3	87.0, 13.6, 8.6
2750	4	2	11075.8	85.4, 14.0, 8.8
3000	8	5	11082.1	84.6, 13.8, 10.2

Table 6.1: Old Alpha Profile Pre-Launch Optimization Results for 60% Van69 Headwinds

$Q\alpha$ Limit	Major Iterations	Avg. 1D Iterations	Maximum m_f (slugs)	Optimum θ_f, α_1, α_2 (deg)
2500	3	5	11052.9	89.1, 15.5, 9.0
2750	5	3	11059.5	88.5, 15.1, 8.9
3000	3	4	11066.8	88.0, 14.9, 9.9

Table 6.2: Old Alpha Profile Pre-Launch Optimization Results for 100% Van69 Headwinds

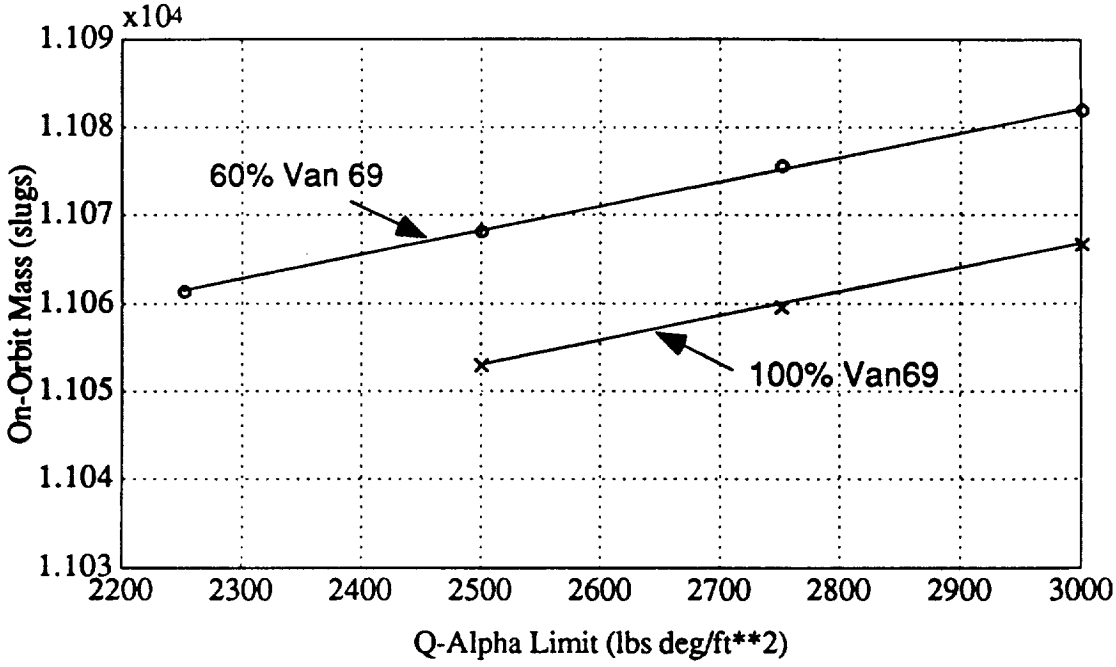

Figure 6.3: On-Orbit Mass Plot for Old Alpha Profile

Figure 6.4 shows the plots of angle of attack versus time for the optimal solutions of trajectory parameters for the case of 60% Van69 headwind. A similar set of plots is shown in Figure 6.5 for the 100% Van69 headwind case. This condition introduced an unforseen difficulty in the implementation of the optimization procedure. If the initial guess for the trajectory parameters was not chosen judicially, the procedure could drive the solution to a region in which the time spent in the α_1 region approached zero. At this point the gradient component corresponding to α_1 becomes identically zero and the assumptions underlying the optimization become invalid. It sometimes required that several different initial guesses for the parameters be considered before a solution was obtained in which the time spent in the α_1 region was greater than zero.

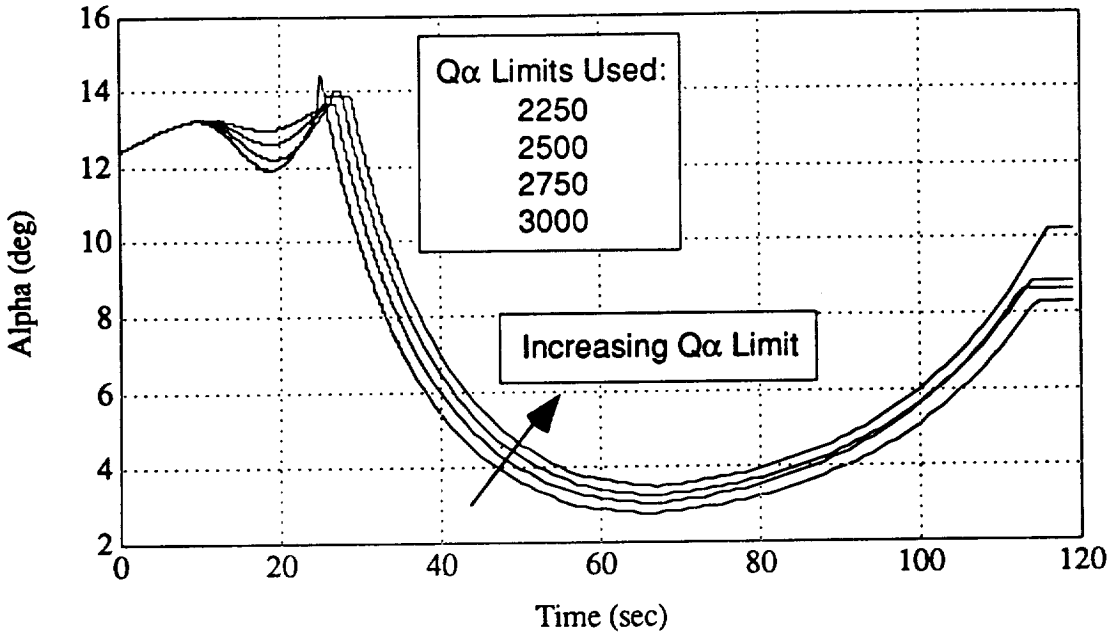

Figure 6.4: Old Alpha Profile: Alpha Plots for Optimal Solutions of 60% Van69 Headwinds

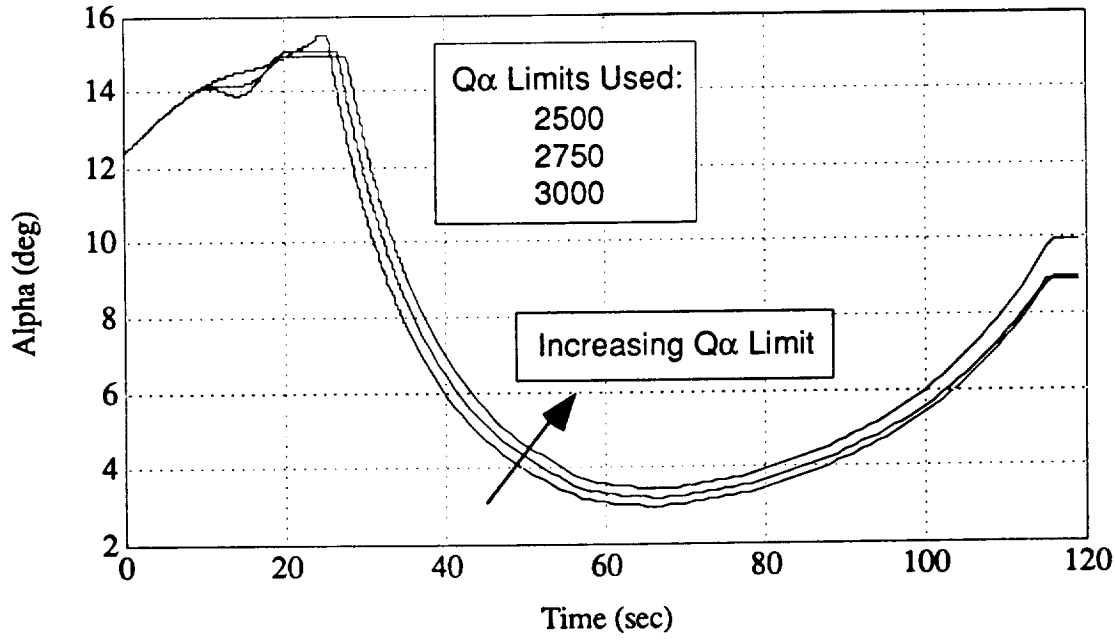

Figure 6.5: Old Alpha Profile: Alpha Plots for Optimal Solutions of 100% Van69 Headwinds

To counteract this problem, a new trajectory shape (alpha profile) was developed. The difference between the new alpha profile and the old alpha profile is in the launch maneuver (Phase 2) part of the trajectory design. Instead of steering the vehicle to a constant angle of attack at the end of the launch maneuver, the objective of the launch maneuver trajectory design was changed to steering the vehicle to the angle of attack limit that was defined by the $Q\alpha$ limit. The error for the one-dimensional launch maneuver optimization was simply based on $Q\alpha$ limit instead of the angle of attack. Table 6.3 shows the error in the $Q\alpha$ at the end of the launch maneuver. The error is a very small percentage of the $Q\alpha$ limit for each run. Instead of spending a very small amount of time in the constant alpha mode, the vehicle went directly to the angle of attack limit. The number of trajectory parameters was reduced from three to two because α_1 was eliminated. This change in trajectory shape made it possible to input almost any realistic combination of θ_f and α_2 into the optimization scheme and have the on-orbit mass converge to within the tolerance. In addition, the reduction in the number of trajectory parameters reduces the number of independent variables used in the optimization scheme.

% Van69 Winds	$Q\alpha$ Limit (lbs deg/ft**2)	Error in $Q\alpha$ (lbs deg/ft**2)
60	2250	4.0
60	2500	6.3
60	2750	0.7
60	3000	1.7
100	2500	6.9
100	2750	4.6
100	3000	5.2

Table 6.3: Error in $Q\alpha$ at End of Phase 2 for Different Simulations of the New Trajectory Design Method

The results for the new alpha profile are presented in the same way as for the old alpha profile for comparison between the two. Tables 6.4 and 6.5 show the optimization results for the new alpha profile for 60% Van69 headwinds and 100% Van69 headwinds. The maximum on-orbit mass obtained for each $Q\alpha$ limit is very close to those values obtained for the old alpha profile. This can be seen in Figure 6.6. The resulting alpha profiles for the optimal solutions are shown in Figures 6.7 and 6.8.

$Q\alpha$ Limit	Major Iterations	Avg. 1D Iterations	Maximum m_f (slugs)	Optimum θ_f, α_2 (deg)
2250	7	5	11060.7	88.2, 7.8
2500	3	6	11067.5	86.8, 9.6
2750	5	6	11075.0	85.3, 11.3
3000	3	4	11082.0	83.7, 9.6

Table 6.4: New Alpha Profile Pre-Launch Optimization Results for 60% Van69 Headwinds

$Q\alpha$ Limit	Major Iterations	Avg. 1D Iterations	Maximum m_f (slugs)	Optimum θ_f, α_2 (deg)
2500	7	5	11052.7	89.1, 10.1
2750	6	3	11060.3	87.5, 10.0
3000	5	4	11066.6	86.0, 9.2

Table 6.5: New Alpha Profile Pre-Launch Optimization Results for 100% Van69 Headwinds

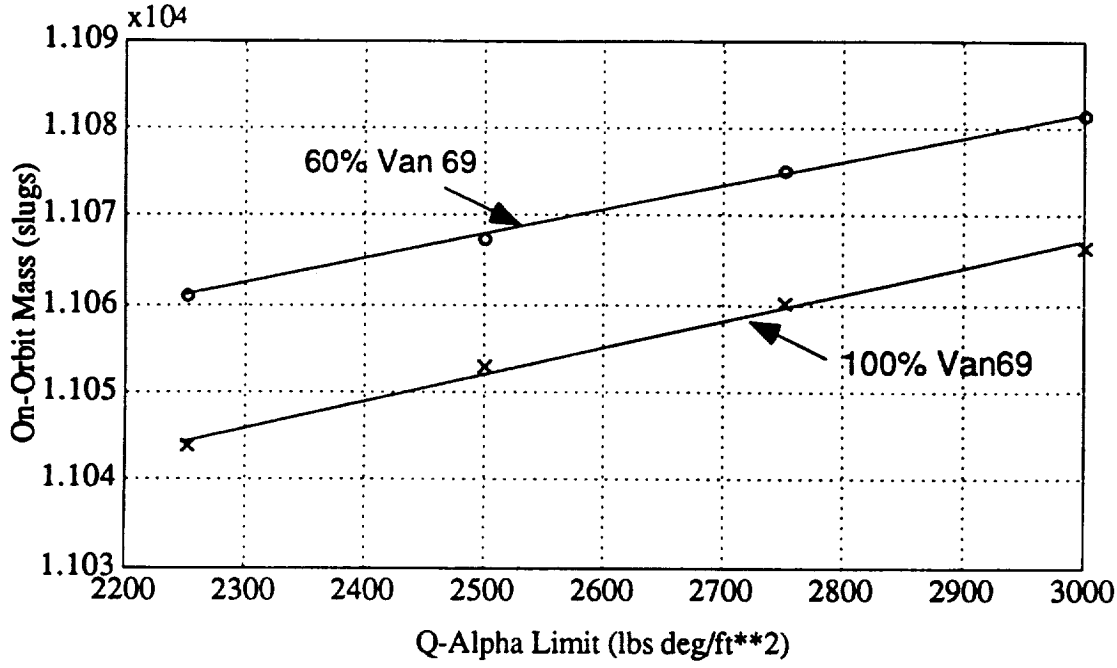

Figure 6.6: On-Orbit Mass Plot for New Alpha Profile

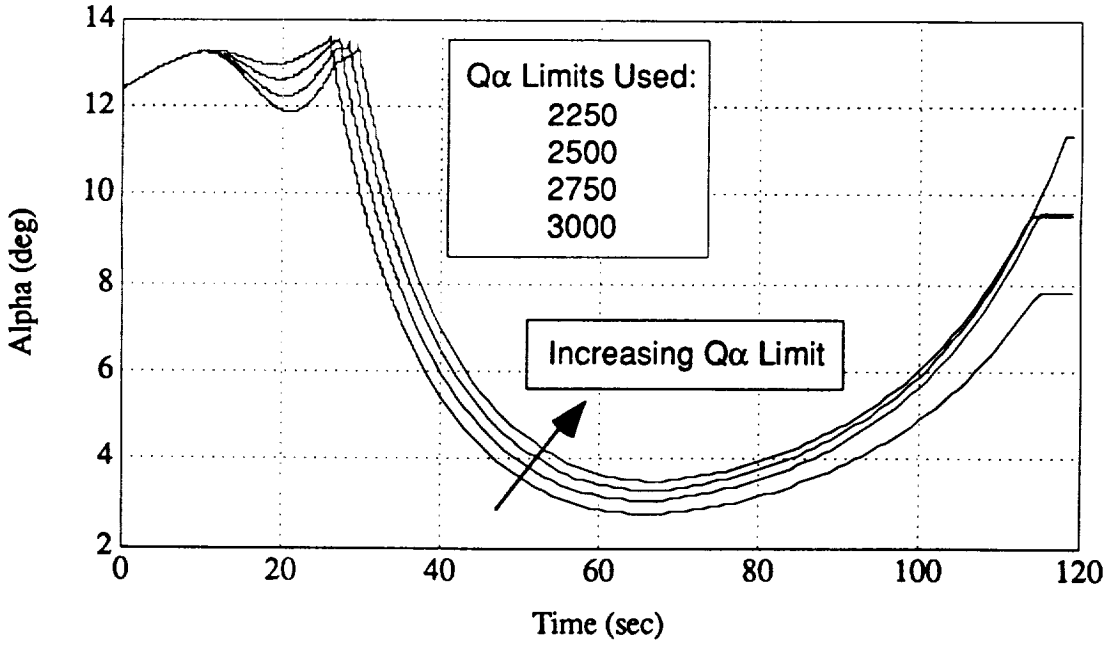

Figure 6.7: New Alpha Profile: Alpha Plots for Optimal Solutions of 60% Van69

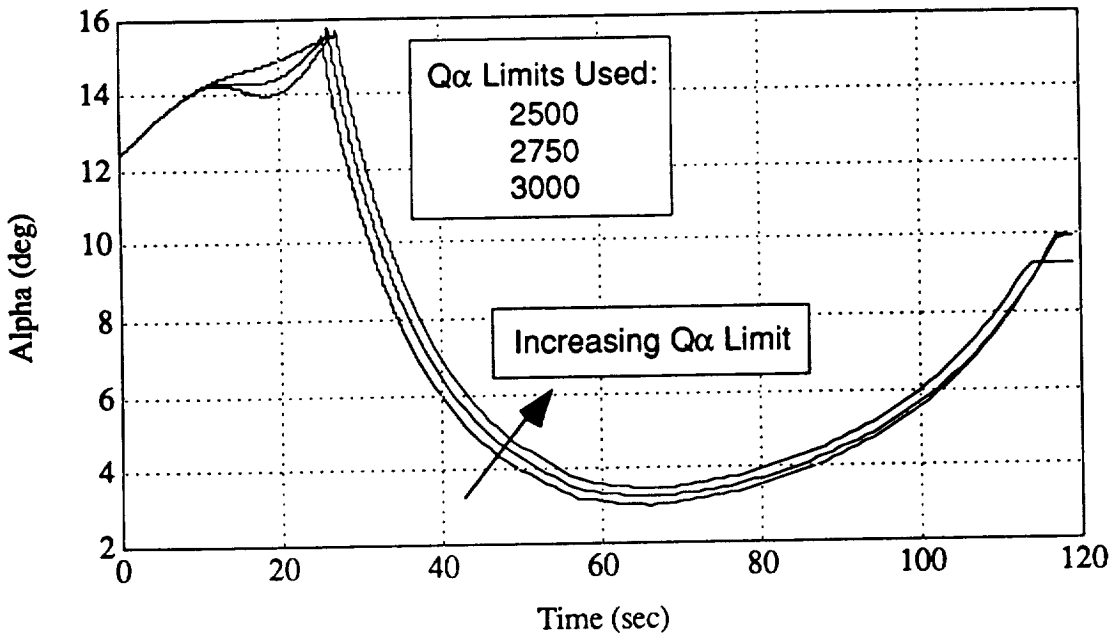

Figure 6.8: New Alpha Profile: Alpha Plots for Optimal Solutions of 100% Van69

6.4 In Flight Trajectory Design

It was decided that any trajectory design in flight should occur after the vehicle has completed the launch maneuver. During the launch maneuver, the altitude is still low enough such that the winds have not built up enough to cause the vehicle to deviate from its trajectory by a significant amount.

Examining the prelaunch optimization results presented in the previous section, the optimal trajectories of both shapes spent most of their time flying the angle of attack limit in the constant $Q\alpha$ phase. Thus, in-flight trajectory optimization over α_1 and α_2 is not practical because the trajectory is almost independent of both parameters. In addition, as the predictive simulation is begun later in flight, even less time is spent within the α_2 portion of flight. This trend was illustrated in Chapter 4.

Therefore, the only redesign that can occur in flight with the trajectory shapes as defined, is based on varying the $Q\alpha$ limit. The prelaunch optimization results proved that

the on-orbit mass would increase with increasing $Q\alpha$ limit. This can be used to ensure that the vehicle meets its time-varying fuel pad requirement, fp(t).

As an example of this, a run was made where the winds experienced in flight were headwinds stronger than those measured before launch. Referring again to Figure 6.3, a baseline on-orbit mass was specified as 11060 slugs. A wind measurement taken before launch was assumed to be the 60% Van69 wind profile. The winds were assumed to be able to vary as much as 40% of Van69. The $Q\alpha$ limit where the 100% Van69 curve crosses the baseline mass was 2750 lbs/ft^2. The on-orbit mass of the 60% Van69 curve at this $Q\alpha$ limit is 11076 slugs. The initial fuel pad is therefore defined as 16 slugs.

The set of optimal trajectory parameters for 60% Van69 at a $Q\alpha$ limit of 2750 lb-deg/ft^2 was then used to design a trajectory for the full simulation. The full simulation was run using all of the estimators. The winds used in flight were 100% Van69. Without any trajectory redesign in flight, the on-orbit mass of the vehicle was 11052 slugs.

Another full simulation was run under the same conditions, but at 60 seconds the trajectory was redesigned. At 60 seconds, the predictive simulation was called with the current vehicle state, the prelaunch wind profile, and a $Q\alpha$ limit of 2750. The predictive simulation returned an on-orbit mass of 11063 slugs. At 60 seconds, the fuel pad will have decreased linearly to 8 slugs. The baseline on-orbit mass plus this fuel pad equals 11068 slugs. Therefore, a search was made to find the $Q\alpha$ limit that would meet this requirement. A $Q\alpha$ limit of 2875 was found to satisfy the requirements and the trajectory was redesigned using this $Q\alpha$ limit. The vehicle flew from 60 seconds on with the new trajectory. The on-orbit mass resulting from this change was 11055 slugs. The performance of the full simulation with and without trajectory design is shown in Figure 6.9.

An engine out case was attempted, but the vehicle was not able to achieve the desired orbit, even with trajectory design in flight at a higher $Q\alpha$ limit.

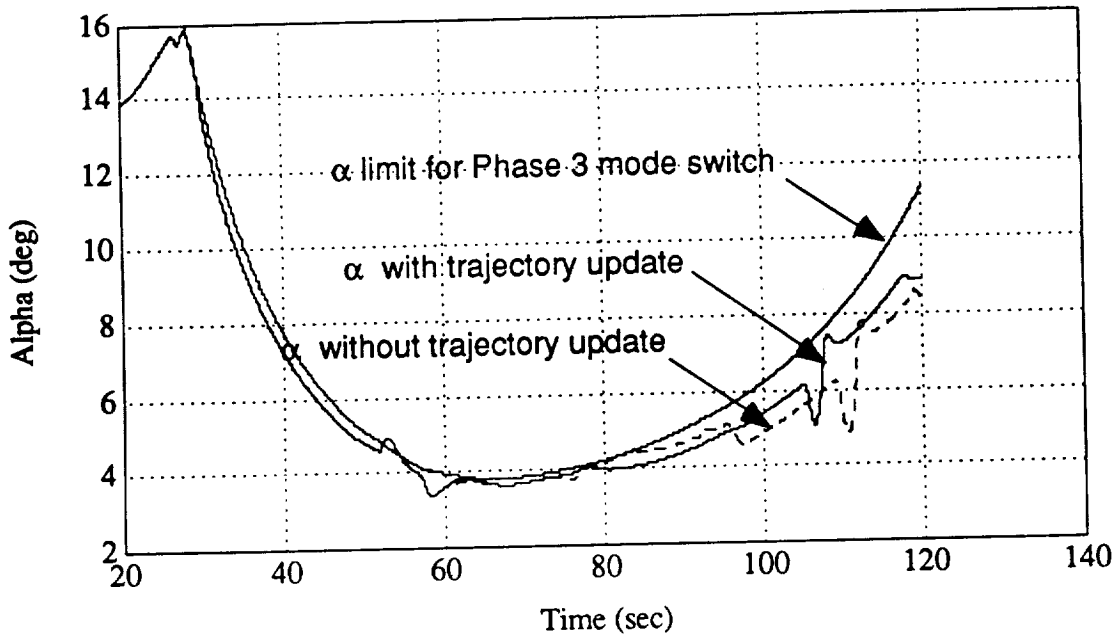

Figure 6.9: In-Flight Trajectory Update for Stronger Winds In Flight

Chapter Seven

CONCLUSIONS AND RECOMMENDATIONS

7.1 Conclusions

One of the objectives of this thesis was to develop a computer program that would automate the prelaunch trajectory design process of the Advanced Launch System (A.L.S.). The other objective was to explore the possibility of redesigning the trajectory in flight to compensate for wind dispersions or an engine out failure.

Since the objective of the A.L.S. trajectory design was the maximization of on-orbit mass, a numerical optimization scheme was employed to determine the set of trajectory parameters, for a given trajectory shape, which maximize on-orbit mass. A predictive simulation was developed which could accurately calculate the on-orbit mass given the vehicle state, wind information, and a set of trajectory parameters. This simulation utilized an idealized control assumption that the control variable, either pitch attitude or angle of attack, was perfectly achieved within a given integration time step. Because of this assumption, the rotational equation of motion did not have to be solved to find pitch attitude and a larger integration time step could be used. Thus, the computational speed of the predictive simulation over the full simulation was shown to be close to that of the full simulation, even with integration time steps as large as one second.

After reviewing the current literature, a conjugate gradient method was chosen over other types of numerical optimization schemes. The conjugate gradient method requires only knowledge of the objective function and its gradient. The objective function was defined as the negative of on-orbit mass. The gradient is the vector of derivatives of the on-orbit mass function, calculated using the predictive simulation, with respect to the trajectory parameters. The gradient is approximated with finite differencing.

The optimization procedure was applied to the problem of prelaunch trajectory design. Using the trajectory shape as originally proposed, it was discovered that optimal solutions produced trajectories in which the time spent in the constant angle of attack portions of Phase 3 was very small. As a consequence, it was found that optimal solutions were very dependent on the initial guess for the trajectory parameters. In some cases, when the initial guess was not close to the optimal solution then convergence to a realistic solution could not be obtained. In these cases, the solution was driven to a condition in which the time spent in the first constant angle of attack portion of Phase 3 was identically zero. In this case, the assumptions underlying the optimization process became invalid and a correct solution was not obtained.

To correct this problem, a new trajectory shape was defined which was similar to the old shape except that instead of having the launch maneuver take the vehicle to a constant angle of attack at the start of Phase 3, the vehicle was taken directly to the angle of attack defined by the $Q\alpha$ limit. With this trajectory shape, neither component of the gradient ever became identically zero before convergence was obtained. The procedure was therefore able to converge to the optimal solution. In addition, the change of trajectory shape reduced the size of the parameter set from three to two and, consequently reduced the dimensions of the optimization problem. Even with the modification in trajectory shape, the predicted on-orbit masses for the optimal solutions were approximately the same as those obtained using the old trajectory shape.

Both sets of prelaunch optimization results from the old and the new trajectory shapes showed the vehicle spending a small amount of time in the second constant angle of attack portion of Phase 3. As a consequence, it was impractical to reoptimize for this parameter during flight. Since the optimum solution tended to approach a simple constant $Q\alpha$ trajectory after the launch phase, the only practical redesign in flight was to use the predictive simulation to design a new trajectory based on a different $Q\alpha$ limit. If it was determined from the predictive simulation that the on-orbit mass would be lower than that needed to meet the fuel pad requirement at the redesign time, then the trajectory would be

redesigned with a higher $Q\alpha$ limit. If it was found from the predictive simulation that the mass would be higher than needed to meet the fuel pad requirements, then the trajectory could be redesigned with a lower $Q\alpha$ limit to reduce stress on the vehicle.

7.2 Recommendations

Further study should be made to determine if more effective trajectory optimization parameters could be substituted for the constant angle of attack parameters of Phase 3. In particular, the constant angle of attack parameter at the end of Phase 3 might be replaced by a parameter that provides a more efficient transition to the Powered Explicit Guidance Phase (PEG). The choice of a new parameter for this transition phase could improve the effectiveness of the in-flight trajectory optimization.

The launch maneuver design for this thesis uses a specified pitch rate profile of sinusoidal form which the vehicle is commanded to follow. Other launch maneuver profiles should be investigated that might provide improvements in payload capabilities.

The impact of an engine-out failure was considered in this thesis, but it was found that it was not feasible to achieve the desired on-orbit mass for the assumed jet model. It was assumed, however, in this thesis that no throttle-up capability existed for the non-failed engines. Alternative designs should be investigated in which the engines nominally thrust at less than full thrust and then increase thrust in the event of an engine-out. For this assumption, the on-orbit mass requirements could more easily be met. It should be determined to what extent the trajectory and on-orbit mass are affected by the particular jet that is failed. A failed jet with a large moment arm from the longitudinal axis through the cg might require a cant angle bias of the remaining jets to reduce the average moment. This could in turn tend to produce a different angle of attack profile than in the nominal case. This occurrence might require modification of the trajectory optimization algorithm. Control problems associated with an engine-out should also be investigated. In particular, the ability to respond to transients produced by the engine-out should be studied. Provision should be made to modify control gains to maintain stability margins for the new thrust model.

Another optimization procedure could also be developed to automatically re-tune the gains used in the vehicle's control systems given last minute changes in payload, vehicle configuration, or mission objective. The objective function could be described in terms of the deviation from desired stability margins. This automation would save much in the way of prelaunch mission preparation.

For this thesis, the steering method employed for Phase 3 was acceleration direction steering. A study should be made to compare the effectiveness of the trajectory optimization procedure with other steering methods e.g., flight path angle steering.

APPENDIX

NASA Langley Research Center provided this study with wind measurements taken at Vandenburg AFB, CA. The wind information was given as velocity plotted versus altitude. The profile used in this thesis is #69, shown in Figure A.1. For simplification, the profile as linearized as shown in Figure A.2.

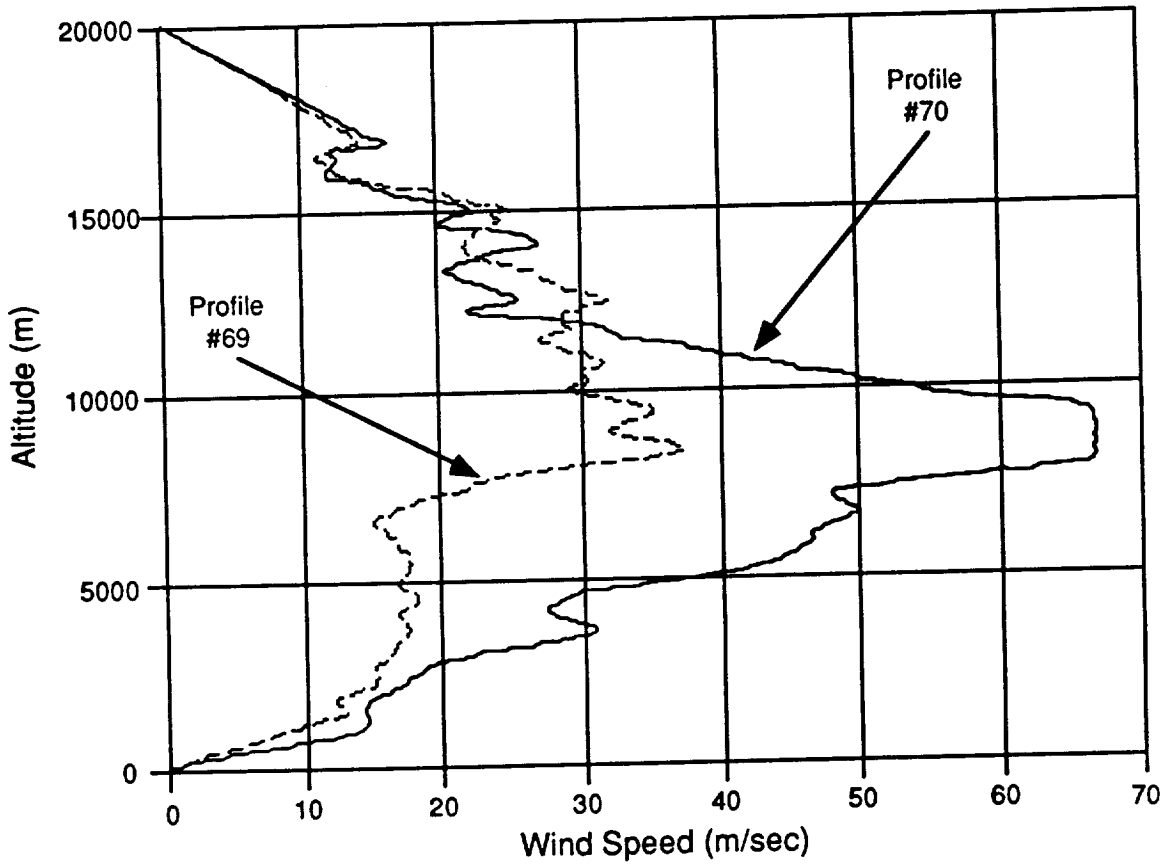

Figure A.1 Vandenberg #69 an #70 wind profiles.

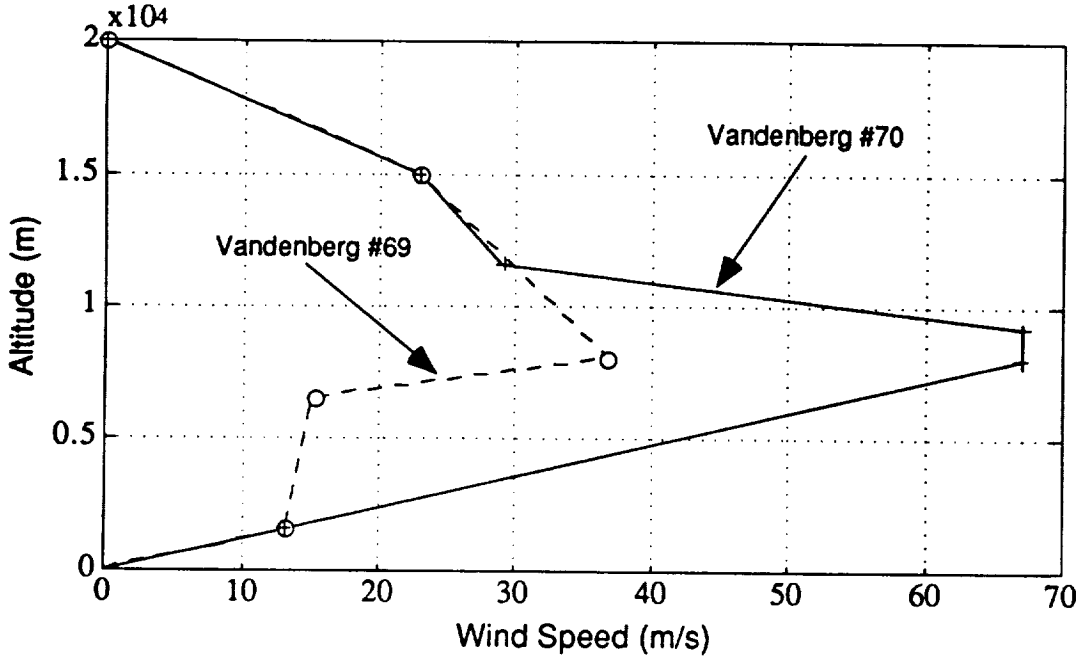

Figure A.2 Linearized Vandenberg #69 and #70 wind profiles.